AD 748344

USCEE Report 423

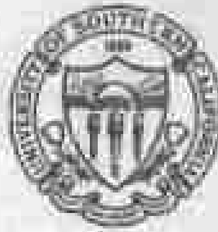

UNIVERSITY OF SOUTHERN CALIFORNIA

NEW METHODS FOR GROWTH AND CHARACTERIZATION OF GaAs AND MIXED III-V SEMICONDUCTOR CRYSTALS

Principal Investigator: William R. Wilcox

D D C
RECEIVED
SEP 13 1972
C

Final Technical Report
1 July 1971 - 30 June 1972

Prepared for
The Advanced Research Projects Agency
ARPA Order Number 1623
Grant No. DAHC 15-71-G6

SEE AD 739374

ELECTRONIC SCIENCES LABORATORY

DISTRIBUTION STATEMENT A
Approved for public release;
Distribution Unlimited

Reproduced by
NATIONAL TECHNICAL
INFORMATION SERVICE
U S Department of Commerce
Springfield VA 22151

BEST
AVAILABLE COPY

Security Classification

DOCUMENT CONTROL DATA - R & D

(Security classification of title, body of abstract and indexing annotation must be entered when the overall report is classified)

1. ORIGINATING ACTIVITY (Corporate author) Electronic Sciences Laboratory University of Southern California Los Angeles, California 90007	2a. REPORT SECURITY CLASSIFICATION UNCLASSIFIED 2b. GROUP

3. REPORT TITLE

NEW METHODS FOR GROWTH AND CHARACTERIZATION OF GaAs AND MIXED III-V SEMICONDUCTOR CRYSTALS

4. DESCRIPTIVE NOTES (Type of report and inclusive dates)

FINAL TECHNICAL REPORT

5. AUTHOR(S) (First name, middle initial, last name)

WILLIAM R. WILCOX

6. REPORT DATE	7a. TOTAL NO. OF PAGES	7b. NO. OF REFS
1 July 1971 - 30 June 1972	129	34

8a. CONTRACT OR GRANT NO. DAHC-15-71-G6	9a. ORIGINATOR'S REPORT NUMBER(S) USCEE Report 423
b. PROJECT NO. ARPA Order No. 1623	
c.	9b. OTHER REPORT NO(S) (Any other numbers that may be assigned this report)
d.	

10. DISTRIBUTION STATEMENT

Approved for public release; distribution unlimited.

11. SUPPLEMENTARY NOTES	12. SPONSORING MILITARY ACTIVITY
	The Defense Advanced Research Projects Agency

13. ABSTRACT

The purpose of this program is to develop new and improved methods for the growth and characterization of gallium arsenide (GaAs) and mixed III-V semiconductor crystals. This is being accomplished by laboratory experiments and related theoretical research. The program is a continuation of one initiated in July 1970 under ARPA Order Number 1628, Grant Number DAHC15-70-G14, and is being completed under Grant Number DAHC15-72-G7, which will terminate 30 June 1973.

DD FORM 1 NOV 65 1473

UNCLASSIFIED

Security Classification

Security Classification

14. KEY WORDS	LINK A		LINK B		LINK C	
	ROLE	WT	ROLE	WT	ROLE	WT

Security Classification

Final Technical Report

1 July 1971 - 30 June 1972

NEW METHODS FOR GROWTH AND CHARACTERIZATION OF GaAs AND MIXED III-V SEMICONDUCTOR CRYSTALS

University of Southern California
Los Angeles, California 90007

Submitted to

ADVANCED RESEARCH PROJECTS AGENCY

ARPA Order Number 1623
Grant Number DAHC15-71-G6
1 July 1971 - 30 June 1972
$184,586.00

Principal Investigator:	William R. Wilcox:	(213) 746-6203
Investigators:	Worth P. Allred:	746-2082
	Clarence R. Crowell:	746-6217
	Agerico Esquivel:	746-6224
	Eric Johnson:	746-6392
	Pat Leung:	746-6392
	James M. Whelan:	746-6219
	David B. Wittry:	746-2510

Details of illustrations in
this document may be better
studied on microfiche

The views and conclusions contained in this document are those of the authors and should not be interpreted as necessarily representing the official policies, either expressed or implied, of the Advanced Research Projects Agency or the U. S. Government.

TABLE OF CONTENTS

		Page
SUMMARY		iii
RESPONSIBLE STAFF		v
I.	BULK CRYSTAL GROWTH	1
	A. Liquid-Seal Czochralski Technique	1
	B. Liquid-Encapsulated Floating Zone Melting	7
	C. Drying of Boron Oxide	21
	D. Travelling Heater Method	21
	1. Gallium Arsenide Growth	21
	2. Organic Analog and Theory	34
	E. Gradient-Freeze Crystal Growth of GaAs	50
	1. Experimental	50
	2. Theory	55
II.	STUDIES OF CRYSTAL GROWTH PHENOMENA	63
	A. Incorporation of Solid Particles	63
	B. Boiling and Convection in Inclusions in a Temperature Gradient	67
	C. Other Crystallization Studies	74
III.	OXYGEN: MEASUREMENT AND CONTROL IN LIQUID EPITAXIAL GROWTH OF III-V SEMICONDUCTORS	74
IV.	CHARACTERIZATION	79
	A. Carbon in GaAs	79
	B. Dislocation Studies and Electrical Properties of GaAs	79
	1. X-Ray Topography	81
	2. Plastic Deformation by Four-Point Bending	85
	3. Cathodoluminescence of Deformed Regions in GaAs	89
	4. Electrical Properties	96
	C. Electron Microprobe Investigations	107
	1. Cathodoluminescence of $GaAs_{1-x}P_x$	107
	2. Stimulated Emission of GaAs	110
	3. Transmission Electron Microscopy	111
	D. GaAs Photoluminescence Measurements	111
	E. High Impedance Hall System	113
	F. Tunnel and Thermal Effects in Photoemission in Schottky Barriers	114
	G. Schottky Barrier Capacitive Characterization of Impurities	122
	1. Theoretical	122
	2. Measurement Facilities	124
	3. Measurements	125

SUMMARY

The purpose of this program is to develop new and improved methods for the growth and characterization of gallium arsenide (GaAs) and mixed III-V semiconductor crystals. This is being accomplished by laboratory experiments and related theoretical research. The program is a continuation of one initiated in July 1970 under ARPA Order Number 1628, Grant Number DAHC15-70-G14, and is being completed under Grant Number DAHC15-72-G7, which will terminate 30 June 1973.

A new Czochralski technique was developed which permits fairly routine growth of dislocation-free GaAs crystals. An apparatus for liquid-encapsulated floating-zone melting of III-V crystals was constructed and is gradually being improved. Three zone passes were successfully completed in one run. The kinetics of drying and moisture absorption by boron oxide encapsulant were measured and published. Further improvements were made in the travelling heater growth method. Theory combined with studies on GaAs and an organic analog system elucidated the conditions required for good single crystal growth by the travelling heater method. A new method was developed to lower oxygen concentrations during liquid epitaxial growth of GaAs, so as to permit growth at significantly lower temperatures and analysis of the oxygen content of semiconductors. It has been found that stirring (e.g., by rotation) and analysis of the oxygen content of semiconductors has a substantial effect on incorporation of solid foreign particles into a growing crystal. Volatile solvent inclusions were observed to boil when the temperature

was sufficiently high in a crystal. This boiling altered the migration rates and directions when a temperature gradient was simultaneously applied.

The influence of bending and short term heating on mobility and carrier concentration of GaAs has been studied. The mobility of our crystals generally decreased as the carrier concentration increased. The cathodoluminescence proved useful for observing dislocation networks near surfaces. The high-impedance Hall apparatus is complete. Further theoretical developments have led to improved understanding of photoemission from Schottky barriers. Photoluminescence measurements confirmed that our Czochralski-grown crystals are less pure than our horizontal Bridgman-grown crystals. Carbon has proven to be a frequent contaminant, with unknown effects on the properties.

Twelve scientific papers have resulted from this program in the last year.

The following equipment was purchased under this grant: ellipsometer, Cat to TTY interface, gas laser and power supply, polisher, high voltage power supply, 2 temperature controllers, power assembly for X-ray generator, volt-ohmmeter and sodium vapor lamp.

RESPONSIBLE STAFF

Staff	Responsibility	Sections in Report
C. R. Crowell	Electronic properties measurement.	IV. D-G
A. L. Esquivel	Dislocation studies.	IV. B
E. S. Johnson	Liquid-encapsulated floating-zone melting and luminescence measurements.	I. B; IV. D
P. Leung	Liquid-seal Czochralski technique and local mode studies.	I. A; II. A
J. M. Whelan	Liquid epitaxial growth and oxygen analysis.	III
W. R. Wilcox	Program coordination, crystal growth research.	I. C-E; II

I. BULK CRYSTAL GROWTH

A. Liquid-Seal Czochralski Technique

As reported previously [1,2] we have invented a new Czochralski technique for GaAs which utilizes a pull rod sealed by molten B_2O_3. (The B_2O_3 is not in contact with the surface of the GaAs melt). We are now able to grow dislocation-free single crystals of GaAs by this technique, as shown in Fig. 1. The crystal is first necked-down to about 1 mm diameter and then expanded to 1 to 2 cm yielding a 4 to 10 cm long crystal. Both Ga <111> seeds and polycrystalline seeds were employed, with no apparent difference in growth characteristics. We have not yet succeeded in growing high-purity uncompensated crystals, however. Table I lists the GaAs ingots grown by this technique during the period 1 July 1971 - 30 June 1972 and the characterization studies performed on samples from these ingots.

Our undoped crystals have a resistivity of about 10^8 ohm - cm. Crystals doped with tellurium have low mobilities compared with crystals grown by the horizontal Bridgman method. This indicates the presence of a deep-level impurity. Mass spectrographic analysis (courtesy of the Air Force Cambridge Research Laboratories) have been performed on one of these crystals. Al, Si and Cl were found, but no Cu. Infrared absorption measurements at USC (courtesy of Prof. W. G. Spitzer) failed to reveal the presence of Si, however.

Recent infrared absorption measurements over a higher frequency region have revealed the presence of carbon in our crystals, as described in Section IV of this report. It is suspected that carbon may be responsible for our low mobilities and high resistivities of undoped crystals. Since the carbon crucibles are a source of carbon in the crystals as well as a possible source of other impurities, we are seeking other crucible materials. Fused silica is undesirable because of probable contamination with silicon. Alumina is good from a purity standpoint, but presents other problems. With radio-frequency induction heating, either a susceptor must

Figure 1 Photograph of undoped GaAs crystal (CZ-37) grown by our new liquid-seal Czochralski technique.

TABLE I. GaAs GROWN BY THE LIQUID-SEAL CZOCHRALSKI TECHNIQUE FROM July 1, 1971 - June 30, 1972

Crystal No.	Dopant	Carrier Conc. (cm^{-3})	Mobility (cm^2/volt-sec)	Samples Sent to	Purpose	Information Feedback
CZ-16 (Jun '71)	Te	2.5×10^{17}	3500	A. L. Esquivel	Dislocation Studies and Electrical Properties.	See Sec. IV-B, this report and Refs. 1 and 15.
CZ-17	Si	6.5×10^{18}		J. Kung	Annealing Studies and Infrared Measurements	- No difference in annealing characteristics between Czochralski and horizontal Bridgman samples. - Carbon local modes observed* See Sec. IV
CZ-19	Undoped	1×10^{17}	3000	A.L.Esquivel	Dislocation Studies and Electrical Properties	
CZ-20	Mg,Se	1.2×10^{18} N		P. Leung	Local Mode Absorption Studies	*
CZ-22	Mg,S			P. Leung	Local Mode Absorption Studies	Unpublished Data
CZ-23	Te			A.L.Esquivel	Dislocation Studies and Electrical Properties	
CZ-25	Undoped	High ρ		H. Huang	Substrates for Deposition of AlP Films	
				D. Gonzales	Absorption Studies with Laser Source	
				S. Nieh	Absorption Studies with Laser Source	

*To be published.

TABLE I (continued)

Crystal No.	Dopant	Carrier Conc.	Mobility	Samples Sent to	Purpose	Information Feedback
				P. Leung	Local Mode Studies of Carbon in GaAs	Carbon Band Observed, No additional bands.
CZ-28	Undoped			V. Yip	Seed Material for THM Growth	
CZ-32	Undoped (Quartz crucible)			P. Leung	Mass Spec. Analysis	
CZ-34	Undoped	High ρ		P. Leung		
CZ-35	Undoped	2.3×10^{16} (Front)	2800	A.L. Esquivel	X-ray Topography	
				C.R. Crowell	Temperature Dependent Hall Measurements	
				D. Wittry	Cathodoluminescence Studies	
				L. H. Skolnik (AFCRL)	Calorimetric Measurements	
				P. Leung	Mass Spec. Analysis	
CZ-[illegible]	Te	4×10^{17} (Back)	2160	C.R. Crowell	Hall, C-V Measurements Schottky Barrier Diodes	
				J. C. Corelli (RPI)	Radiation Induced Extrinsic Photoconductivity Measurements	

TABLE I (continued)

Crystal No.	Dopant	Carrier Conc.	Mobility	Samples Sent to	Purpose	Information Feedback
CZ-37	Undoped	High ρ		L. H. Skolnik (AFCRL)	Calorimetric Measurements	
				P. Leung	Local Modes Studies of Carbon in GaAs	Carbon Band Observed
					Mass Spec. Analysis	
CZ-38	Zn	4.6×10^{17} P	120	D. Wittry	Cathodoluminescence Studies	
				J. C. Corelli (RPI)	Radiation Induced Extrinsic Photoconductivity Measurements	
CZ-40	Undoped	High ρ				
CZ-41	Undoped			V. Yip	Seed Material for THM Growth	
CZ-42	Undoped			S. Nieh	Absorption Studies	
CZ-43	CR	High ρ		S. Nieh	Absorption Studies	
CZ-44	Si			P. Leung	Carbon Local Modes Study	
					Check Control for Growth with ^{30}Si	
CZ-45	Si			P. Leung	Carbon Local Modes	
					Check Control for Growth with ^{30}Si	

TABLE I (continued)

Crystal No.	Dopant	Carrier Conc.	Mobility	Samples Sent to	Purpose	Information Feedback
CZ-46	Zn			P. Leung	Carbon Local Modes	Two additional bands observed. May be due to Zn-C pairs.
CZ-47	Te			P. Leung	Carbon Local Modes	
				D. Wittry	Cathodoluminescence Studies	

be placed around the alumina crucible or the power must be coupled directly to the GaAs. We do not believe such direct coupling will produce the thermal conditions required for growth of dislocation-free crystals. Nevertheless, this has been tried. Unfortunately, the alumina crucibles fractured due to thermal stresses. In view of the fact that carbon is present in our material, pyrolytic graphite crucibles will probably not be considered further for improving our crystal purity. At the moment, we are testing the use of silicon as a susceptor with alumina and silica liners. Silicon carbide is also being considered as a crucible material.

B. Liquid-Encapsulated Floating Zone Melting

We have completed construction of the previously described (1) apparatus for floating zone refining of GaAs while surrounded by a molten encapsulant to prevent As evaporation. We shall describe the evolution of the apparatus during this report period and discuss what we have learned of the problems associated with encapsulated float zoning [3]. Results are summarized in Table II.

The apparatus in (1) was originally constructed with the encapsulated GaAs remaining stationary while the rf coil and auxiliary furnaces moved. This arrangement was found to be unworkable because the long flexible rf leads to the work coil radiated excessively, coupling to and disturbing the motion-table control circuitry. In addition, arcing from the work coil to the auxiliary furnaces occurred when rf power sufficient to heat the GaAs to the melting point was generated. Arcing occurred in the use of isolation transforms for the furnace power supplies. In an attempt to remedy these problems, the work coil was made stationary and attached directly to the rf generator, the leads thus being quite short. In addition, the previous coil was replaced with a high-current, low-voltage "pie" coil. The chuck holding the quartz tubing was attached to the motion table and made to move through the stationary work coil and auxiliary heaters. This arrangement of the apparatus solved the radiation and arcing

TABLE II. SUMMARY OF LIQUID ENCAPSULATED FLOATING ZONE MELTING RUNS

Run No.	Successful Aspects	Unsuccessful Aspects
FZ-1	Assembly of apparatus with moving encapsulated GaAs rod, stationary auxiliary furnaces and rf coil. Familiarity with silica, graphite chuck. sample preparation.	Inadequate heating from auxiliary heaters to remove water from B_2O_3. Insufficient B_2O_3 in tube, difficulty lowering GaAs rod in B_2O_3. Failure when silica broke out at bottom
FZ-2	Redesign dry nitrogen input section of silica. Rebuild various mechanical parts. Weigh out correct volume B_2O_3 and modify graphite to ease lowering of GaAs rod. Solution found to arcing problem from rf coil. Successfully carried molten zone ~ 1 1/2".	B_2O_3 leaking into dry nitrogen capillary forced dry N_2 shut down. Heaters still inadequate to dry B_2O_3. Gas rod broken from graphite chuck prevents removal.
FZ-3	Rewound auxiliary furnaces with Hoskins 875 wire and built variac units to apply 210 V power to heaters, adequate drying of B_2O_3 using auxiliary furnaces. 2 passes of floating zone and recovery of crystal. See Fig. 6 Hall measurements made (Fig. 7).	B_2O_3 leaking into capillary, failure of dry nitrogen drying. Continual loss of As bubbles from GaAs-B_2O_3 interface. Drift of rf generator across floor.
FZ-4	Anchor rf generator to floor. Construction and successful use of 12" auxiliary furnace to replace 6" furnace. Modification of apparatus to apply He overpressure. Found procedure to avoid B_2O_3 leaking to capillary. Successful control of As bubbles by applied overpressure.	Broke GaAs from graphite chuck upon lowering into B_2O_3. Incomplete melting on a single pass.

TABLE II (cont'd)

Run No.	Successful Aspects	Unsuccessful Aspects
FZ-5	Develop precision threads for feed rods. Successful techniques for lowering GaAs rod into B_2O_3 as routine procedure. Successful drying of B_2O_3 with no provisions for or use of dry gas. 1 pass through feed stock under He overpressure.	Mistake of As bubbles for H_2O bubbles resulted in reapplication of vacuum and distribution of B_2O_3 over much of silica. B_2O_3 froze and broke up silica--could not recover sample. Feed rod tipped to side during melt through.
FZ-6	Redesign of heaters to prevent B_2O_3 solidification. Redesign of bottom of silica to provide GaAs support after melt through. ! pass through feed stock under He overpressure.	Failure to control zone diameter so that a second pass would be possible. Impossible to recover GaAs because of separation from chuck.
FZ-7	Control of zone size to permit 3 passes. Discovery of variation in power necessary for melting with the number of passes. Hall measurements on pieces shown in Fig. 8.	Feed material broke from chuck because of build up of structurally unsound material at position where float zone passes ended.

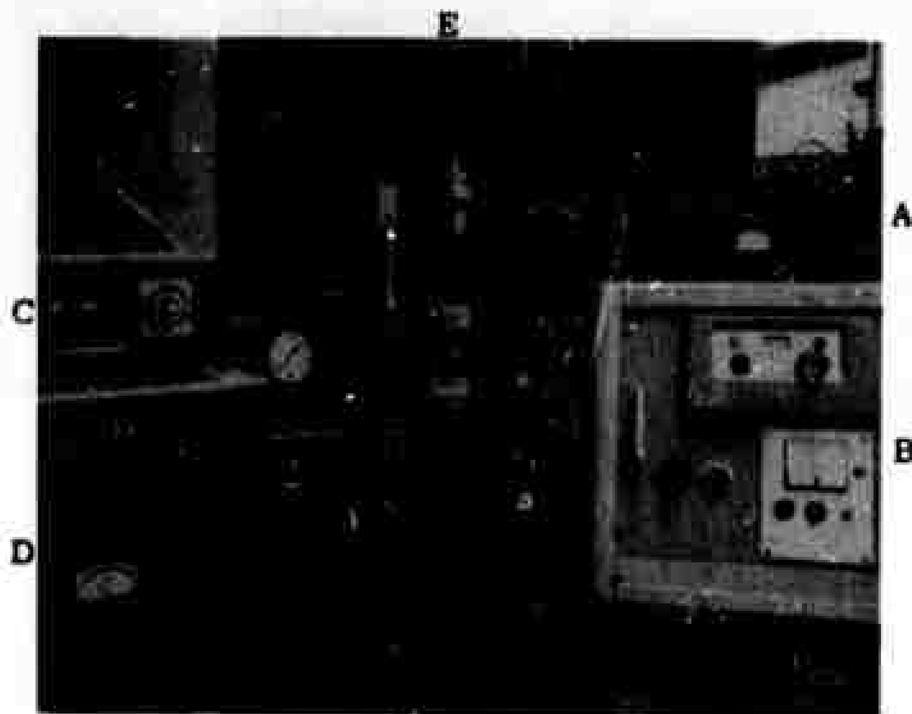

Reproduced from best available copy.

Figure 2. Photographs of the Liquid-Encapsulated Floating-Zone Melting Apparatus for Growth of High Purity GaAs and Mixed III-V Crystals.

A. Control for auxiliary heaters (G).

B. Controls for radio-frequency generator (J).

C. Controls for controlled-motion table (H).

D. Vacuum system.

E. Quartz rod and tube.

F. Induction coil and molten zone.

G. Auxiliary furnaces to keep B_2O_3 molten.

H. Controller motion table.

I. Support stand for auxiliary furnaces (G).

J. Radio-frequency generator.

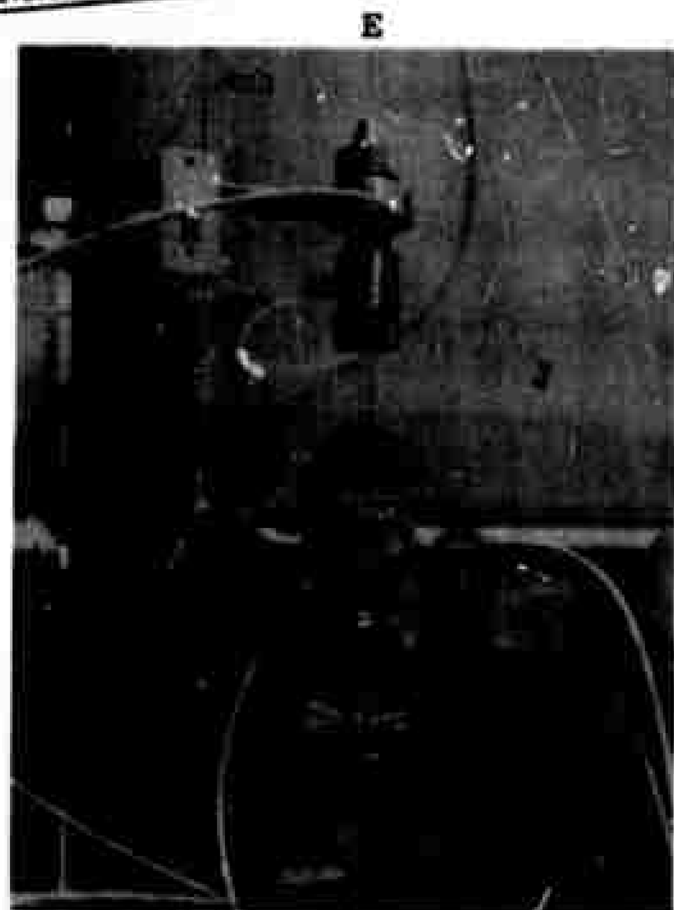

Close-up.

problems. The revised apparatus is shown in operation in Fig. 2.

A second major problem area encountered in the first experiments was to provide adequate drying of the boron oxide encapsulant prior to lowering the GaAs feed rod into position in the encapsulant. Without adequate drying, water vapor formed at the boron oxide-molten GaAs interface, producing uneven support for the molten zone and allowing the escape of As. Although commercial boron oxide sold for encapsulation purposes was nominally "dry" a significant amount of water remained, and additional water was absorbed from the air during loading of boron oxide into the quartz tube. The water could be removed by heating boron oxide under vacuum to 1000 to 1100°C for several hours. An attempt was made to speed the removal of water by bubbling dry nitrogen gas through the molten boron oxide. A difficulty with this technique was that molten boron oxide wet the capillary through which the gas was introduced, and unless the capillary was also raised to ~600°C, the boron oxide would harden and break the fused silica. Thus, it would have been necessary to heat an ever increasing amount of the silica ware. Although we did find a procedure which solved the creep problem we concluded that the best approach was to do away with the use of dry gas completely, thereby simplifying both the silica fabrication and the boron oxide drying procedure. In order to reach the high temperatures necessary to dry boron oxide using only a vacuum, new auxiliary furnaces were constructed and provisions made for use of 210 V electrical power. At present, adequate drying is obtained by heating the boron oxide under vacuum (forepump pressures) for 6 to 8 hours at 1000°C, followed by an additional hour at 1100°C. The silica and related apparatus presently used are shown schematically in Fig. 3.

Having solved the above problems, we turned to the float zoning of GaAs. The first difficulties to be faced here were concerned with how to get the sample into and out of the encapsulant. Initially, GaAs rods were connected to the graphite chuck using hand-ground threads. These threads often broke, and consequently the GaAs could not be removed from

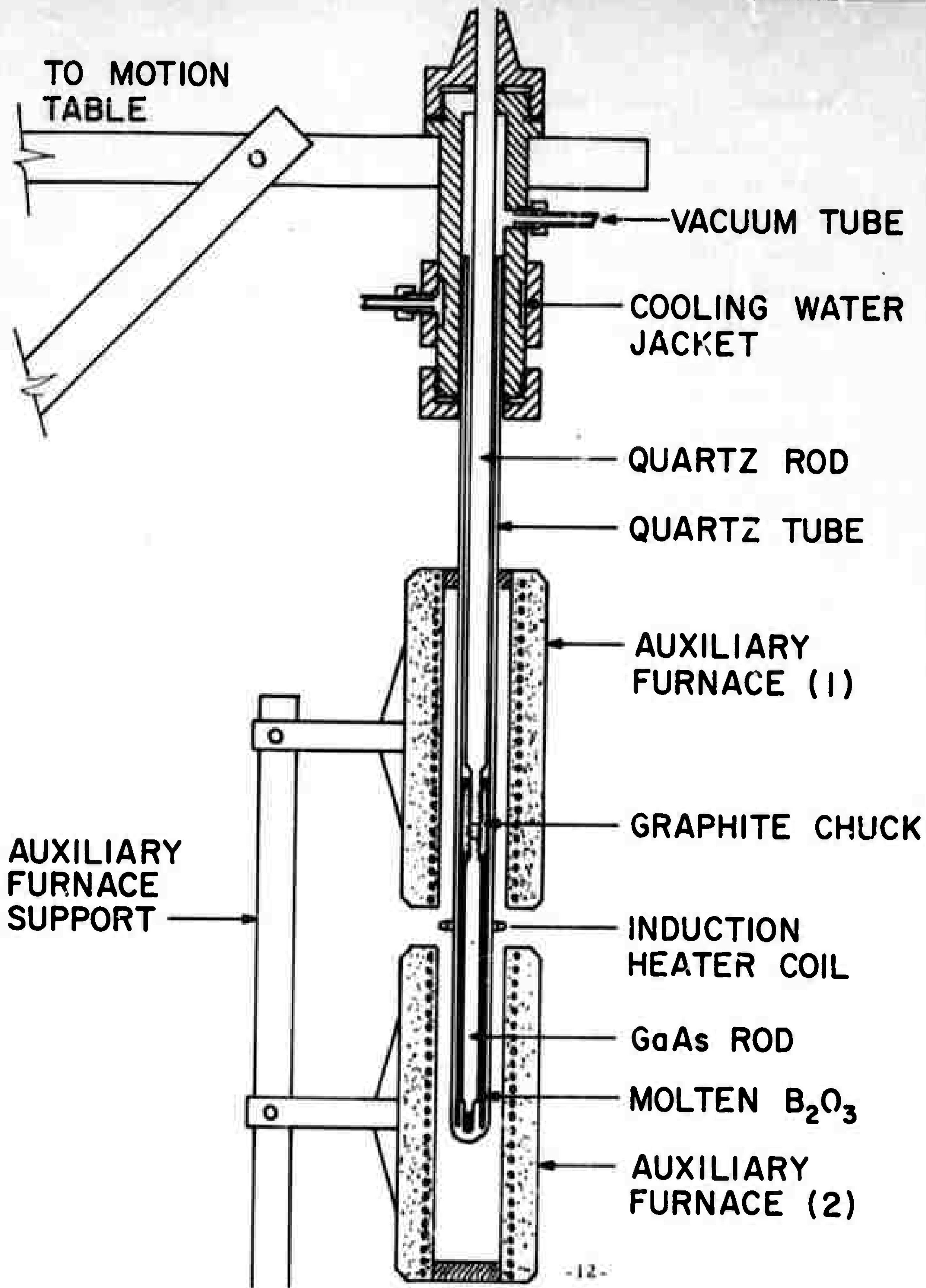

Figure 3 Diagram of apparatus for liquid encapsulated floating

from the encapsulant. A threading jig was constructed to grind precision threads onto the feedstock rod so that the stock could be held firmly in the chuck. A second step in developing our present technique was to realize that the sample could not be pushed quickly through the boron oxide but was best protected by dropping slowly into position by gravity. The immersion process was speeded by heating the boron oxide to 1000°C to reduce its viscosity. At this temperature small bubbles of As vapor appeared on the immersed GaAs. This was in no way a problem if one did not mistake the As bubbles for water vapor, and reapply vacuum in an effort to remove them.

Two techniques were developed to initiate rf coupling to the GaAs. In the first, coupling was made with the graphite chuck and the hot coupled region was moved downward onto the GaAs. Since the rf coupled with greater ease to graphite than to solid GaAs and since GaAs had to be heated by the chuck until sufficiently conductive, this technique used high rf power levels. If not done properly, separating or thinning of the feedstock near the chuck could have resulted. In the second, preferred, technique, the encapsulated GaAs rod was heated to ~ 1000°C in one of the auxiliary furnaces and quickly repositioned in the rf coil. Induction heating could easily be initiated at any position on the feed stock using this technique.

Once rf coupling was initiated at some position on the feed stock, the rf power was increased until melt-through was achieved. Melt-through was determined when the section of the feedstock above the rf coil could be rotated independent of the lower section. It was important that the feed stock was well supported by the bottom silicaware, since support from above was lost at melt-through. If support was lacking, the bottom section tipped to the side and twisting from above to confirm melt-through produced a spiral effect in the float zoned material. At melt-through, As bubbles began to push out of the molten GaAs zone and up through the boron oxide. These bubbles could be prevented by applying an inert gas overpressure (5-8 $lbs\text{-}in^{-2}$) to the boron oxide, and in fact, As bubbles

still in contact with the melt could be driven back into the melt by the overpressure. What could not be prevented was the diffusion of As through the boron oxide and into the inert gas to condense on cool silica. This process was aided by the 700-800°C temperature which had to be maintained throughout the boron oxide. The amount of As lost in this manner was small but resulted in Ga enrichment of the melt, and a slight lowering of the power necessary for maintenance of the molten zone as the pass proceeded.

We found that the loss of material from a zone too long to be contained by surface tension was not a serious problem. Extra material which broke away from the zone dropped slowly through the encapsulant and froze, and was occasionally remelted and rejoined to the zone on the next pass. Our early discovery of the ease with which a large encapsulated zone could be contained suggested that zoning could be done at an rf power level significantly greater than that needed for melt-through, eliminating the risk that a small negative rf power perturbation might cause re-contact of the two solid portions. Although the large zone which resulted could be easily contained we soon found that we could not control the zone nor achieve more than a single pass. These problems come about if the melt becomes large enough to neck in at the top and balloon at the bottom. The resulting situation is common with the zone refining of substance where the rf coupling to the melted material is much greater than that to the solid. If the zone is being moved from the bottom to the top of the feed rod, the necked-in portion does not adequately heat the solid above and the zone is left behind the rf coil. Moving in the opposite direction, one transports material toward the bottom of the feed rod and the diameter of the upper section decreases until separation from the chuck occurs. The only way we have found to maintain diameter control and allow multiple passes is to keep the zone as small as possible. In practice, this means keeping the power level as close to the melt-through value as is possible.

This last requirement is more exacting than first appears. We have found that the melt-through power drops dramatically with succeeding

passes and that a new rf power setting must be found at the beginning of each pass. We do not yet have an explanation for this behavior.

After the desired number of passes have been made, the material must be pulled out of the boron oxide encapsulant, and into the upper auxiliary furnace to permit boron oxide remaining on the crystal to thin and move downward. Some surface break off of GaAs results when the rod is cooled to room temperature, but the bulk appears to be undamaged. One must take care during zoning that the passes do not all end in the same position on the feed rod because the gallium-rich material present in the zone at the end of each pass has little structural strength as a solid and the feed rod will break when pulled from the molten boron oxide.

With our best efforts we have made three floating zone passes, with diameters up to 8 mm, and grown single crystals. Individually, most runs have ended in failure, and only one crystal has been extracted intact. Each experiment has revealed problems which have been solved only to find a new difficulty. We now believe we are close to routine float zoning and successful recovery of single crystal GaAs.

We shall make a few further comments and describe some of our results, as summarized in Table II. We have used feed rods cut to a square cross-section from Bridgman-grown, polycrystalline ingots. Round GaAs castings, formed by the gradient freeze technique (Section I.E) have not been used as feed material because the threads ground onto these feed rods were quite weak due to voids present in the castings. We believe that improvements in casting techniques (Section I.E) will permit the use of castings.

We have produced what appear to be GaAs single crystals from sections of single crystal feed rod, as shown by the cleavage plane in Fig. 4. The feed was a square rod prior to a single float zone pass, and has clearly been melted through, as can be seen by examining the "tree ring" structure from a section of the same sample with incomplete melt-through, shown in Fig. 5. We must point out, however, that most of the

GaAs chunks recovered after zoning were more polycrystalline than the original feed material, and straight twin lines were commonly observed, as appear in Fig. 6, for an ingot recovered intact from the encapsulant. Thus far, a limited amount of work has been done to determine whether encapsulated float zoning can greatly improve the purity of GaAs. This is largely because of a lack of samples. Hall measurements on n-type samples cut from the ingot in Fig. 6, which had two passes, showed a zone leveling of impurities (Fig. 7). This result is not unexpected, when one considers the orientation of the Bridgman-grown feed rod and the direction of the passes. The carrier concentration decreased by a factor of three for samples cut from the ingot near the beginning of the passes relative to samples cut from a similar position in the feed rod. Hall samples cut from pieces (Fig. 8) recovered from an ingot with three passes have also been measured. The original hole concentration of $2.10^{17}/cm^3$ was lowered by one-half by float zoning. This result implies an effective segregation coefficient of 0.80, a value in agreement with that for carbon in GaAs.* Measurement of the optical absorption of these samples may indicate whether this agreement is more than coincidental. Other pieces of the ingot with three floating zone passes have been sent to the Battelle Columbus Laboratories for mass spectrometer analysis.

When we have learned the techniques required to carry out approximately six passes and recover the ingot from the encapsulant using scrap GaAs feed rods, we shall try feed rods of high-purity, single crystal GaAs grown by Bridgman or gradient freeze techniques. This last experiment should indicate whether bulk GaAs purity levels approaching that of epitaxial films are possible and, if not, what the intrinsic limitations are. We shall also try to increase the diameter of the rods to 1 cm and beyond. One technique to accomplish this will be to try to increase the

---

*L. R. Weisberg, F. D. Rosi and P. G. Herkbart, in Properties of Elemental and Compound Semiconductors (Interscience, New York, 1960), p. 25.

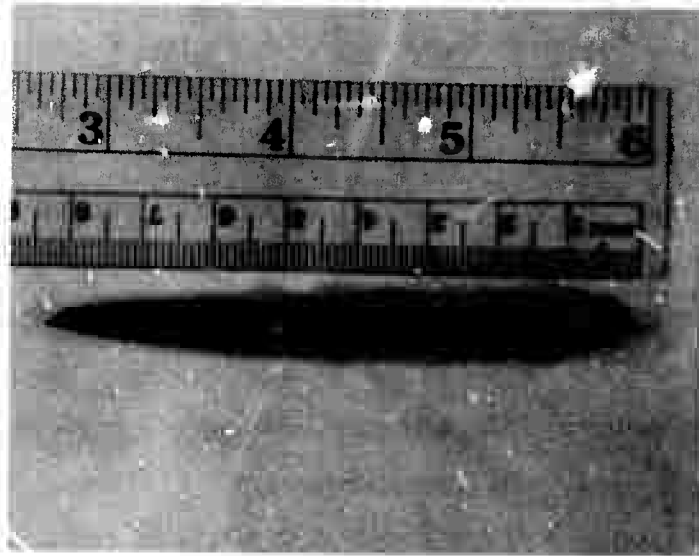

A.

Reproduced from
best available copy.

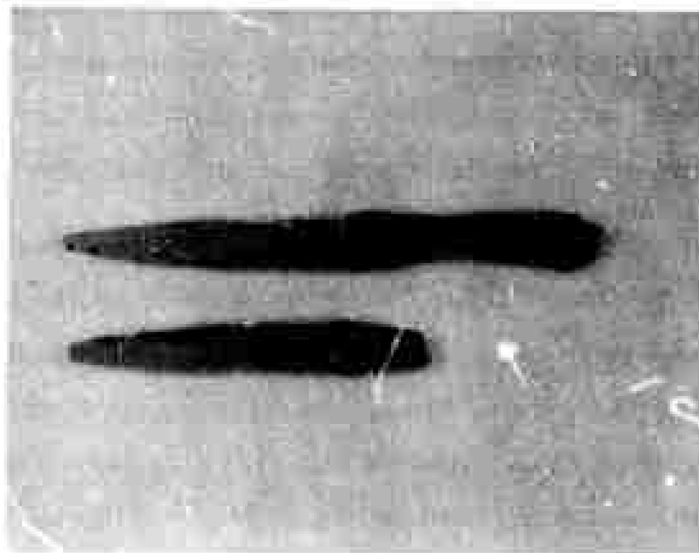

B.

Figure 6. Zoned ingot (FZ-3); A. As-grown; B. Sectioned crystal, showing twins.

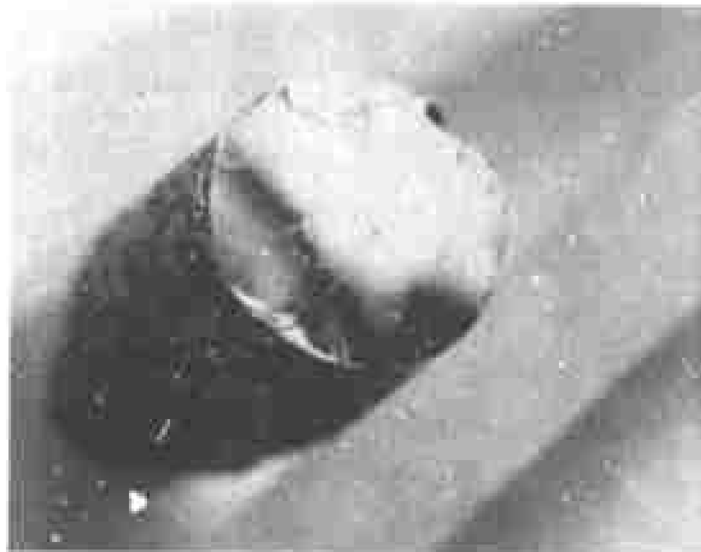

Figure 4 Cleavage from GaAs subjected to one zone pass.

Reproduced from
best available copy.

Figure 5 Cleavage from GaAs incompletely melted through.

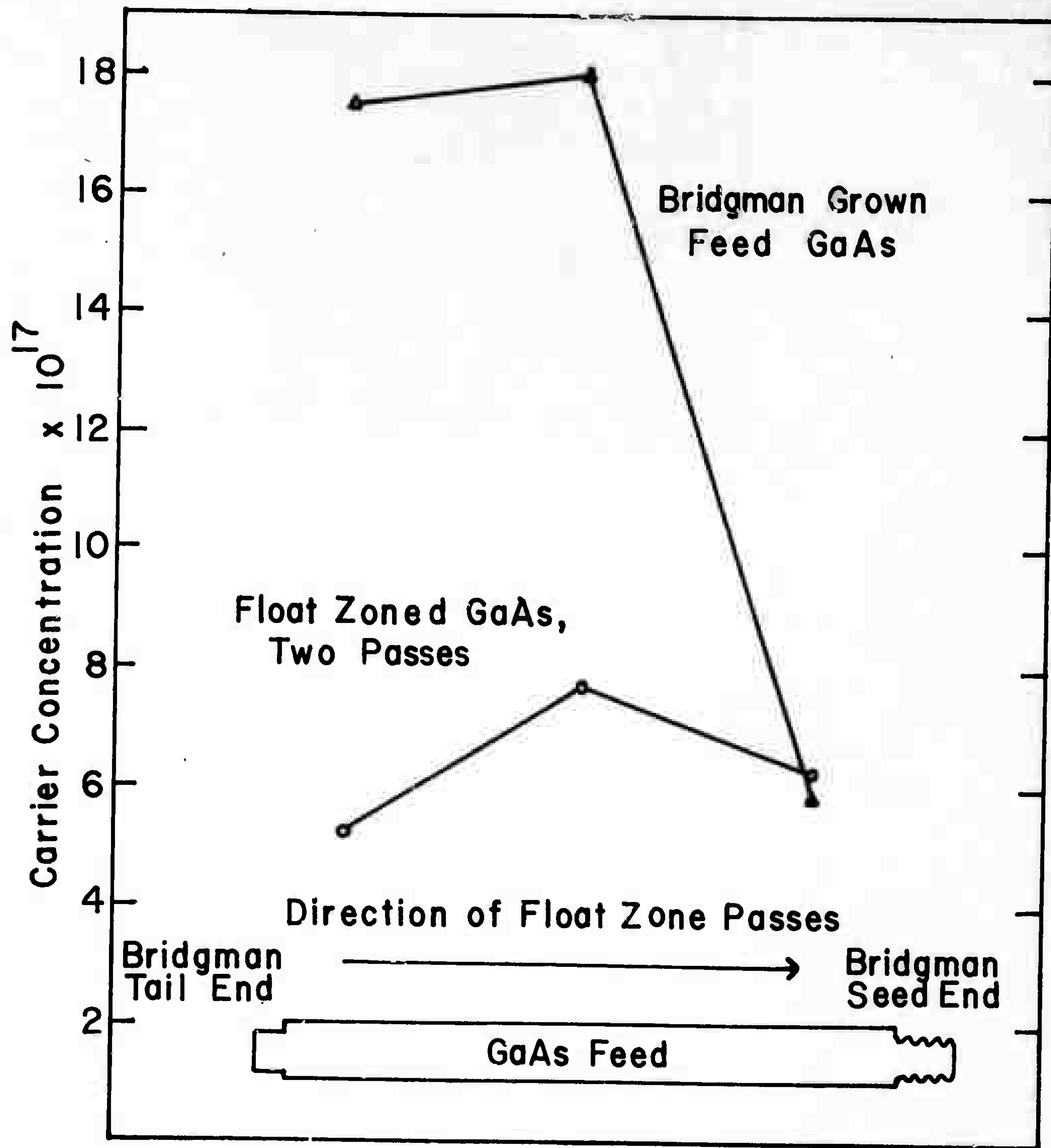

Figure 7 Variation of carrier concentration along GaAs before and after zoning.

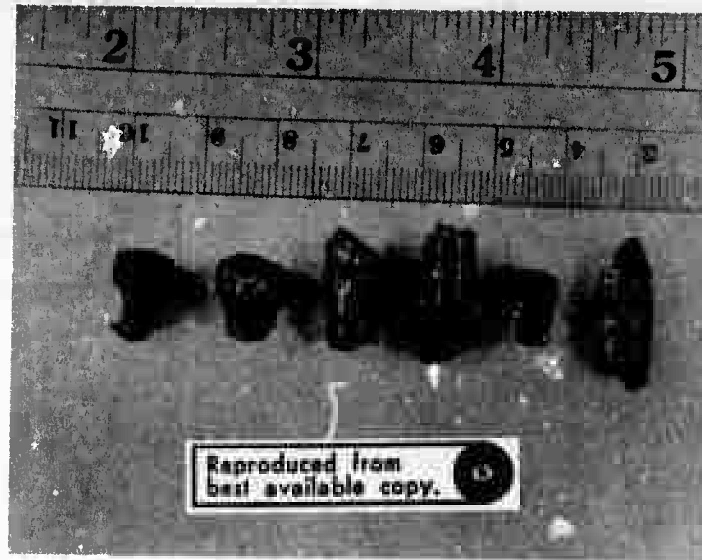

Figure 8 Pieces (FZ-7) recovered from zoned GaAs.

density of the encapsulant by mixing lead fluoride with boron oxide, thus reducing the gravity distortion of the zone and paving the way to really large ingots. Finally, we would like to try to move a gallium zone through encapsulated GaAs, at temperatures well below the GaAs melting point, in a manner similar to the traveling heater technique described in Sec. (I.D) as a prelude to experiments on the encapsulated growth of mixed III-V crystals.

C. Drying of Boron Oxide

The experiments on drying of B_2O_3 encapsulant have been completed and a paper published [4]. Figure 9 shows the exponential decrease in water content during bubbling of dry nitrogen through molten B_2O_3 at 1200°C, as monitored by infrared absorption measurements. The upper curve is for thin samples while the bottom curve is for thick samples, indicating that some moisture was reabsorbed from the air during sampling. Figure 10 shows moisture absorption when vitreous B_2O_3 was exposed to air at room temperature. The first region is parabolic, corresponding to diffusion limited absorption. The surface was smooth during this period. The second region is linear--a constant absorption rate. The B_2O_3 surface was powdery during this period and gave an X-ray powder pattern for boric acid. Figure 11 shows removal of surface moisture from B_2O_3 by exposure to a vacuum at room temperature. The curve is a sum of two exponentials, indicating two parallel removal mechanisms--probably involving boric acid conversion to B_2O_3 and water diffusion and desorption from B_2O_3.

D. Travelling Heater Method

1. Gallium Arsenide Growth

As reported previously [1], we have grown bulk GaAs single crystals by the travelling heater method, in which a solvent zone of Ga was moved through polycrystalline feed by means of a travelling heater.

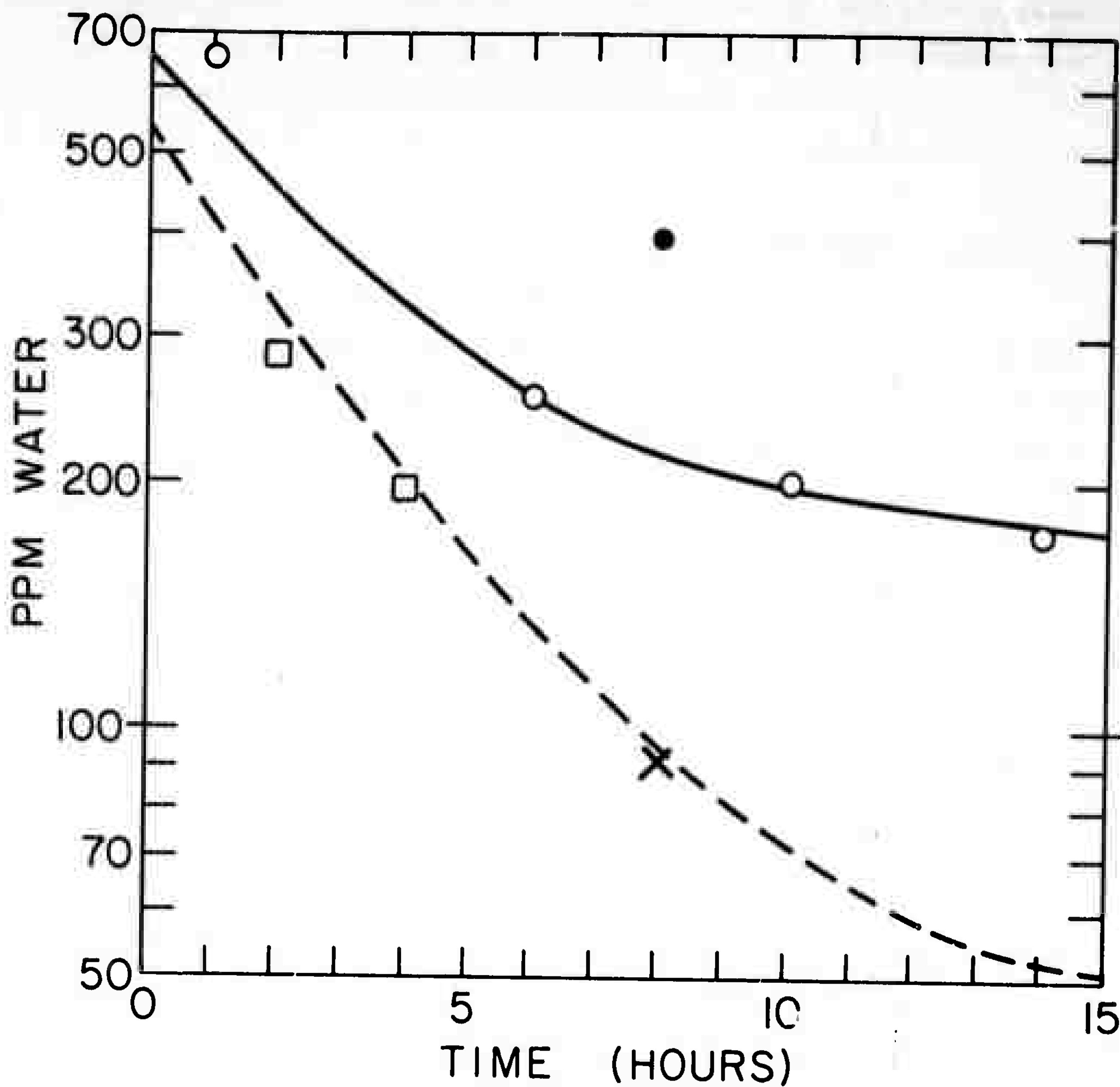

Figure 9 Rate of Removal of Water from Molten B_2O_3 by Bubbling Dry Nitrogen at 1200°C.

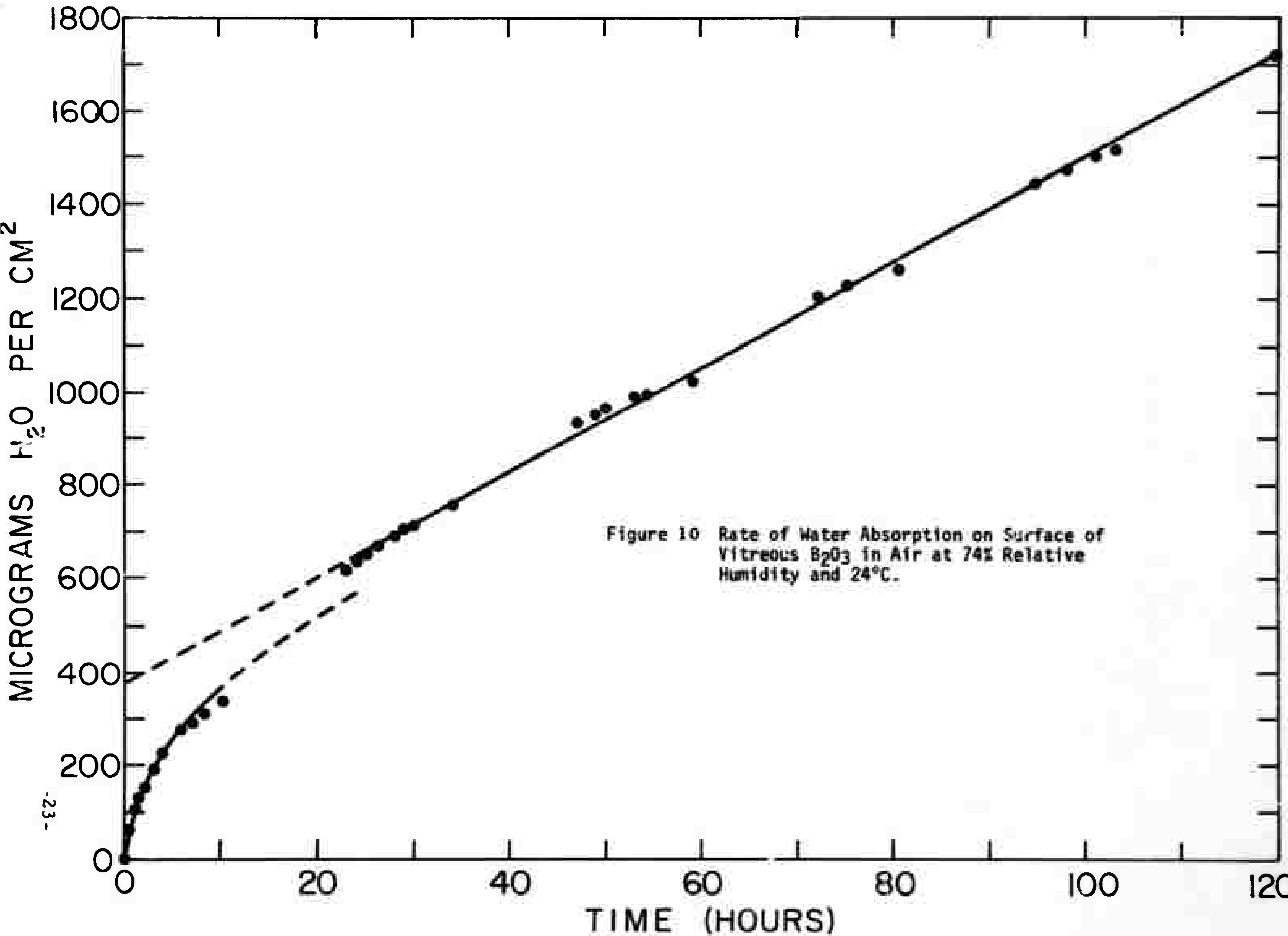

Figure 10 Rate of Water Absorption on Surface of Vitreous B_2O_3 in Air at 74% Relative Humidity and 24°C.

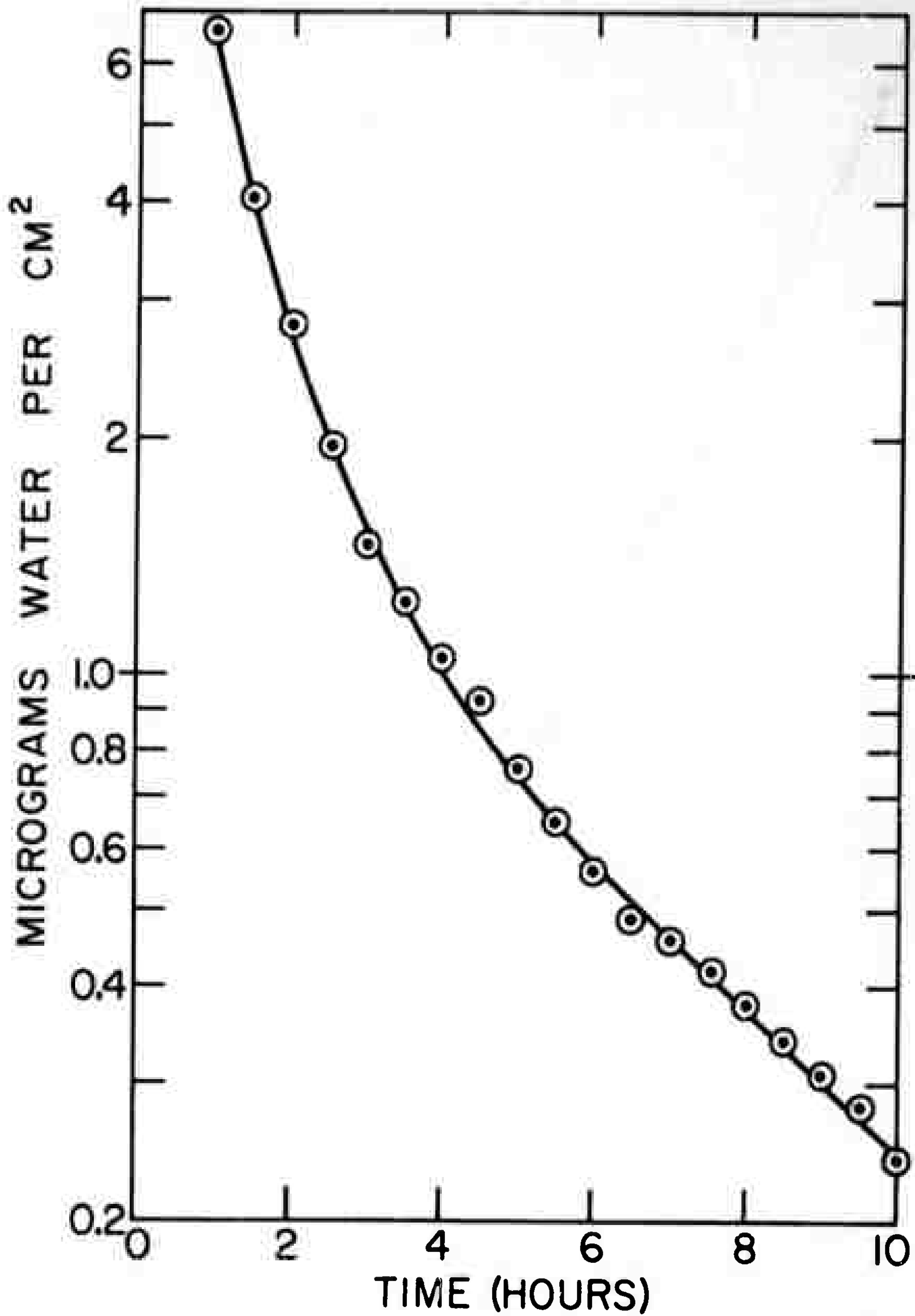

Figure 11 Rate of Removal of Surface Moisture in Vacuum at 24°C.

(Actually, the sample ampoule was lowered through a stationary heater.) This has been perfected to the point where crystals could easily be grown routinely (Table III). One objective of this research was to systematically study the influence of different growth parameters on the properties and perfection of the resultant crystals. A major obstacle to such studies has been the inability to view the positioning of the ampoule and the location of the solid-liquid interfaces. This has been overcome by use of the apparatus design shown in Figures 12 and 13. The heater was constructed by winding 22 guage Pt-10% Rh wire on a transparent fused silica tube. The space between the heater and the outer glass tube was initially empty, permitting accurate positioning of the ampoule. This space was then filled with bubbled alumina and the heater power turned on. The position of the zone was determined by operating for several hours and then quenching the zone by suddenly retracting the ampoule into the cooler portion of the apparatus and turning off all power. After cooling, the bubbled alumina was drained below the heater. The ampoule was then lowered to its original position, permitting location of the quenched zone relative to the heater, as shown in Fig. 14. In the preceding manner, it was found that the length of the feed and crystal can have a considerable influence on the relative positions of the interfaces, as shown in Figures 15 and 16. Thus it is seen that the seed should be longer, both to avoid excessive dissolution of the seed and to avoid an initial crystallizing rate greatly in excess of the ampoule lowering rate. Likewise the feed section should be longer than about twice its diameter to avoid rapid zone motion.

The shape of the growing interface is expected to depend on its position. One could approximately determine the macroscopic interface shape by breaking open the ampoules quenched as above. Unfortunately, *in situ* observation of the interface is not possible with high-temperature opaque material such as GaAs.

TABLE III.A. Summary of Early Travelling Heater Experiments on GaAs (July 1970-June 1971)

Run THM #	Heater Temp.	Original Seed length (cm)	Original Ga Zone length (cm)	Original Feed length (cm)	Lowering Rate (mm/day)	Results
1	1000°C	0.6 < 111 > direction	0.3	4.2	4.7	Seed was dissolved. Growth started by self seeding and grains grew inwards towards center where Ga inclusions were found. Total growth about 3.5 cm.
2	1010°C	0.6 < 111 >	1.0	2.5	4.7	Seed dissolved. Self seeded polycrystal measured 2.5 cm with large twinned crystals several mm in center. Evidence of nucleation near wall. No Ga inclusions.
3	1025°C	0.6 <111>	1.0	2.5	5.0	Seed dissolved. Large grain of 4 mm x 10 mm in center with polycrstalline nucleation near ampoule wall. No Ga inclusions. Total length 2.3 cm.
4	1055°C	0.3 <111>	1.0	2.0	5.0	Seed dissolved. Grains nucleated at bottom of ampoule and propagated along the length for 2.0 cm polycrystalline growth. No Ga inclusions.
6	1000°C	0.3 < 111 >	0.8	2.5	1.0	Growth was quenched after 1 cm growth from self seeding (seed dissolved). The quenched solid-liquid interface was convex and the ingot showed grain selection.

TABLE III.A. (continued)

Run THM #	Heater Temp.	Original Seed length (cm)	Original Ga Zone length (cm)	Original Feed length (cm)	Lowering Rate (mm/day)	Results
7	950°C	1.3 <110>	0.8	2.5	2.0	Successfully seeded. 90% of the 1.5 cm grown was single crystal of <110> direction.
9	935°C	2.0 <110>	0.8	1.5	5.0	Successfully seeded and grown 1.0 cm. Ingot began single but rapidly became polycrystalline due to the fast growth rate.
11	950°C	0.8 <110>	0.8	1.0	3.0	Successfully seeded and grown 0.8 cm. Ingot was in <110> direction and nearly completely single crystal.

TABLE III. B. Summary of Recent Travelling Heater Experiments on GaAs (July 1971 - June 1972)

Run THM #	Heater Temp.	Original Seed length (cm)	Original Ga Zone length (cm)	Original Feed length (cm)	Lowering Rate (mm/day)	Results
33	800°C	1.0	0.75	3.8	1.0	Ga zone detached after 0.8 cm growth indicating 800°C is too low for THM growth even at 1 mm/day.
45	850°C	1.0	0.75	3.8	1.0	Successfully completed 2.5 cm growth. Crystal quality poor indicating 650°C and 1 mm/day as lower limit for THM growth.
32	850°C	1.0	0.75	3.8	2.22	Ga zone detached after 1.0 cm growth, travel rate too fast for growth.
31	850°C	1.0	0.75	3.8	4.44	Ga zone detached after 0.7 cm growth.
51	980°C	1.0	0.55	3.8	1.5	Growth terminated after 0.5 cm growth due to power shutdown.
39	980°C	1.0	0.55	3.8	4.44	Successfully completed 3.5 cm growth. Polycrystalline with some Ga inclusion; travel rate apparently too fast for good quality crystal.
44	980°C	1.0	0.55	3.8	6.66	2.8 cm growth completed. Crystal very polycrystalline with traits of Ga inclusion.
52	980°C	1.0	1.0	3.8	1.5	Growth terminated after 1.7 cm growth due to power shutdown.
41	980°C	1.0	1.55	3.8	1.5	2.8 cm polycrystalline growth completed. Grains appeared to have nucleated on wall and grown towards center due to the concave solid-liquid growth interface. Trails of Ga inclusions present in center of crystal.

TABLE III. B. (continued)

Run THM #	Heater Temp.	Original Seed length (cm)	Original Ga Zone length (cm)	Original Feed length (cm)	Lowering Rate (mm/day)	Results
40	980°C	1.0	0.75	3.8	1.5	3.0 cm growth. Seeded crystals appeared to have grown outwards due to presence of convex solid-liquid growth interface. Quality of crystal good with no Ga inclusion.
70	1020°C	Self Seed	0.55	3.2	4.0	Self seed and completed 2.5 cm growth. No Ga inclusions found.
58	1100°C	1.0	0.55	3.8	13.2	Completed 2.0 cm growth. No Ga inclusion present. Such high growth rate still useable at 1100°C.

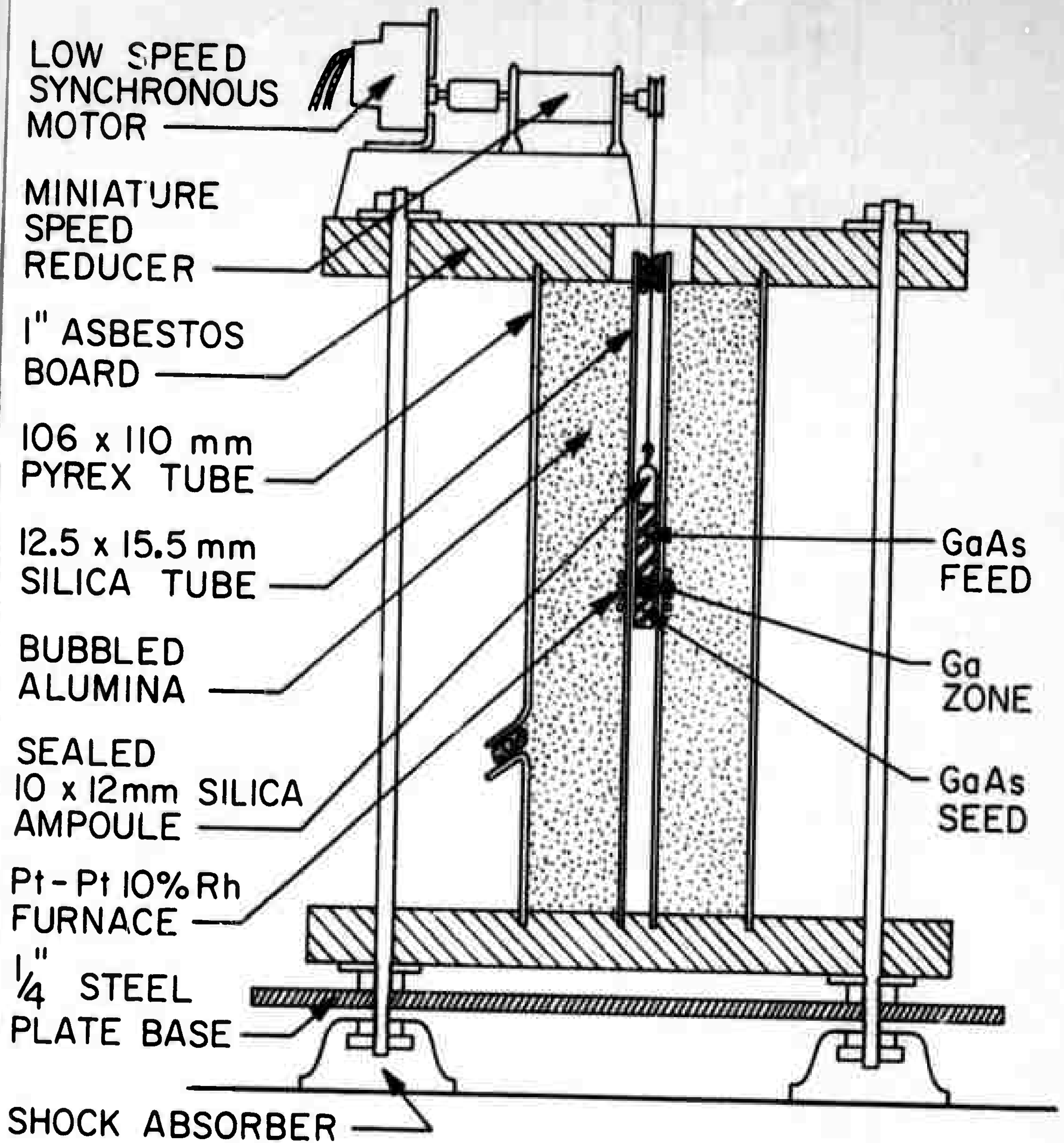

Figure 12 Diagram of the travelling heater apparatus for III-V crystal growth.

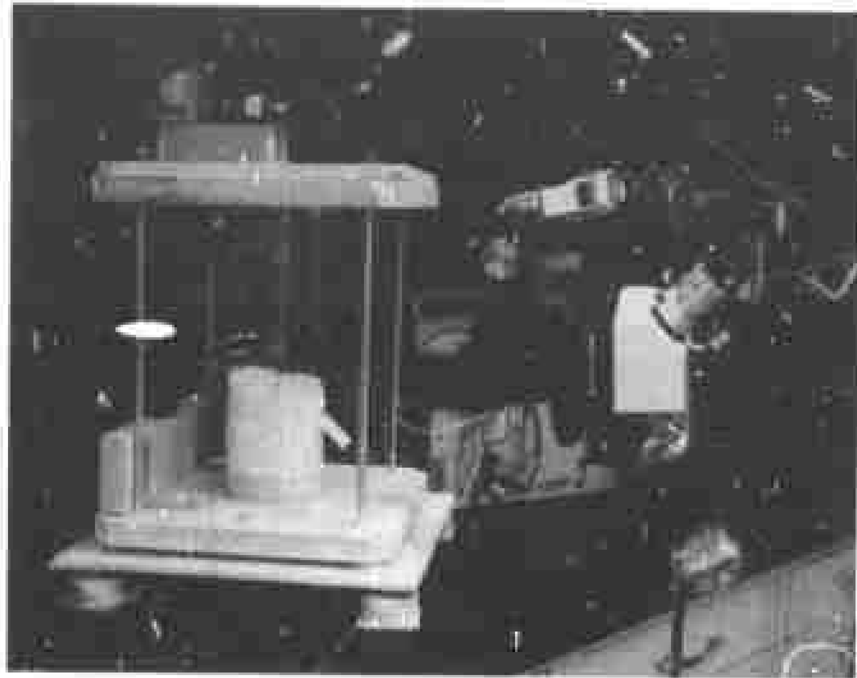

Figure 13. Photograph of travelling heater III-V growth apparatus, partially filled with bubbled alumina.

Reproduced from best available copy.

Figure 14 Photograph of quenched Ga zone.

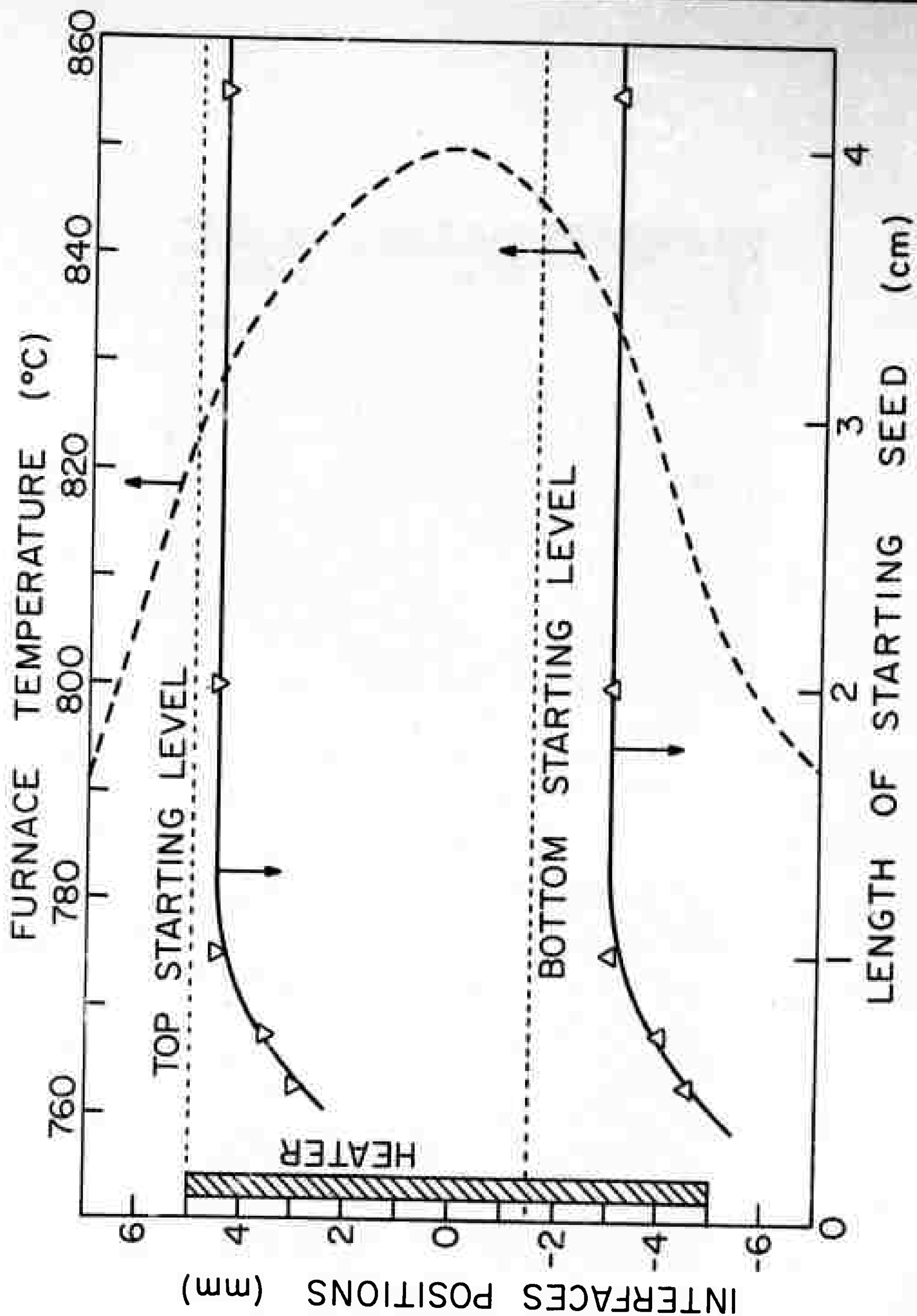

Figure 15 Position of the GaAs-Ga interfaces relative to the heater as a function of the initial length of the crystal below the solvent zone in the travelling heater method apparatus with zero travel rate and heater at 3.8 cm initial feed

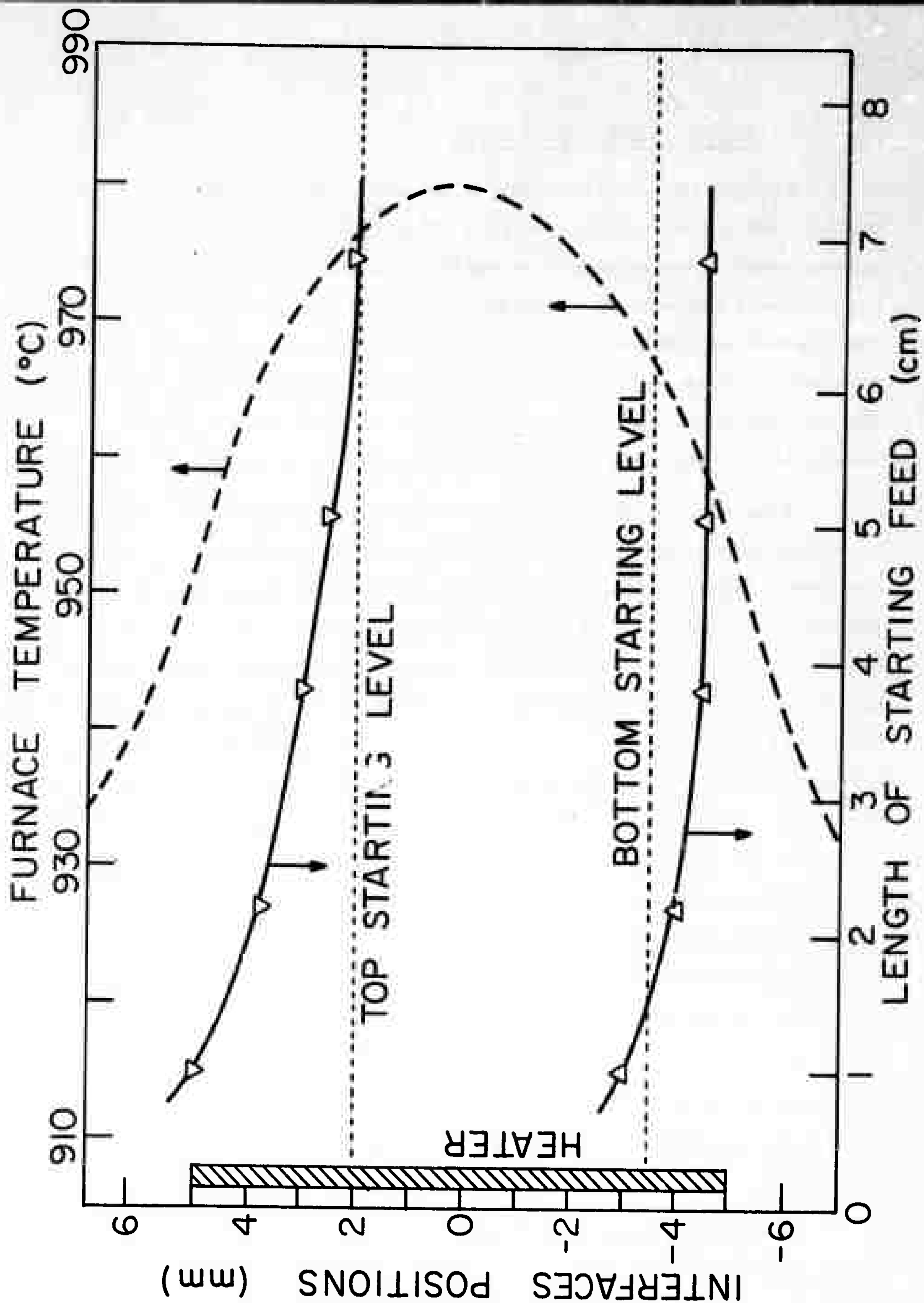

Figure 16 Position of the GaAs-Ga relative to the heater as a function of the initial length of the feed above the solvent zone in the travelling heater method apparatus with zero travel rates and heater at 980°C. 0.55 cm initial length of Ga. 1.0 cm initial length of seed below zone. 1 cm diameter tube.

2. Organic Analog and Theory

Experiments have been performed with a low-melting transparent organic analog system to permit easy observation of the interfaces and measurement of temperatures inside the ampoule. A diagram of the experimental apparatus is shown in Figure 17. The system investigated was crystalline naphthalene with benzoic acid as a solvent, yielding a maximum melting point of about 81°C (in the absence of benzoic acid). Microscopic observation revealed interface features such as grain boundaries and interface breakdown, as illustrated in Figure 18.

When the rate of lowering the ampoule was gradually increased, breakdown of the bottom interface and trapping of solvent was eventually observed. When the lower (growing) interface was convex, interface breakdown initiated at grain boundaries in the center of the tube and spread over the interface. At low movement rates the breakdown did not spread to the periphery, which lagged behind the center of the interface to produce shapes as shown in Figure 19. As the travel rate was increased further, the breakdown gradually covered more and more of the interface. When the zone length was less than the diameter of the tube, a hump formed on the top interface as shown in Figure 20. The position of the hump was sensitive to thermal conditions and rarely fell at the tube center. Breakdown of the bottom interface in such narrow zones began almost directly beneath the lump on the upper interface, indicating a strong free convection influence.

When the ampoule was raised then growth occurred on the upper interface, which was generally quite concave. Again when the rate of raising was gradually increased, the upper (growing) interface eventually broke down. However, in this case, breakdown began at the tube wall.

The critical travel rate V_c for initiation of interface breakdown was measured both for downward travel and for upward travel as a function of the zone composition. As shown in Figure 21 the critical travel rate decreased as the solvent content of the zone increased.

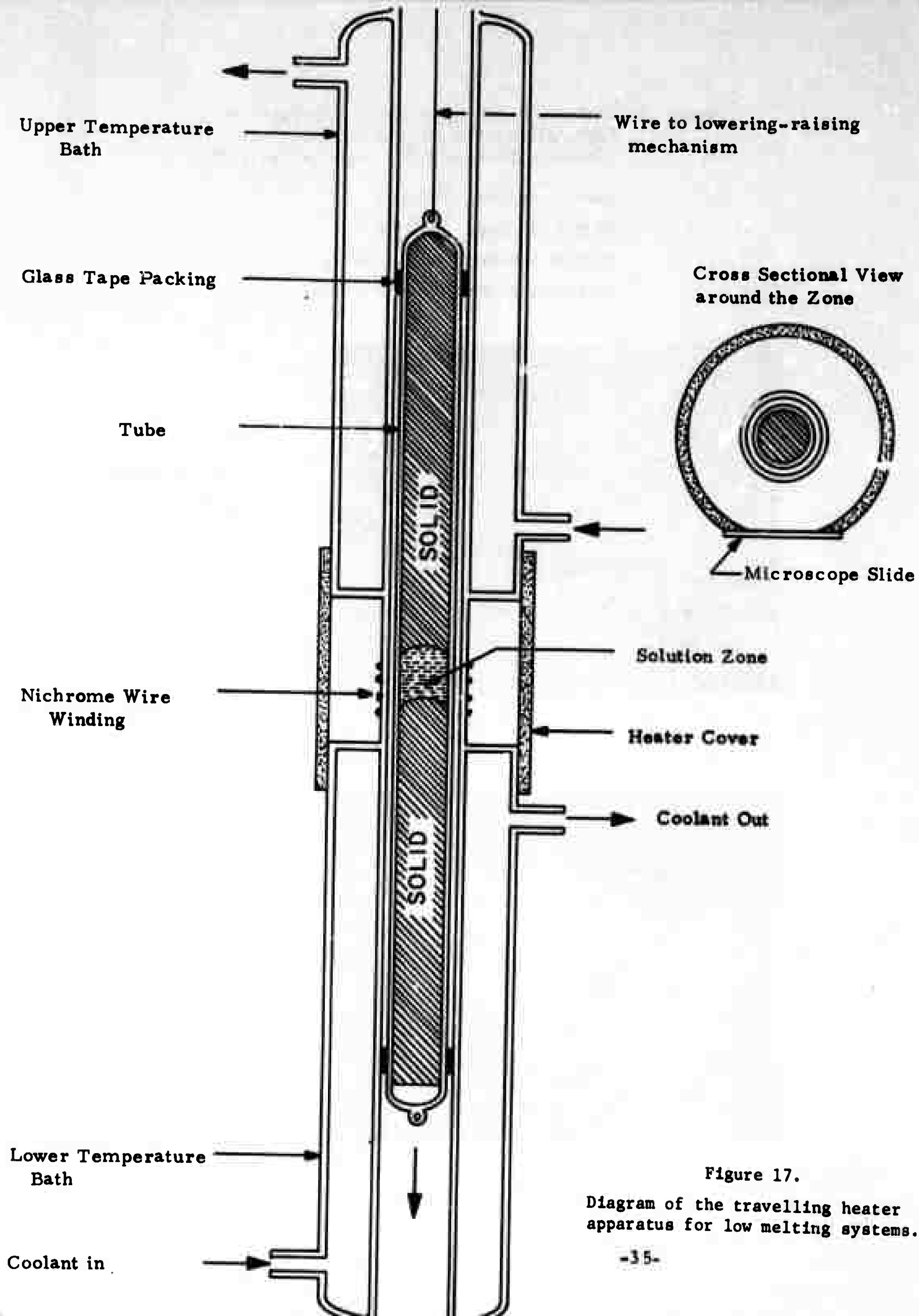

Figure 17.

Diagram of the travelling heater apparatus for low melting systems.

Figure 18 Photographs of the Growing Interface of Naphthalene with Benzoic Acid Solvent. (The dark bands are the heater wire) x 15

Tube diameter: 10.6 mm

Length of zone: ~10 mm

Solvent Concentration: ~25 wt.%

Temperature gradient: ~39°C/cm.

A. Smooth interface showing grain boundaries.

Travel rate: 10.2 mm/day

Reproduced from best available copy.

B. Interface after breakdown showing trapping of solvent.

Travel rate: 26.3 mm/day

A

C

Reproduced from
best available copy.

B

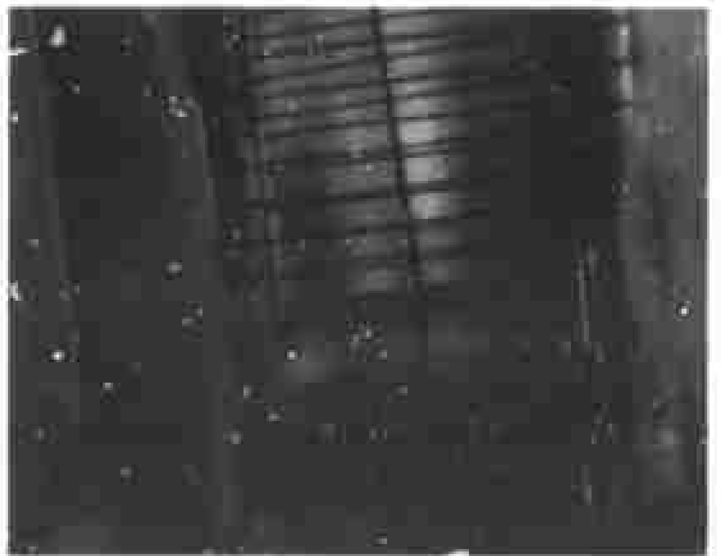

D

Figure 19 Breakdown and change of macroscopic shape of naphthalene-solution interface. 11.6 wt % benzoic acid in zone. 10.6 mm tube diameter. 23 mm zone length. A. Zero travel rate. B, C, D. Successive time intervals at a travel rate of 76.7 mm/day.

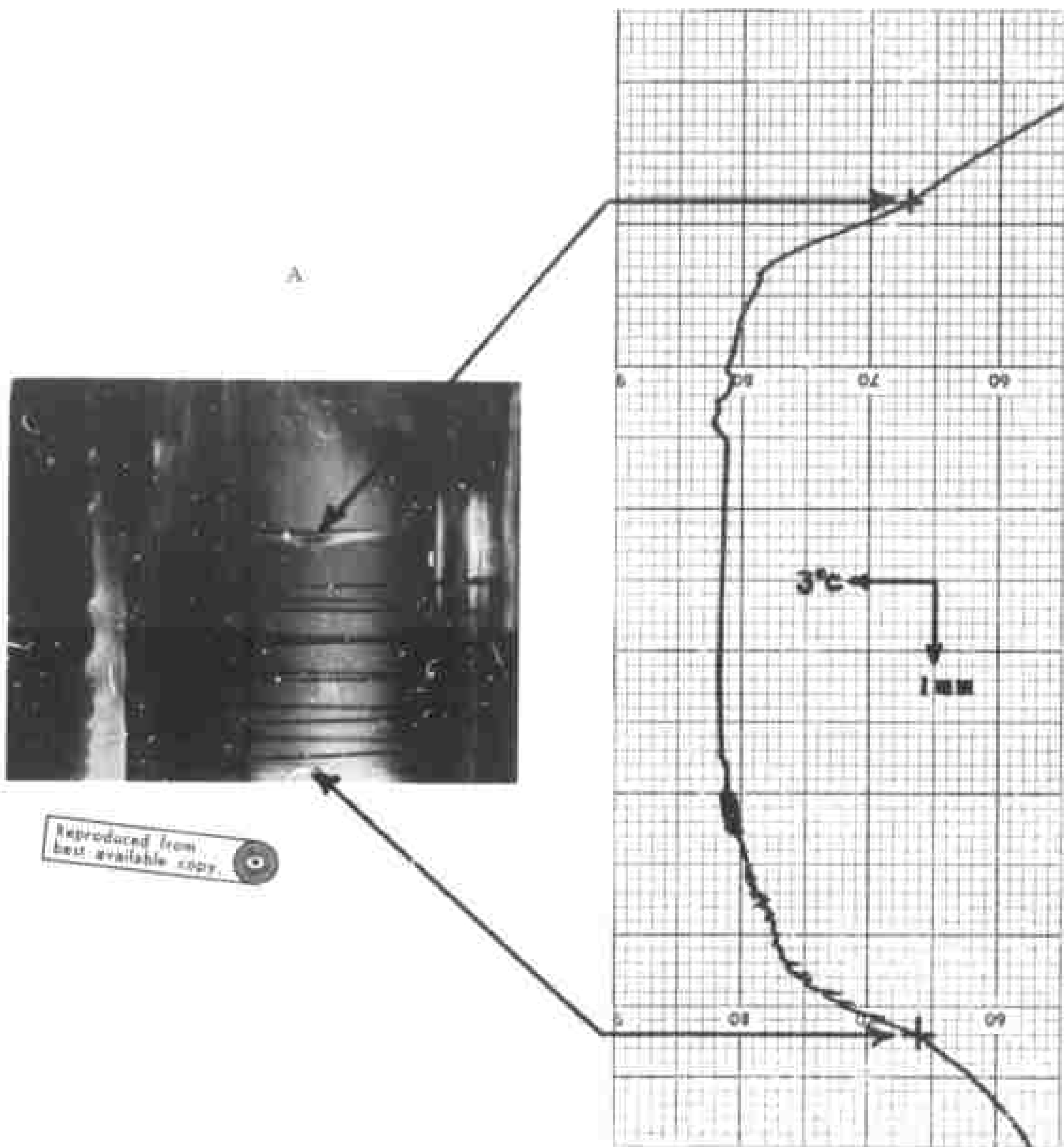

Reproduced from best available copy.

Figure 20 A narrow benzoic acid zone in naphthalene. A. Photograph showing hump on upper interface. B. Thermocouple recording during movement of solvent zone. (Thermocouple moving with ampoule relative to heater and zone).

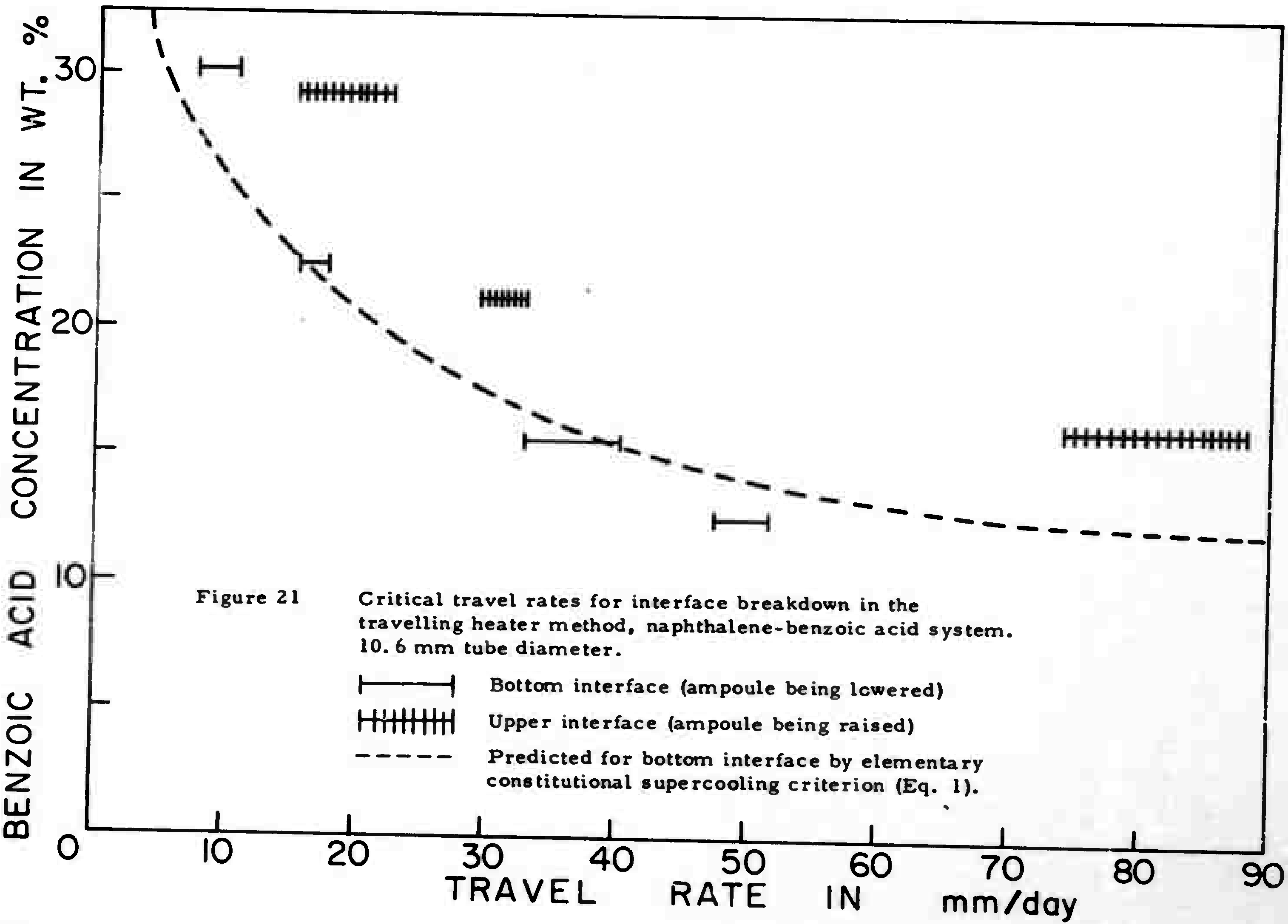

Figure 21 Critical travel rates for interface breakdown in the travelling heater method, naphthalene-benzoic acid system. 10.6 mm tube diameter.

The critical travel rate was substantially higher for the upper interface (ampoule raised) than for the bottom interface (ampoule lowered). The curve was derived theoretically for the bottom interface by combination of a one dimensional heat transfer analysis with the simple constitutional supercooling concept. The equation for this curve is

$$\frac{V_c m}{D}(C_z - C_s) = \frac{V_c \rho \Delta H_f}{k} + a_1\left[(T_h - T_c)\exp(-a_2\delta_b) - (T_h - T_i)\right] \quad (1)$$

where m is the slope of the liquidus, D is the diffusion coefficient for the solute, C_z is the interfacial solute concentration (assumed equal to the solute concentration of the bulk zone), C_s is the solute concentration in the solid, ρ is the density of the solid, ΔH_f is the latent heat of fusion, k is the thermal conductivity of the solid,

$$a_1 = \frac{1}{2}\left[\frac{V_c \rho C_p}{k} - \sqrt{\left(\frac{V_c \rho C_p}{k}\right)^2 + \frac{8h}{Rk}}\right. ,$$

$$a_2 = \frac{1}{2}\left[\frac{V_c \rho C_p}{k} + \sqrt{\left(\frac{V_c \rho C_p}{k}\right)^2 + \frac{8h}{Rk}}\right. ,$$

T_h is the heater temperature, T_c is the cold bath temperature, T_i is the interface temperature, C_p is the heat capacity of the solid, and δ_b is the height of the bottom interface above the bottom of the heater. When the heater power input to the zone was increased, the critical growth rate V_c increased for two primary reasons: the zone temperature increased, increasing the solute concentration in the zone (C_z), and the zone axis increased, decreasing the amount of the bottom solid inside the heater.

The interface positions as a function of travel rate and length L to diameter D ratio of the zone were observed, as shown in Figures 22 and 23. The length of the zone was changed by changing the heater power input, so that the higher L/D the lower was the solvent concentration. The bottom interface was always symmetrically convex, while the concave

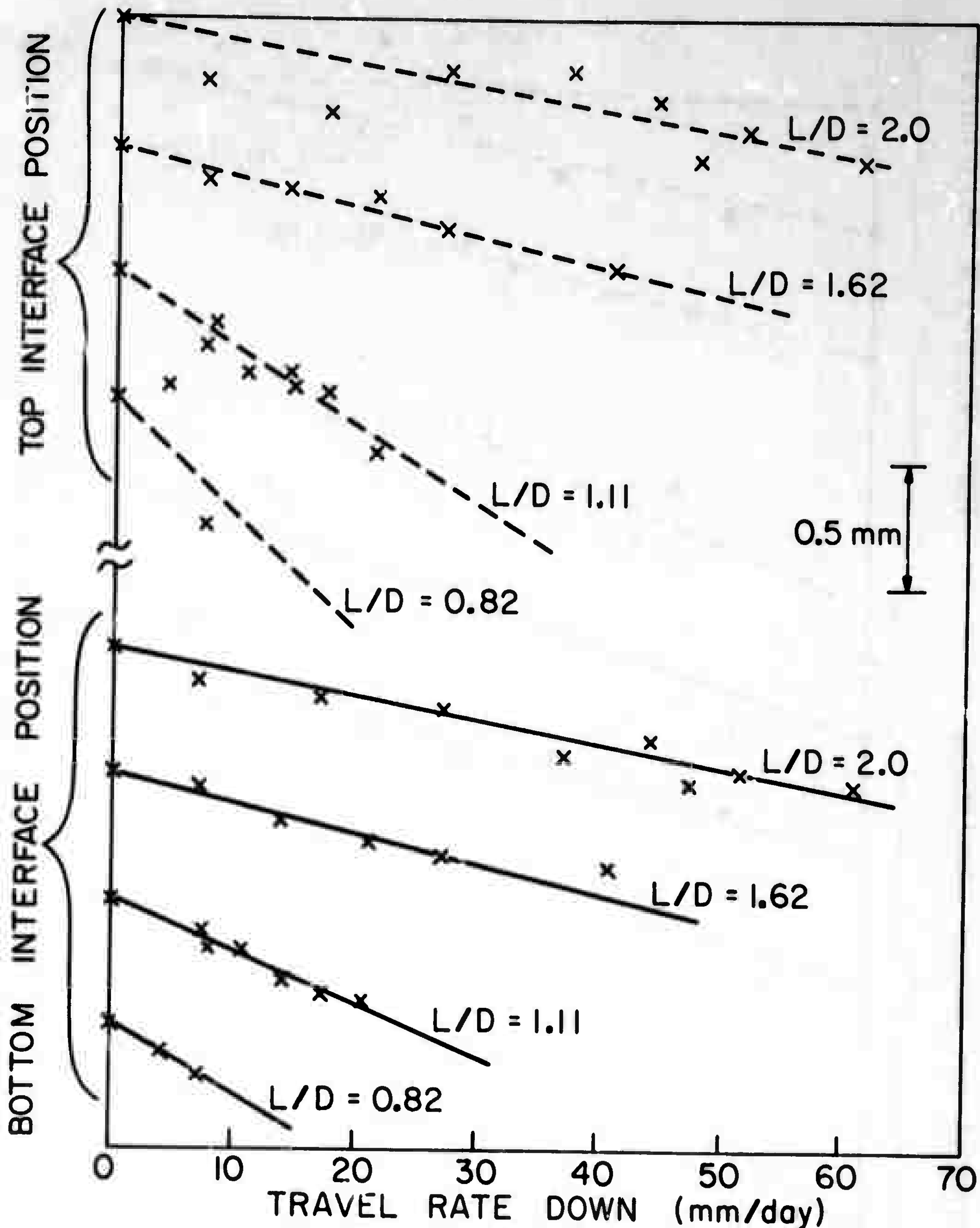

Figure 22 Shifts of steady state interface positions as a function of zone travel rate and length to diameter ratio of the zone for naphthalene with benzoic acid solvent. Ampoule being lowered. Solvent concentration decreased as L/D increased.

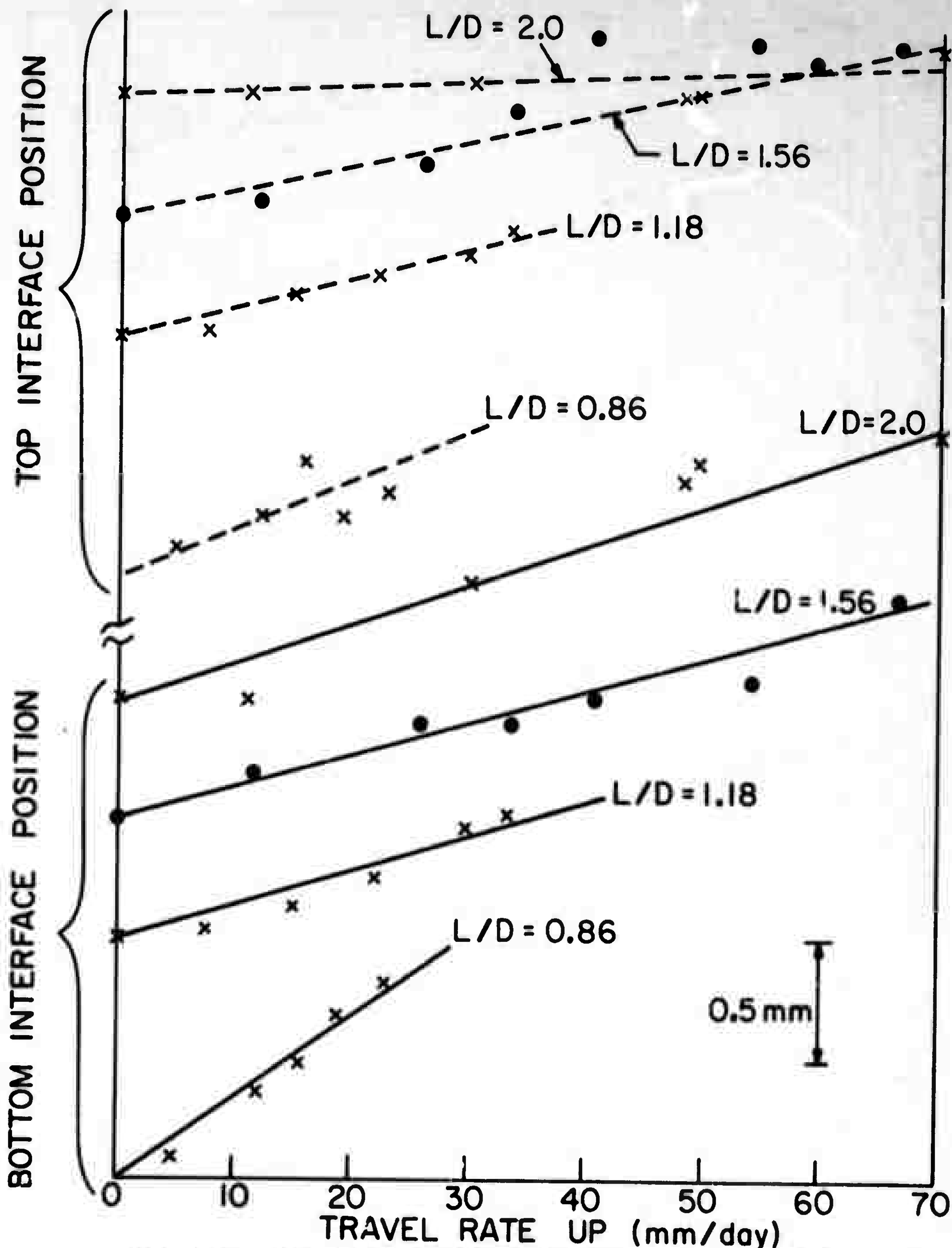

Figure 23 Shifts of steady state interface positions as a function of zone travel rate and length to diameter ratio of the zone for napthalene with benzoic acid solvent. Ampoule being raised. Solvent concentration decreased as L/D increased.

top interface was often nonsymmetrical and highly skewed to one side. The dependence of interface position on travel rate increased as the zone length to diameter ratio decreased. When the zone contained only molten naphthalene, the dependence of interface positions on travel rate was about one-fourth the dependence when benzoic acid solvent was present. This indicates that the shift in zone position was caused primarily by mass transfer resistance when solvent was present. Nevertheless, the temperature difference between top and bottom interfaces never exceeded $\sim 2^{o}C$.

In order to separate heat and mass transfer effects, experiments were also performed with no solvent present, i.e., zone melting. Temperatures were measured by insertion of the two leads of very fine copper-constantan thermocouple wire through small holes in opposite sides of the tube. The junction was formed at the axis. The thermocouple leads ran along the tube in opposite directions. These precautions were taken to reduce errors caused by conduction down the thermocouple wire. At low travel rates the temperature in the zone was relatively independent of position, i.e., relatively flat temperature profiles were obtained as shown in Figure 24. At higher travel rates, the temperature varied significantly through the zone. The positions of the center and peripheries of the interfaces were also measured as a function of zone travel rate, as shown in Figures 25A and B. Heat transfer coefficients h were cal from measured temperatures using the heat balance

$$h(T_z - T_i) = -kG_s \pm V \rho \Delta H_f , \quad (2)$$

where G_s is the temperature gradient in the solid at the interface. These are shown as points in Figures 25A and 25B. Heat transfer coefficients were also calculated from the shift in interface positions for lowering of the ampoule, using one dimensional heat transfer analyses. These are shown as the curves in Figure 25A. Agreement between the

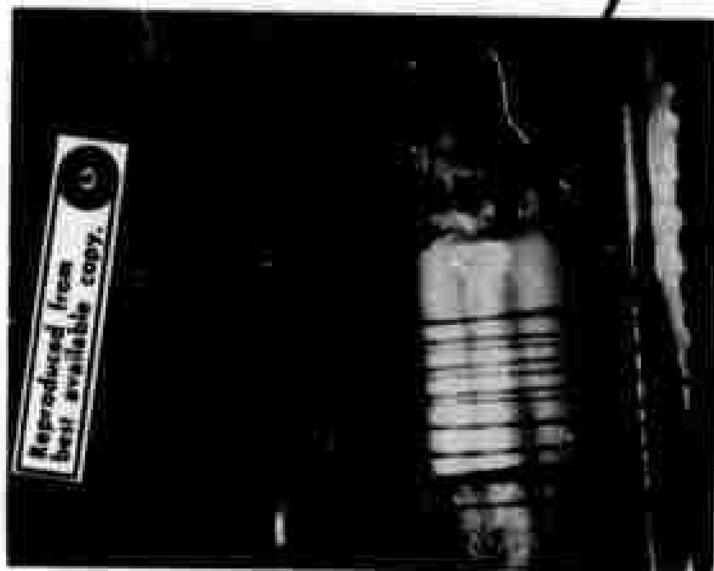

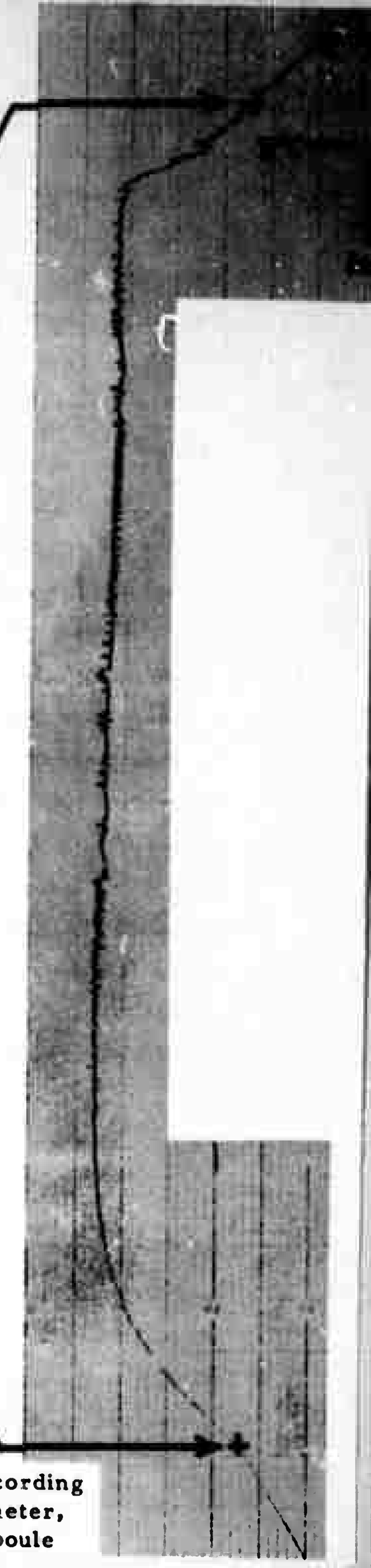

Figure 24 Photograph of molten zone and axial temperature recording for zone melting of naphthalene. 10.6 mm tube diameter, 14.0 mm zone length, 3.24 mm/hr. travel rate (ampoule lowered).

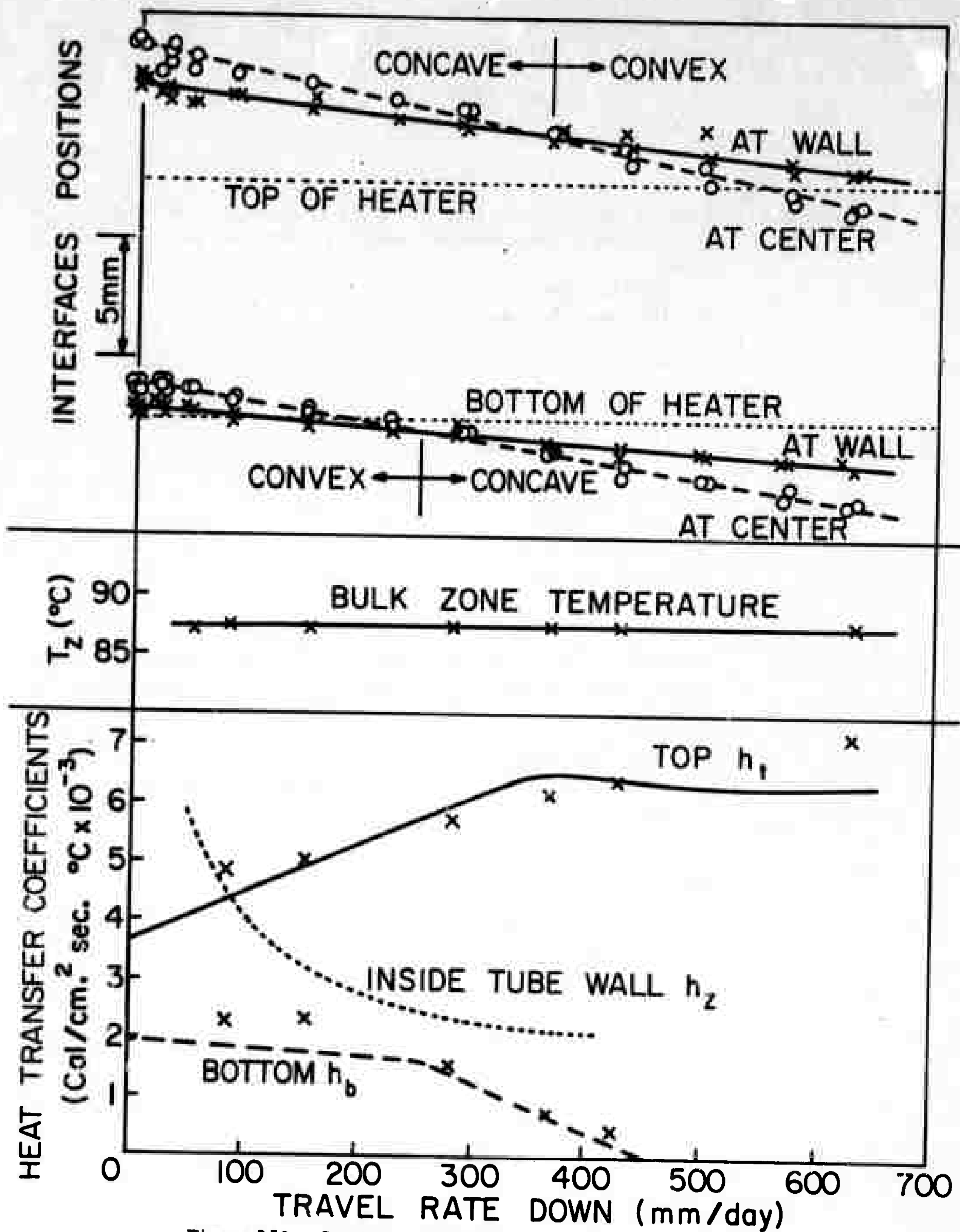

Figure 25A. Caption on following page.

Figure 25A Zone parameters for travelling heater method growth of naphthalene without solvent (zone melting). Ampoule being lowered.

A. Interface positions;

B. Bulk zone temperature T_z;

C. Heat transfer coefficients for bottom interface (h_b), top interface (h_t), and inside tube wall to zone (h_z).

X - from temperature recordings and interface heat balance.

--- - from interface positions and one-dimensional heat transfer analyses.

(On Preceding Page)

Figure 25B Zone parameters for travelling heater method growth of naphthalene without solvent (zone melting). Ampoule being raised.

A. Interface positions;

B. Bulk zone temperature T_z;

C. Heat transfer coefficients determined from temperature measurements and interface heat balance.

(On Following Page)

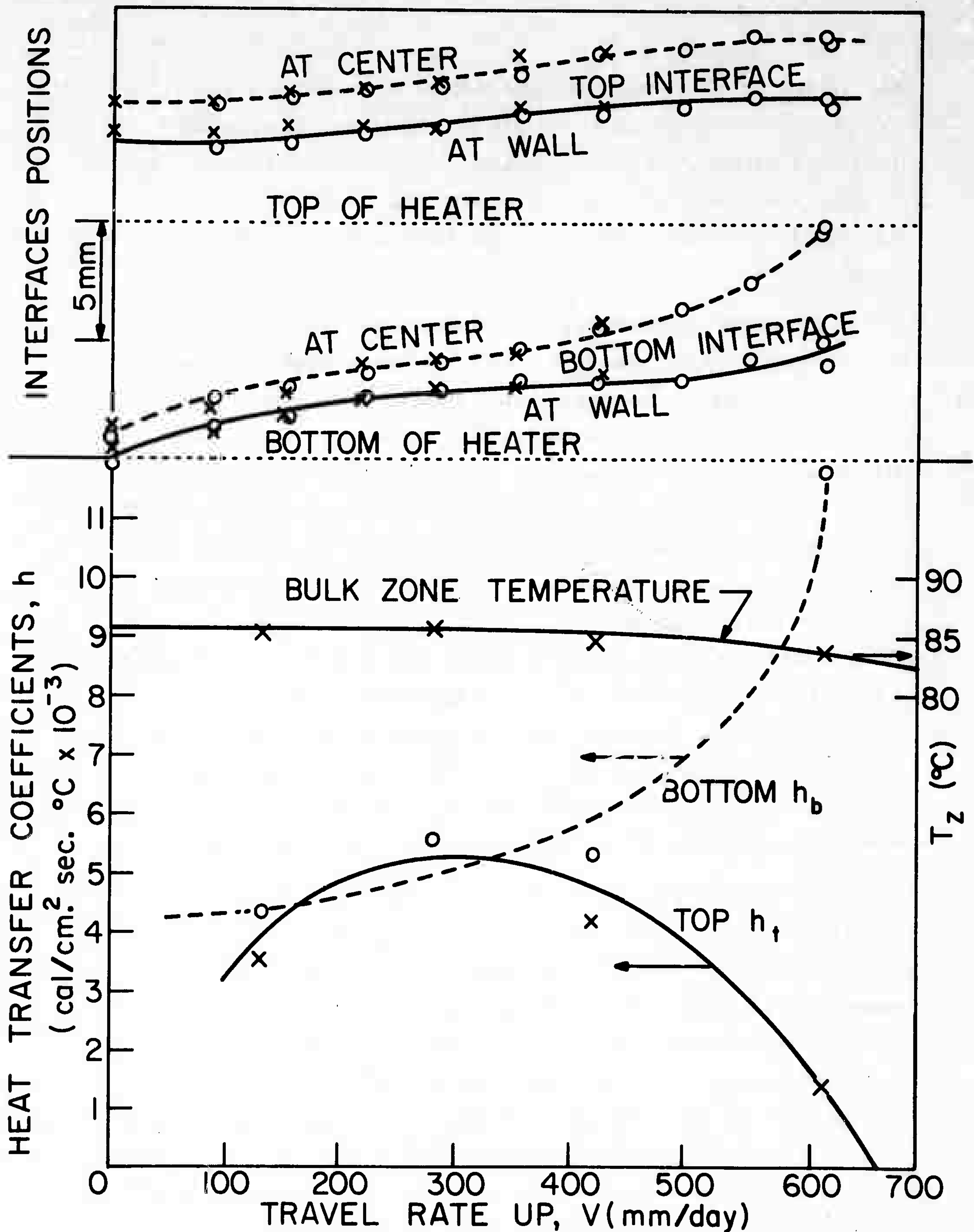

Figure 25B. Caption on preceding page.

heat transfer coefficients determined in these two manners is good, except when the interface was very convex. Partly the discrepancies reflect the failure of the one-dimensional assumption for the heat transfer analyses when the interface is very curved, and partly they reflect the fact that there was not a sharp transition from heater to cooler as assumed in the analyses.

Temperature recordings also served to reveal irregularities in the free convection patterns in the zone. For zones longer than the tube diameter temperature fluctuations were sizeable in the middle of the zone, smaller at the top, and negligible near the bottom (Figure 26). Observation of small particles present in the melt showed that convection currents arose from the heated walls and fell down the center from the cooled upper interface. As noted earlier, zones shorter than the tube diameter exhibited a small convex bump in the upper interface. A vigorous fluid stream moved downward from this bump, sometimes leading to a local concavity in the bottom interface. As shown in Figure 20, temperature fluctuations were large at the bottom of the zone and negligible at the top in this case. Generally speaking, the magnitude of the temperature fluctuations increased as the size of the zone increased. Disturbances were generated particularly when the zone protruded above the top of the heater, due to movement of convection currents upward from a heated tube wall into a cooled region.

Our main operating hypothesis thus far has been that a concave interface is deleterious to single crystal growth, since, on one hand, new grains nucleated at the wall will propagate to the center, while, on the other hand, grain selection is made more difficult. A subsidiary part of this hypothesis is that a concave interface is favored when the interface lies within a cooler, and conversely a convex interface is favored when the interface lies within the heater. These concepts have been borne out in travelling heater growth of naphthalene. Fortunately, with naphthalene-benzoic acid the bottom interface lay within the heater because of free convection and was convex, aiding in grain selection. Many streaked

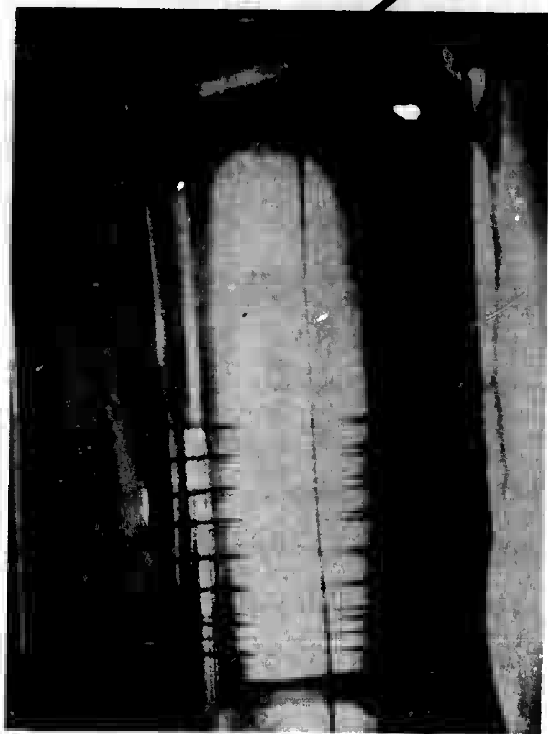

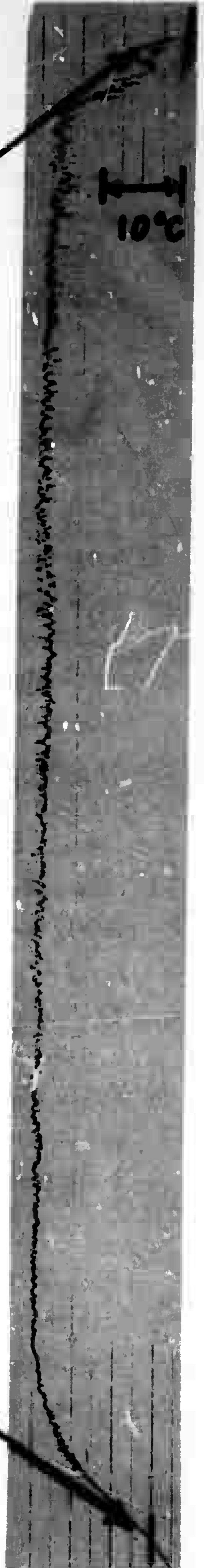

Reproduced from best available copy.

Figure 26 Zone shape and axial temperature profile for 9.2 wt % benzoic acid zone, with a zone length of 29 mm and a travel rate of 2.55 mm/hr.

grains developed at the upper interface with tube lowering when the interface was slightly concave or convex. In the absence of benzoic acid solvent, a concave bottom interface could be formed by use of a sufficiently high growth rate. Under such conditions streaked grains were again produced. The nature of these streaked grains is unknown at present.

E. Gradient-Freeze Crystal Growth of GaAs

1. Experimental

Cylindrical rods of GaAs were required for both the travelling heater and floating-zone experiments. At first these were cut from horizontal-Bridgman-grown crystals. The close tolerances needed for the travelling heater method necessitated tedious grinding. It was found that suitable ingots could be cast in fused silica tubes by melting and slowly turning the power down in the globar furnace shown in Figure 27. An evacuated and sealed tube was placed around the open tube containing the GaAs as shown in Figure 28 in order to prevent escape of arsenic vapor. Both GaAs and elemental Ga and As were used as starting materials. When Ga and As were employed, the Kanthal furnace shown in Figure 27 was first brought up to about 610°C and maintained at that level in order to control the arsenic vapor pressure at about one atmosphere. The lower globar furnace was then slowly raised to slightly above the melting point of GaAs. After a GaAs melt had been attained for several hours the furnace was turned down at 0.3 to 3°C/min. With a furnace temperature gradient of about 6°C/cm in the furnace, the estimated solidification rate was about 0.05 to 0.5 cm/min.

After the above casting procedure, generally intact ingots (Table IV, Fig. 29) of up to 17 cm long were removed from the inner tube, which was frequently cracked. Pre-coating of the tube with carbon (by pyrolysis of acetone) eliminated tube fracture, but was not generally employed because of the probability of carbon and silicon contamination. Much to our initial surprise, roughly the top half of each ingot was a single crystal

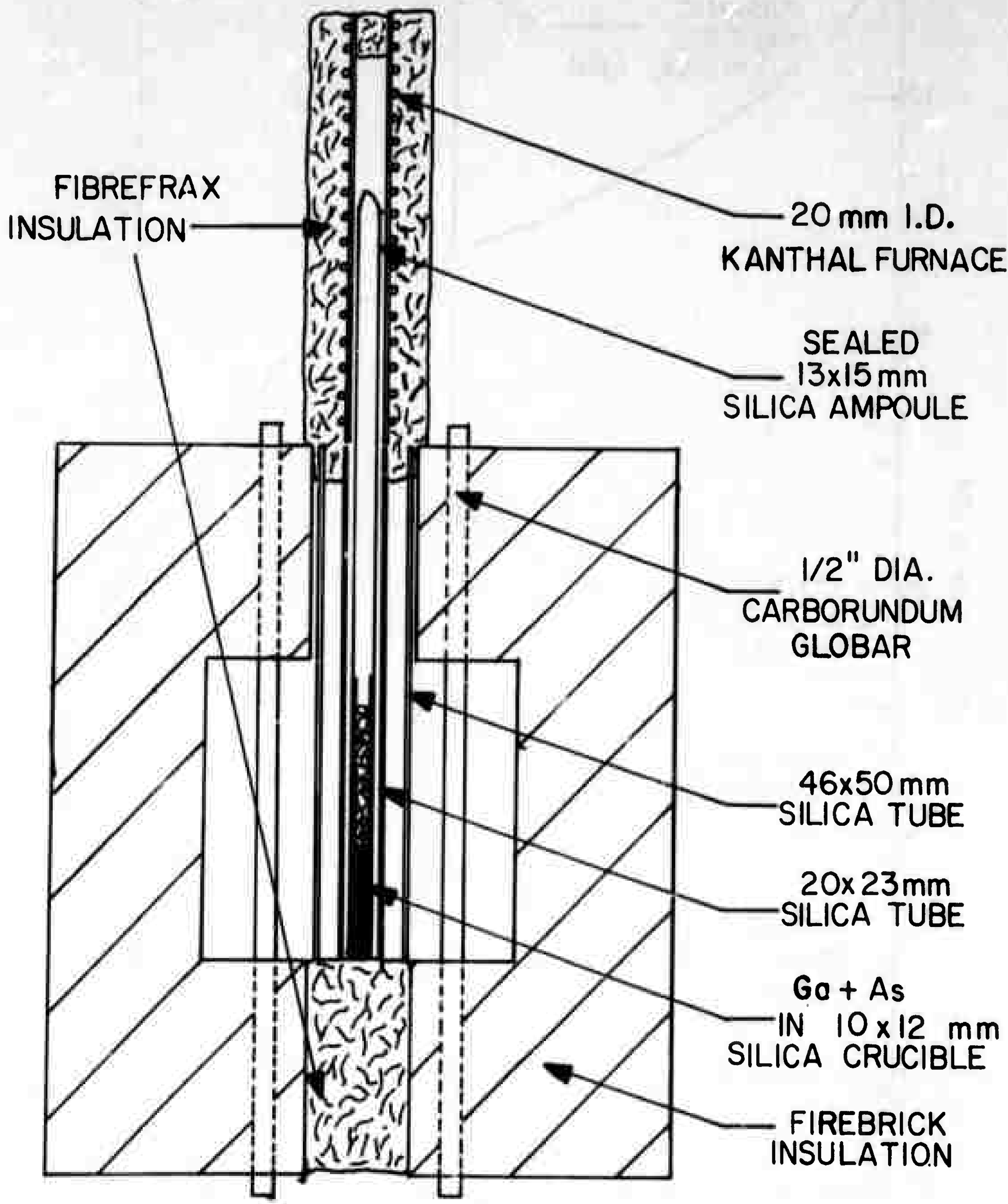

Figure 27 Diagram of gradient-freeze apparatus for GaAs.

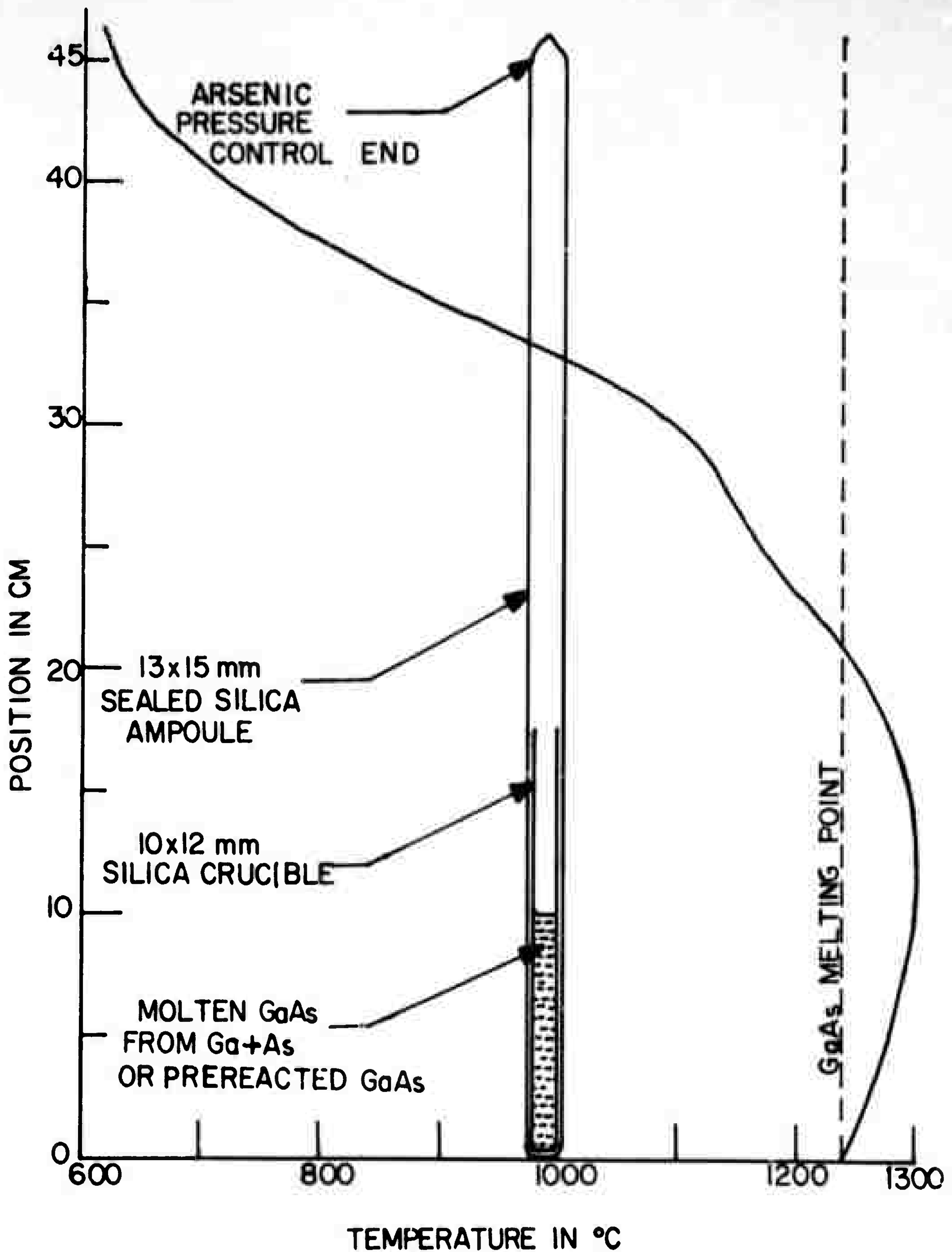

Figure 28 Ampoule and furnace temperature profile used for gradient freeze growth.

TABLE IV

GaAs Grown by Vertical Gradient Freeze Method

Ingot	Starting Material	Cooling Rate	Result
GF-1	Horizontal boat grown GaAs (undoped)	3°C/min.	n type low resist.
GF-25	Czochralski grown GaAs (undoped)	3°C/min.	n type low ρ
GF-30	6 nine purity Ga + As	0.3°C/min.	n type high ρ
GF-31	6 nine purity Ga + As	0.3°C/min.	n type low ρ
GF-32	Czochralski grown undoped GaAs	0.3°C/min.	n type low ρ

TABLE V

Semiquantitative Analyses (Weight Percent)

	GF-1	GF-25	GF-30	GF-31
Ga-	Rem. --->			
As-	4[illegible]. %	49. %	48. %	48. %
Si-	nil	TR < 0.002	nil ---------------->	
Mg-	nil	TR < 0.0001	nil ---------------->	
Cu-	ND < 0.00002	0.000058	0.000041	0.000049
Ca-	0.00022	0.00045	0.00021	0.00042
Li-	ND < 0.005 --------------------------------->			
Te-	ND < 0.10 ---------------------------------->			
Other Elements-	nil -->			

ND = not detected
TR = trace

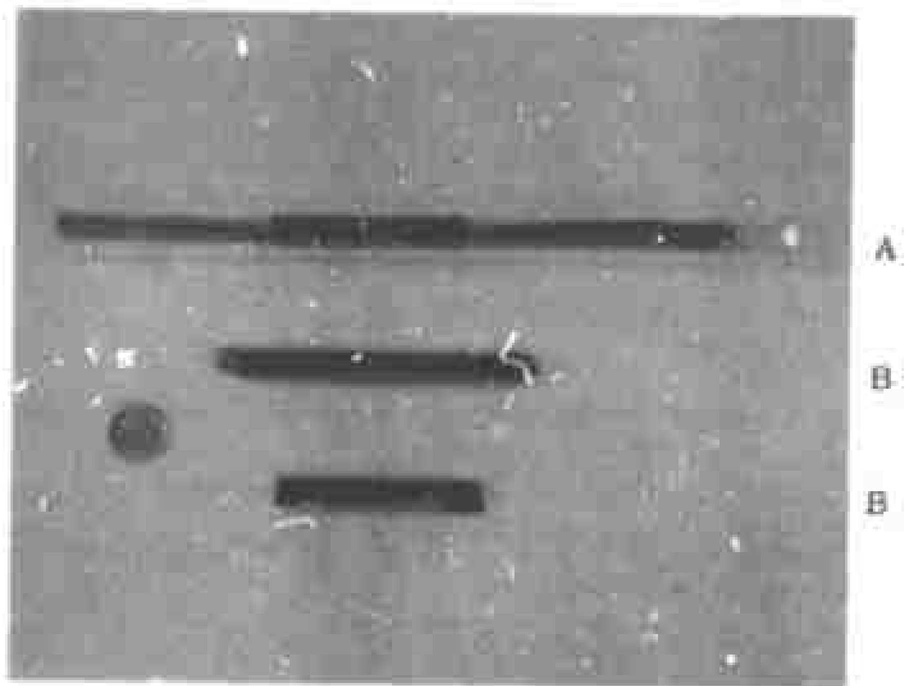

Reproduced from best available copy.

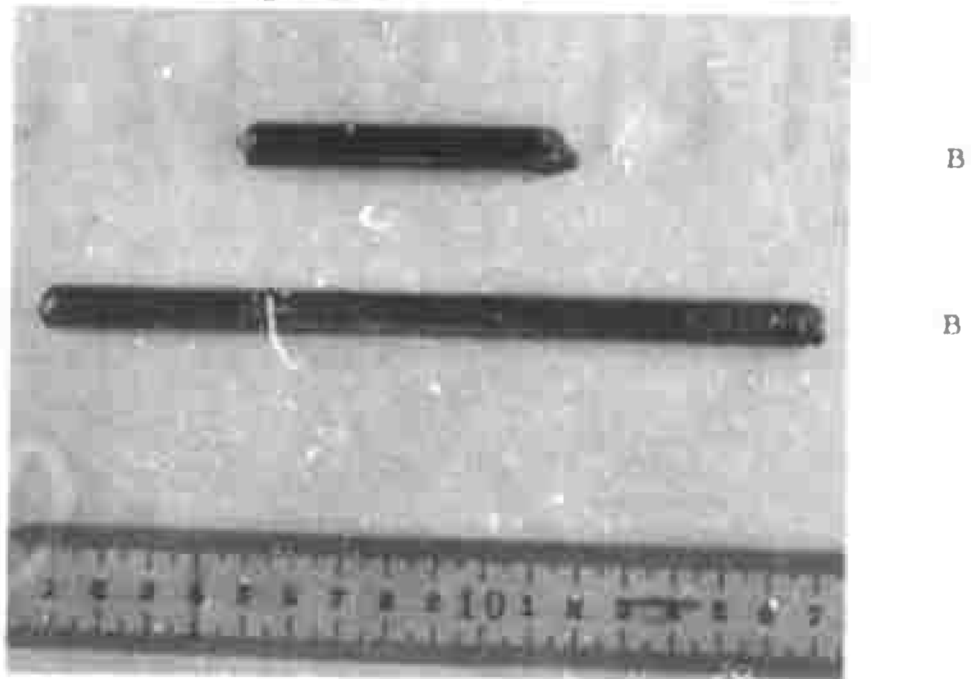

Figure 29 GaAs ingot cast by vertical gradient freeze technique.
A. Assembled ampoule before casting;
B. Cast ingots.

or occasionally a bi-crystal (6). Apparently, nucleation occurred at the bottom of the tube and growth proceeded upward with grain selection.

Frequent macroscopic defects when pre-reacted GaAs was used as a feed were voids along the periphery of the ingot as shown in Figures 29 and 30A. These are thought to be caused by trapping of gas bubbles during melt-down. An occasional defect was a central void or crack, as shown in Figure 30B. We cannot agree on the origin of this defect. One hypothesis is that gas bubbles were trapped at the center of an extremely concave interface. Another hypothesis is that cracking resulted from the thermal strain associated with an extremely convex interface. Dislocation densities in cast crystals ranged from 10^5 to about $10^6/cm^2$.

Undoped crystals were n-type. Cathodoluminescence was used to investigate the uniformity of these crystals. Figure 31 shows two scans at 2 mm intervals across a (110) plane cut at 25° to the growth direction of undoped crystal GF-25. The cathodoluminescence results shown in Figure 32 strongly suggested cellular solidification, which would be expected from the very rapid freezing rates employed. Crystals were also analyzed by emission spectroscopy, as shown in Table V. Starting material for GF-1 was from a horizontal Bridgman ingot while feed for GF-25 was prepared by our Czochralski technique. The higher impurity content of GF-25 is felt to reflect the greater handling of the pre-reacted material. GF-30 and GF-31 were grown from high purity Ga and As and show lower impurity contents. For comparison, horizontal Bridgman and Czochralski GaAs not only contained more Cu and Ca, but also detectable amounts of other impurities such as Si, Mg, Fe, Li and Al.

2. Theory

As noted earlier, our basic hypothesis is that, in solidification inside a tube, a concave freezing interface yields polycrystalline growth while a slightly convex interface results in single crystal growth. To the first approximation, a concave interface is expected when the crystal

Reproduced from best available copy.

A B

Figure 30 Defects in GaAs ingots cast by vertical gradient freeze technique.
A. Voids at periphery;
B. Central void or cracks.

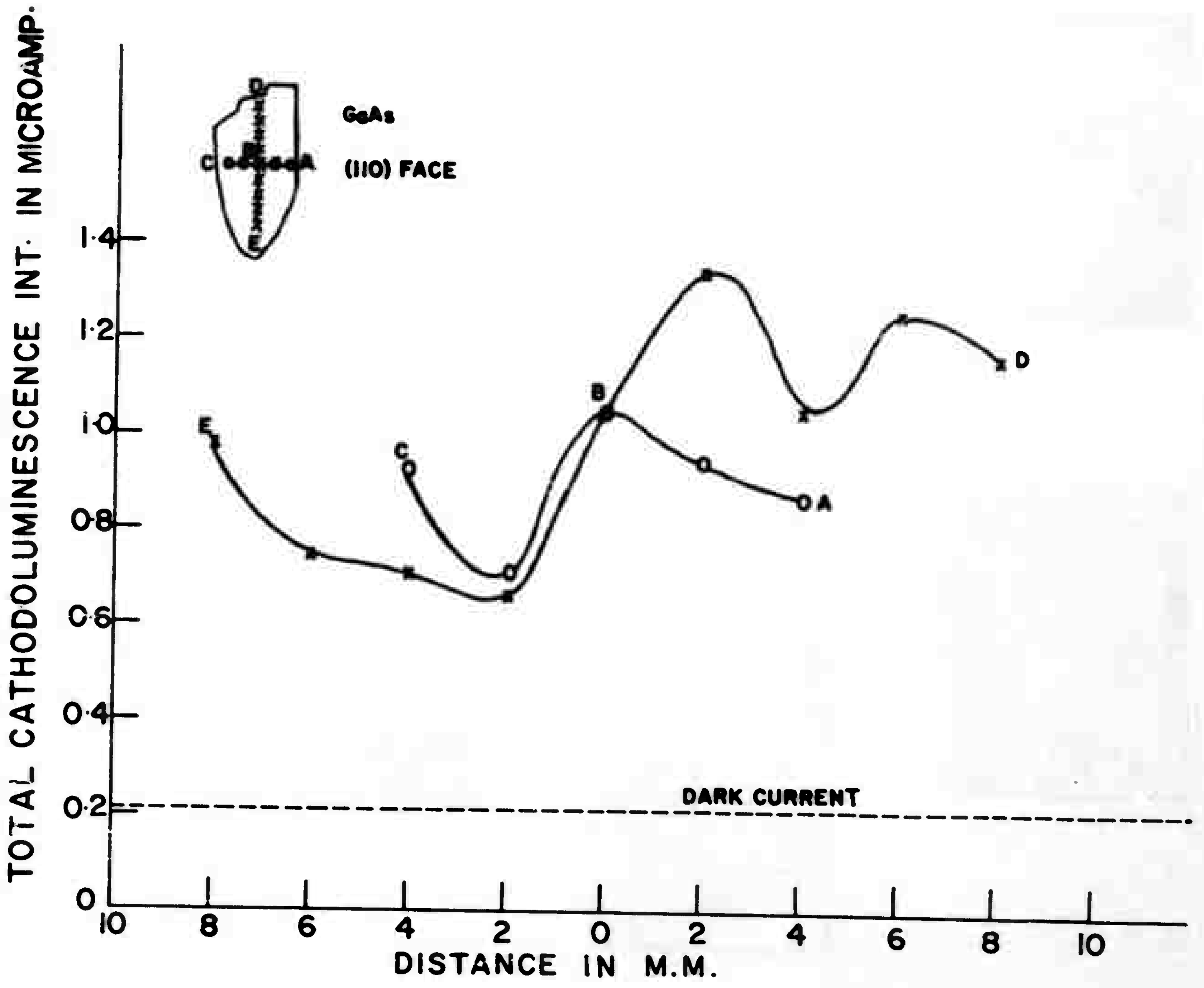

Figure 31 Cathodoluminescence intensities at 2 mm intervals in scans across (110) face of gradient freeze grown GaAs crystal GF-25.

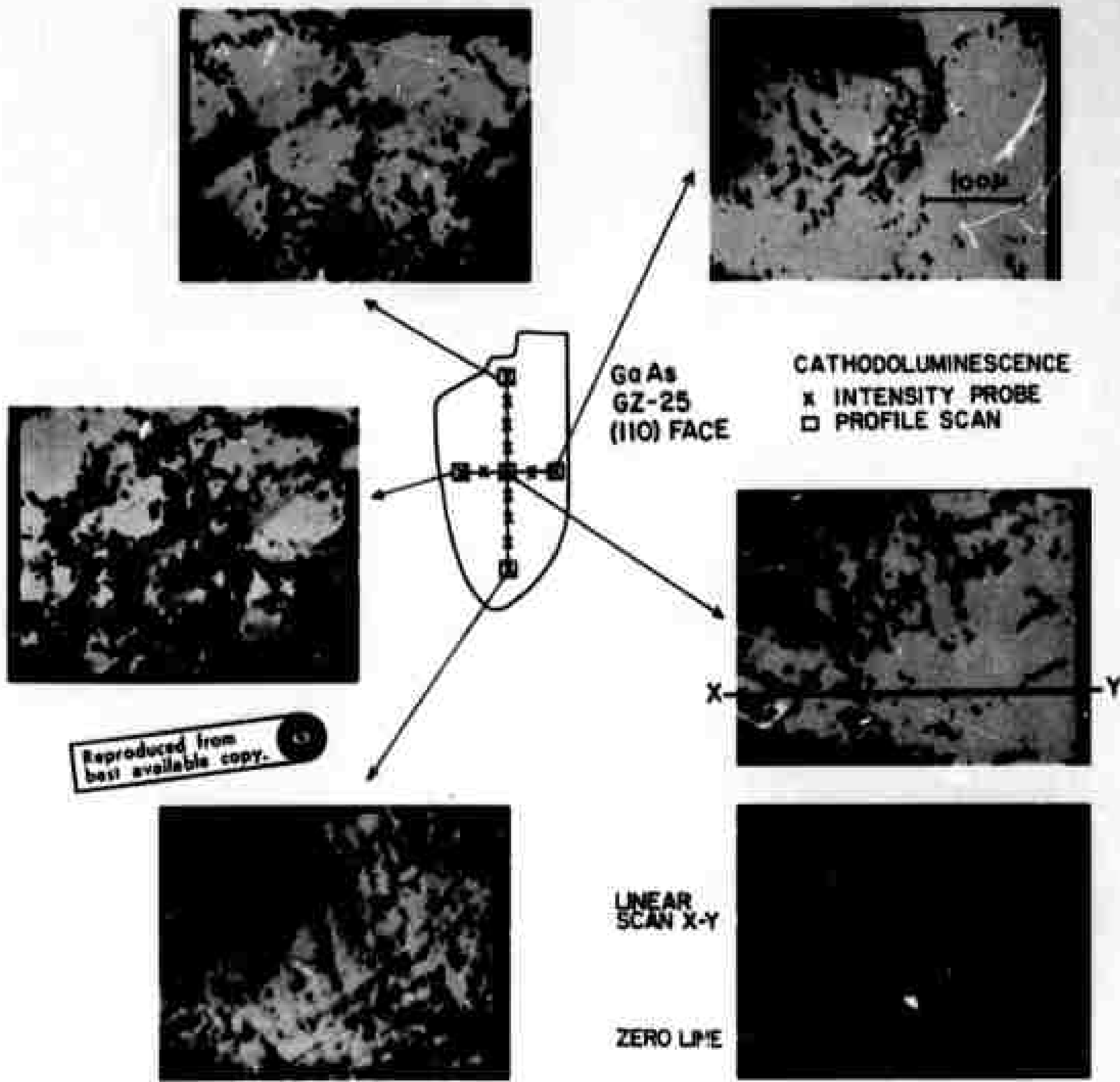

Reproduced from
best available copy.

Figure 32 Cathodoluminescence of gradient freeze-grown GaAs.

surface adjacent to the interface loses heat to the surroundings (5). Thus one may expect to gain some insight into a solidifying process by finding the furnace temperature adjacent to the interface. We have done this by an approximate one-dimensional solution of the heat transfer problem for gradient-freeze growth (6, 7). The absence of convection in the melt was assumed, which is reasonable with a vertical tube which is cooler at the bottom. When the interface is many tube diameters from the ends of the tube it is predicted to become more concave as the freezing rate is increased, because of latent heat liberation. At very low growth rates the interface should be convex only if the thermal conductivity of the solid k_s is greater than that of the liquid k_ℓ. Unfortunately, the reverse is true for the III-V's. A calculated temperature profile for GaAs is shown in Figure 33, with heat transfer parameters taken to be freezing rate $V = 0.85$ cm/min., Peclet number for solid $\beta_s = \theta\rho_s C_{ps} R/G k_s = 0.0144$, $\beta_\ell = \theta\rho_\ell C_{p\ell} R/G k_\ell = 0.0048$, Biot number for solid $H_s = hR/k_s = 0.0392$, $H_\ell = hR/k_\ell = 0.0131$, and the latent heat parameter is $\omega = \Delta H_f/GRC_p = -291.5$. Here θ is the rate of temperature change at any point in the furnace, G is the temperature gradient in the furnace, h is heat transfer coefficient between tube and furnace and ΔH_f is the latent heat.

In order to find an analytical solution for a finite tube length it was necessary to neglect the latent heat and to assume the properties of solid and liquid are the same. The heat transfer coefficient h was taken to be constant over cylindrical and end surfaces. The problem is shown schematically in Figure 34. The interface is predicted to be concave initially and convex at the end. The parameter δ_o is the distance between the cold end of the tube and the point in the furnace having the same temperature as the end of the tube. As δ_o increases, the initial interface shape becomes more concave. The dependence of δ_o on the heat transfer parameters is shown in Figure 35. From this one finds that the interface should become more concave as the cooling rate increases, as the temperature gradient decreases, as the thermal conductivity increases, and as the length of the tube increases. The difference between the

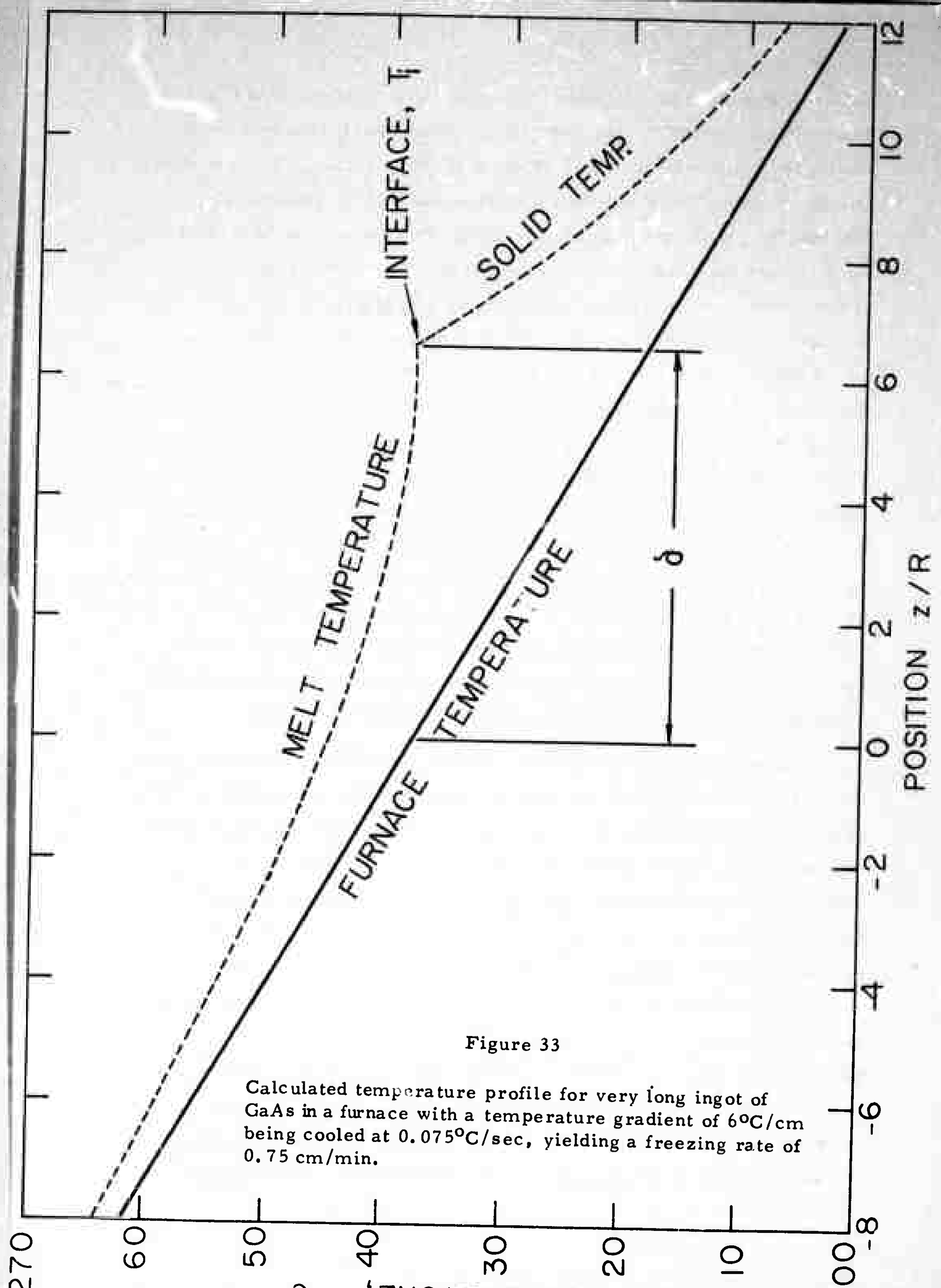

Figure 33

Calculated temperature profile for very long ingot of GaAs in a furnace with a temperature gradient of 6°C/cm being cooled at 0.075°C/sec, yielding a freezing rate of 0.75 cm/min.

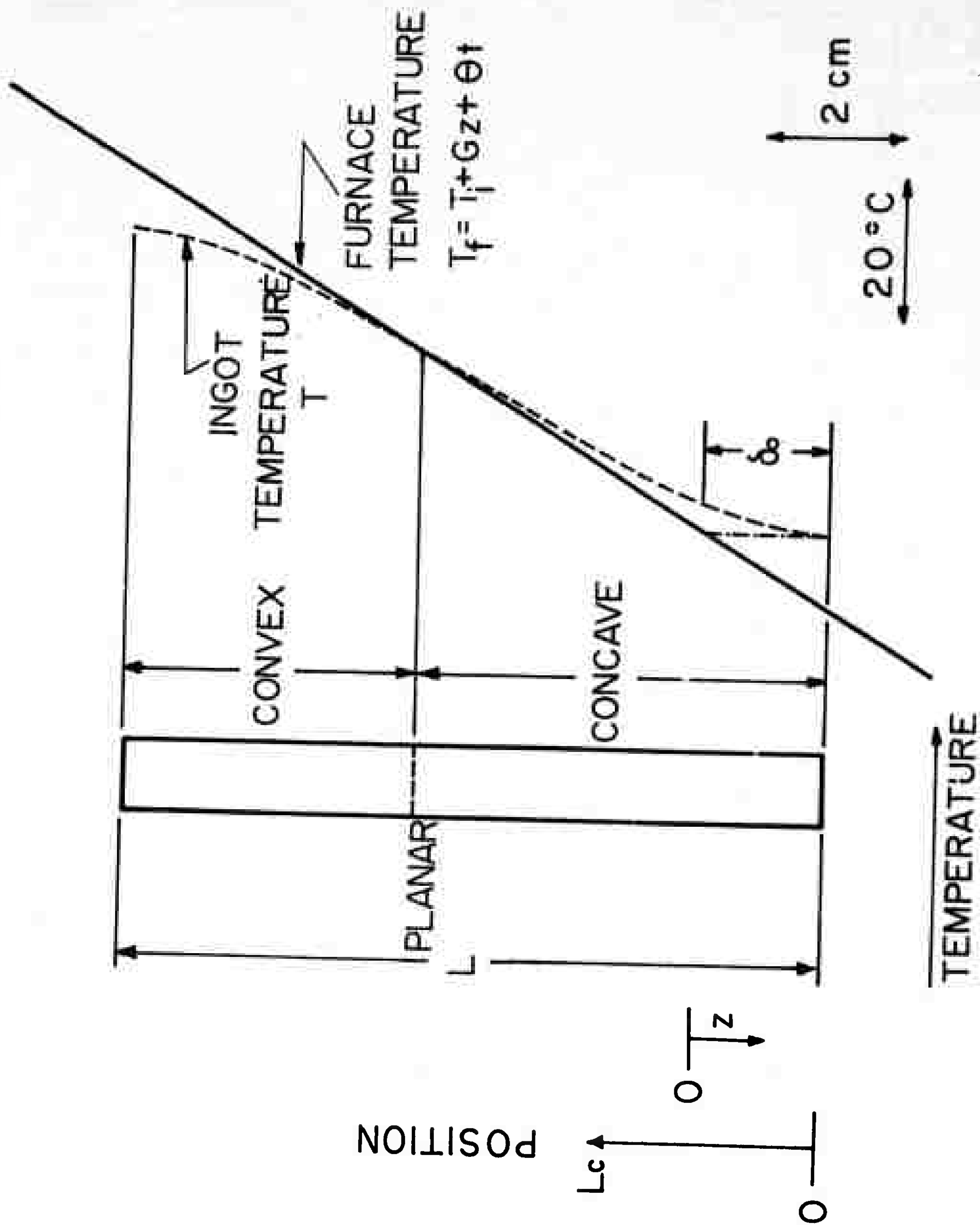

Figure 34 Heat transfer in gradient-freeze growth of GaAs in a finite ampoule.

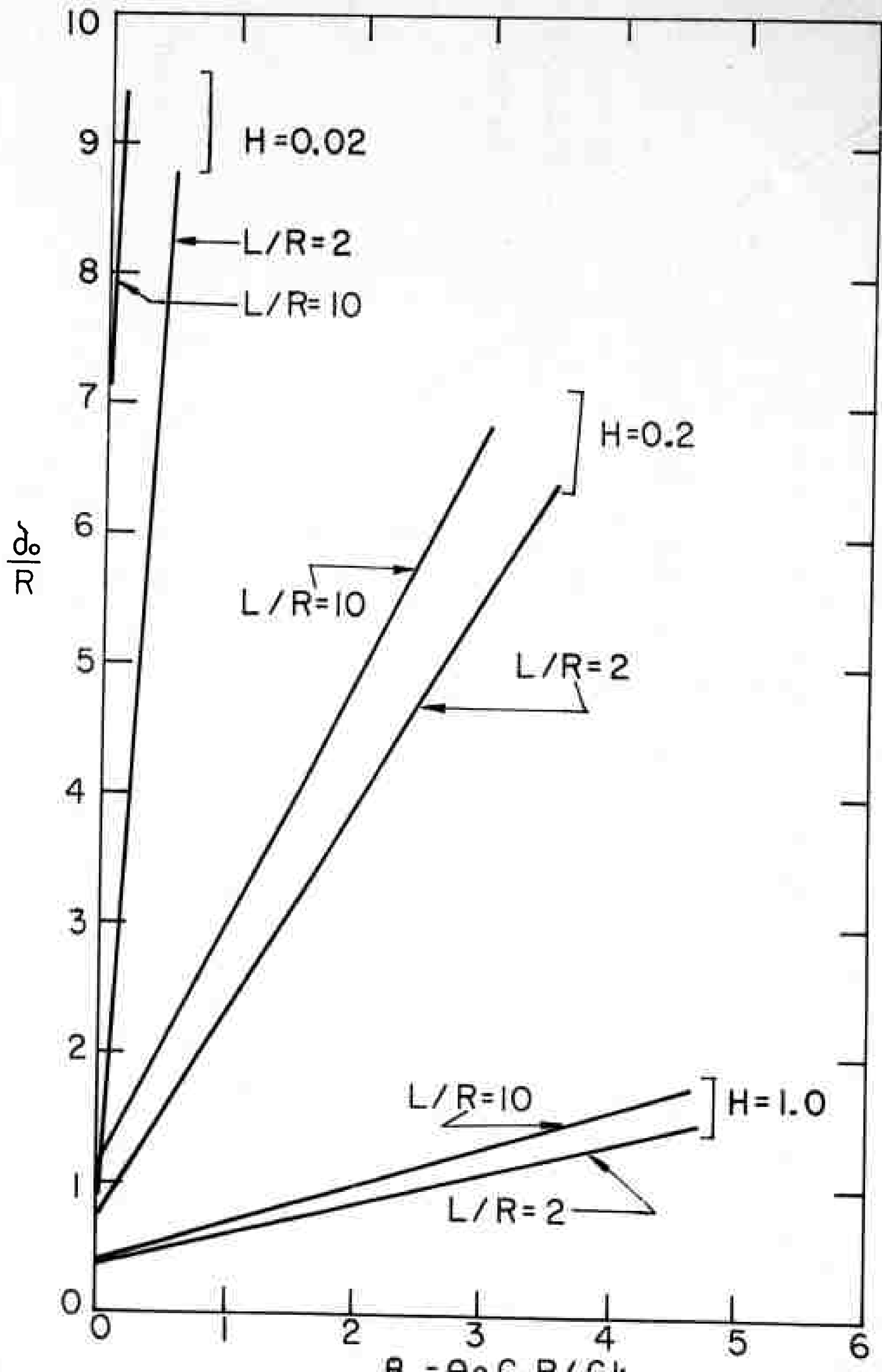

Figure 35 Heat transfer parameters dependence of δ_o, the initial displacement of the interface from the position in the furnace having the same temperature.

interface temperature and the adjacent furnace temperature as a function of the length of the GaAs crystal is shown in Figure 36, in which we took $\beta = 0.0048$, $H = 0.039$ and $L/R = 10$. A concave interface is predicted for the first 58% of the ingot and a convex interface for the last 42%, which corresponds nicely with our observation on the transition from polycrystalline to single crystal growth.

It was found that the interface shape may be controlled by application of additional cooling to the cold end of the ingot. For example, Figure 37 shows the prediction for GaAs when the end of the ingot loses heat to a sink held 78.5°C below the adjacent furnace temperature. In this case we predict the interface would start planar, turn slightly concave, and later become increasingly convex. Suitable conditions would yield a convex interface throughout.

II. STUDIES OF CRYSTAL GROWTH PHENOMENA

A. Incorporation of Solid Particles

Solid foreign particles are known to generate new grains and twins when they are incorporated into a solidifying crystal. This has, for example, been observed during growth of GaAs by our new Czochralski technique. Therefore, we have investigated the influence of stirring on particle incorporation during solidification (8). A horizontal zone melting technique was employed with rotation of the tube at various rates. Naphthalene with particles of carbon, copper and iron oxide was used as an analog for convenient study. The steady state zone shape varied with travel rate as shown in Figure 38. Under given conditions, particles were rejected below a critical freezing rate V_c and incorporated above that rate. To determine V_c the travel rate was slowly increased. The circulation and trapping behavior varied from particle to particle, apparently determined by particle size and density. Thus, at low rotation rates copper ($\rho = 8.9$) was trapped more readily at the center of the ingot than at the wall, as

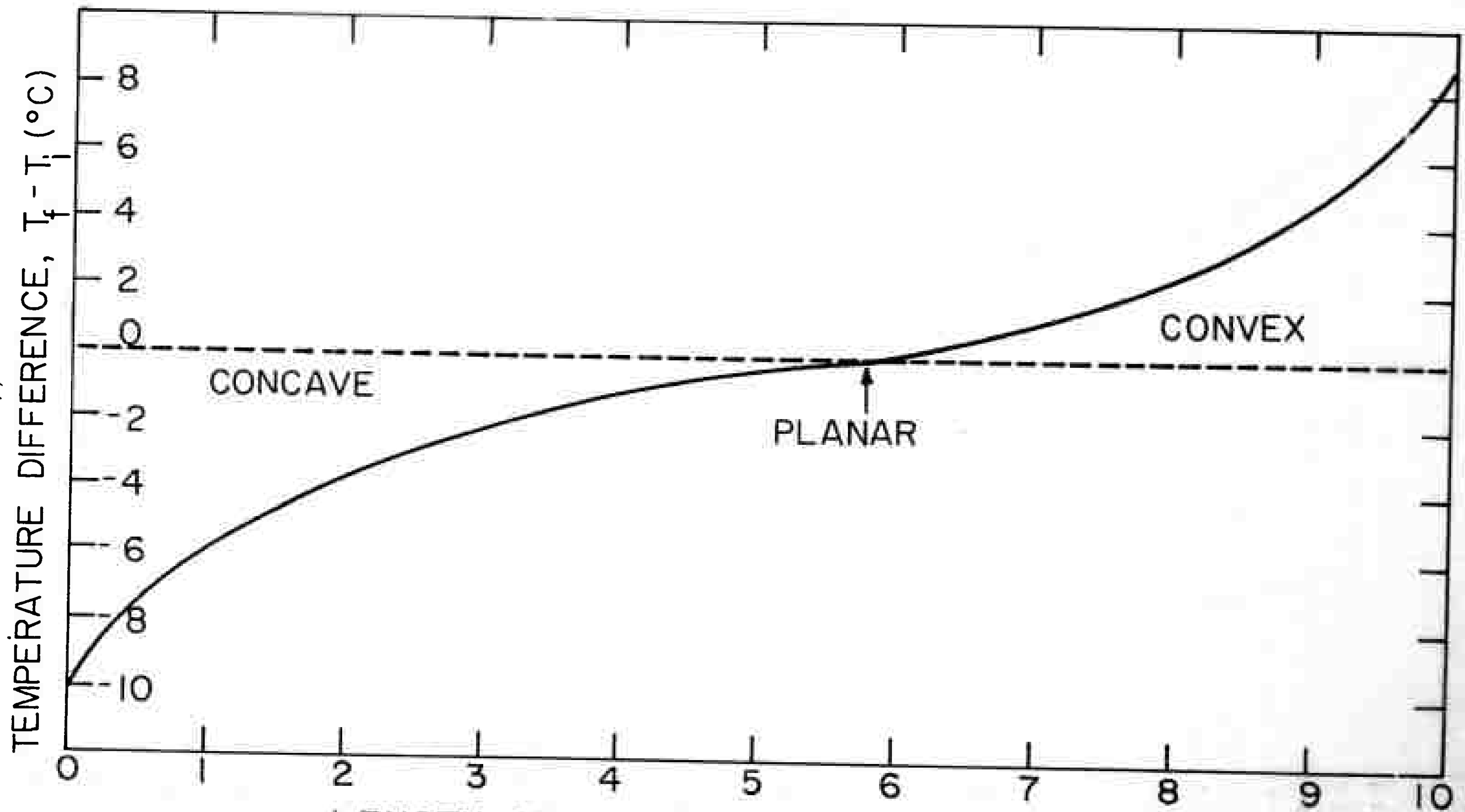

Figure 36 Difference between interface temperature (Gradient-freeze growth) and the adjacent furnace temperature for GaAs in gradient freeze growth.

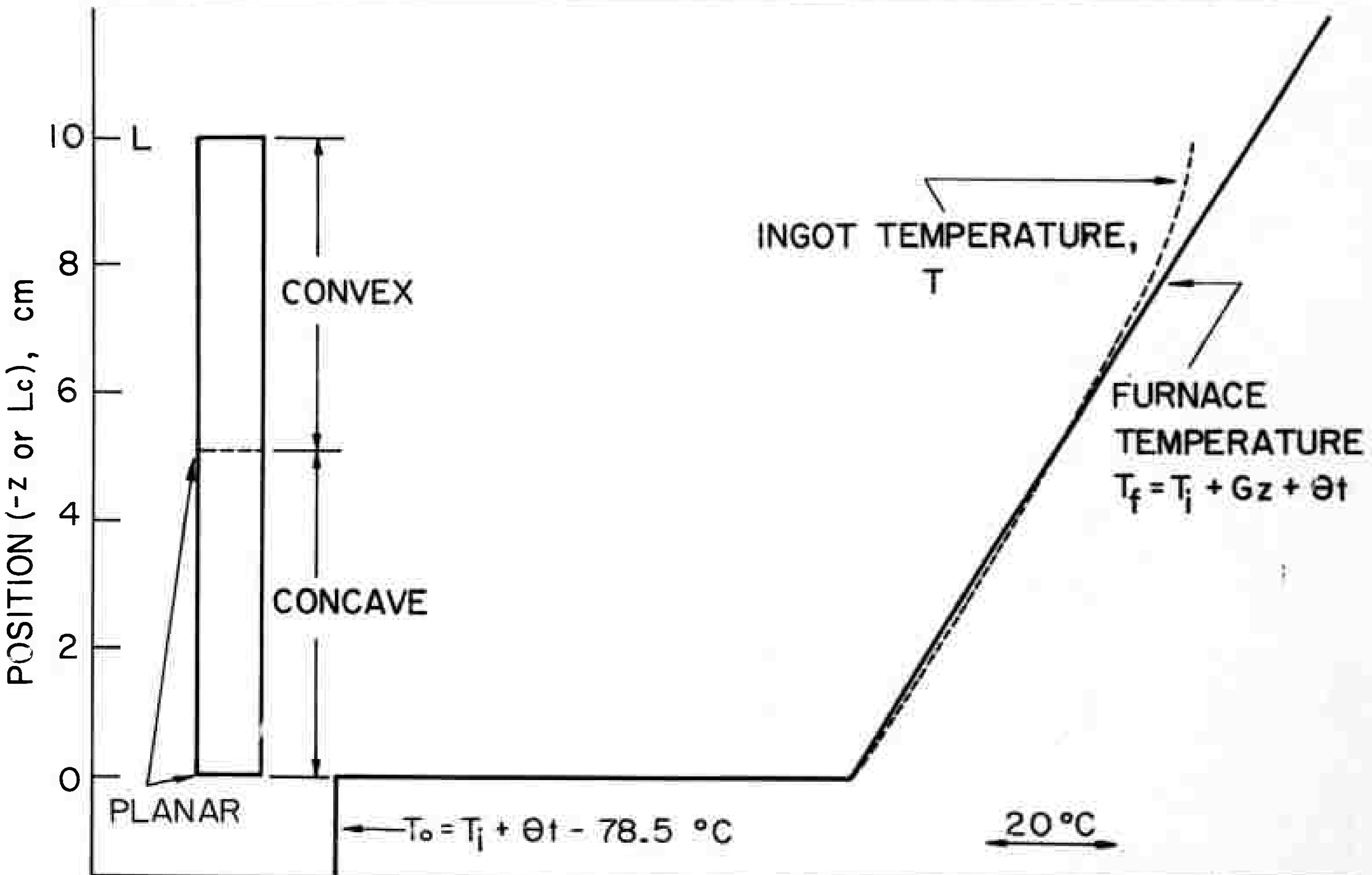

Figure 37 Predicted temperature profile for GaAs in gradient freeze growth with the cold end of the ampoule losing heat to a sink held 78.5°C below the adjacent furnace temperature.

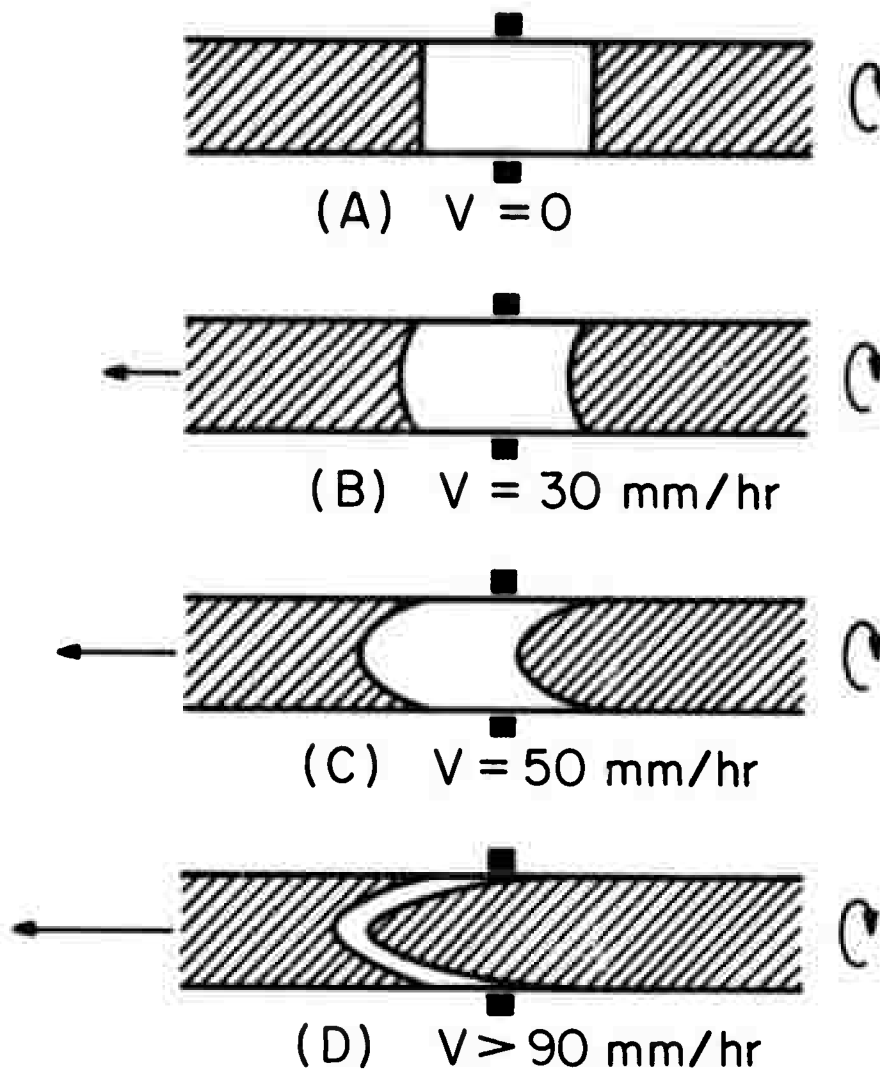

Figure 38 Change of zone shape with travel rate in horizontal zone melting of naphthalene with rotation.

shown in Figure 39. As the rotation rate increased, trapping became easier at the wall and more difficult in the center. The dependence on rotation was less for Fe_2O_3 particles ($\rho = 5.2$; Figure 40), and still less for carbon ($\rho \sim 2$; Figure 41). Thus, there was an optimal rotation rate for rejection of the particles. We expect a similar situation for Czochralski growth. The maximum critical freezing rate increased slightly as the tube diameter increased from 10 mm.

We have also found that programmed-rate solidification can be used to separate particles by type or by size. Thus, for example, a mixture of carbon and copper was quantitatively separated.

B. Boiling and Convection in Inclusions in a Temperature Gradient

When GaAs is grown from solution or from non-stoichiometric melts, Ga or As inclusions are sometimes formed in the crystal. Because of the dependence of solubility on temperature these inclusions should move in a temperature gradient imposed on the crystal during growth or later. We have briefly studied phenomena which occur when solvent inclusions are subjected to a temperature gradient [9, 10]. Alkali halide crystals containing water and water-alcohol inclusions were used as convenient analog systems for study. It was confirmed that solvent inclusions move toward the heat source under ordinary conditions. As noted previously [11], the presence of air bubbles caused the inclusions to move in the wrong direction. When the temperature was raised above the levels shown in Table VI boiling occurred in the inclusions. This at first caused rapid movement, but then the travel rate fell to near zero. The solvent vapor pressures corresponding to these boiling points far exceed 1 atmosphere. Experimentally measured travel rates are summarized in Figure 42, 43 and 44. The dashed curves correspond to theoretical movement rates with water as a solvent, no air bubbles or boiling present, no convection in the inclusion, and infinite interface kinetics. We conclude from this data that there is an appreciable

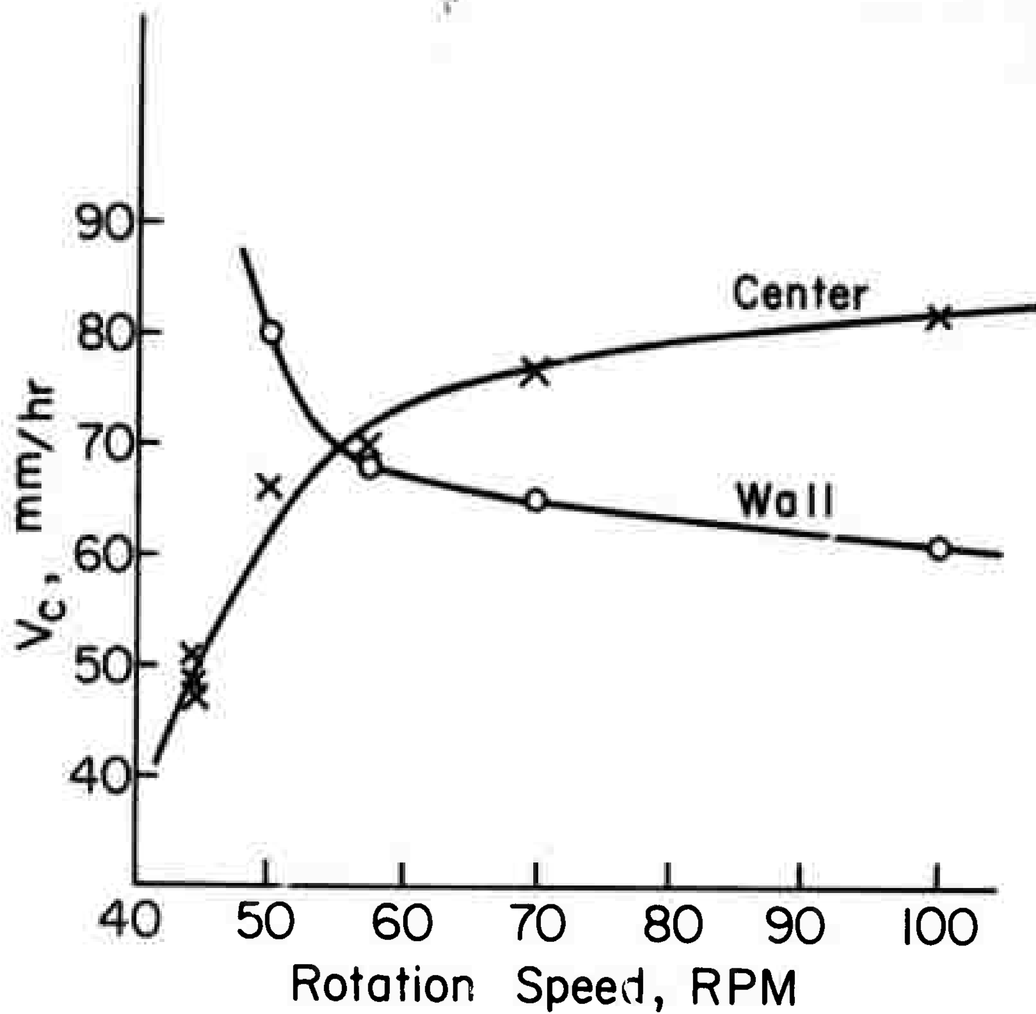

Figure 39 The influence of tube rotation on incorporation of copper particles by naphthalene during horizontal zone melting.

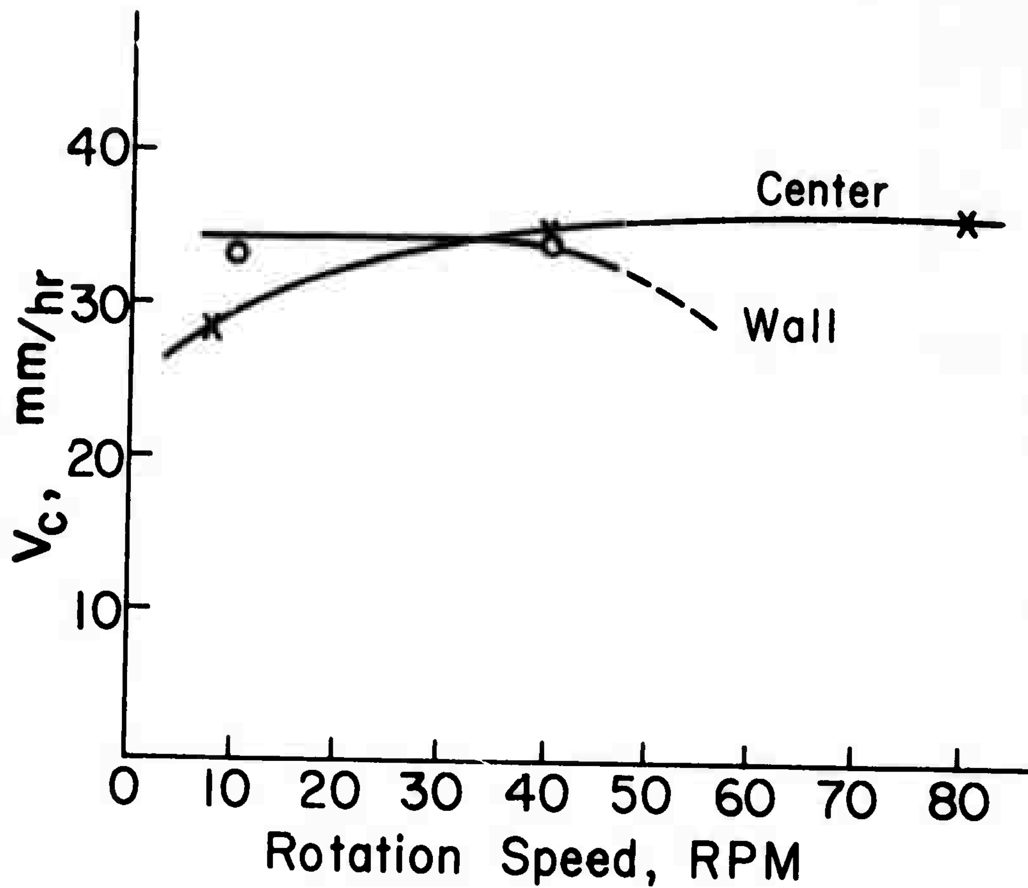

Figure 40 The influence of tube rotation on incorporation of iron oxide particles by naphthalene during horizontal zone melting.

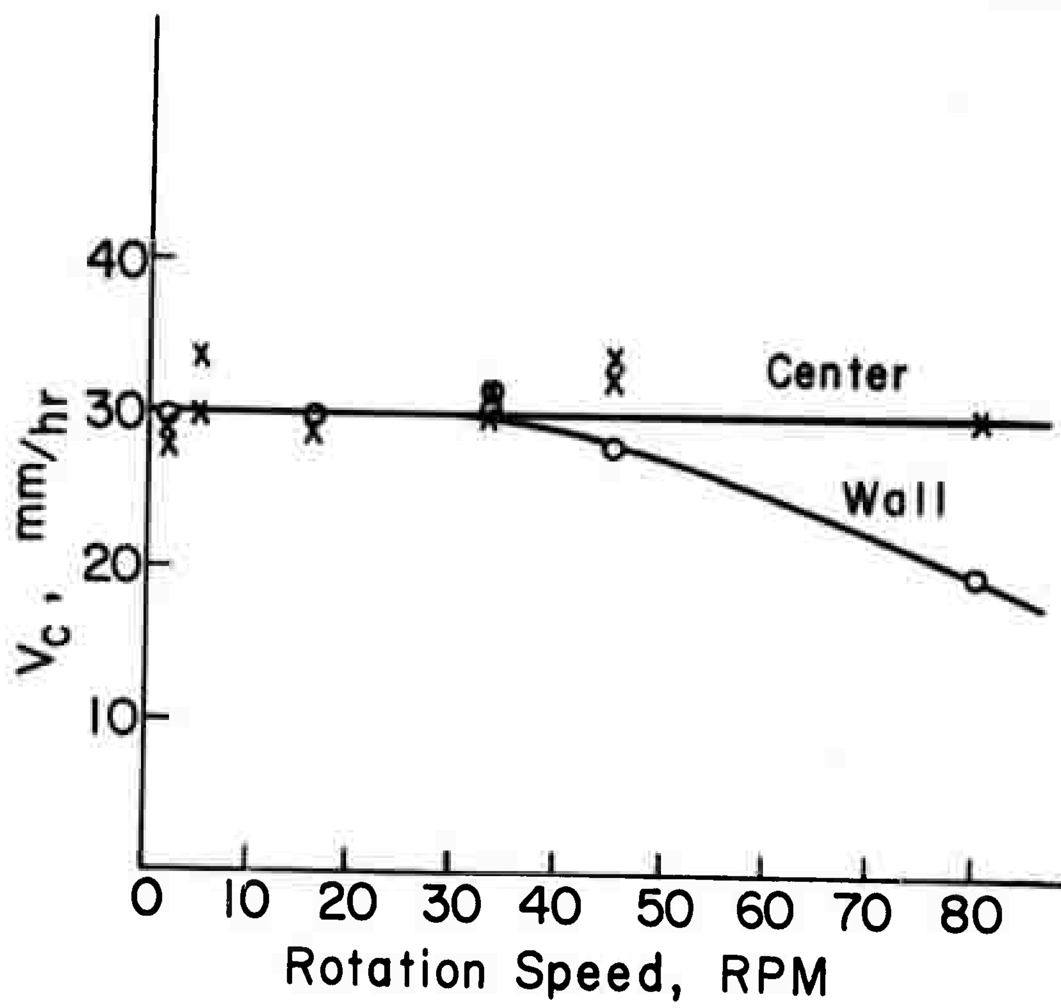

Figure 41 The influence of tube rotation on incorporation of carbon particles by naphthalene during horizontal zone melting.

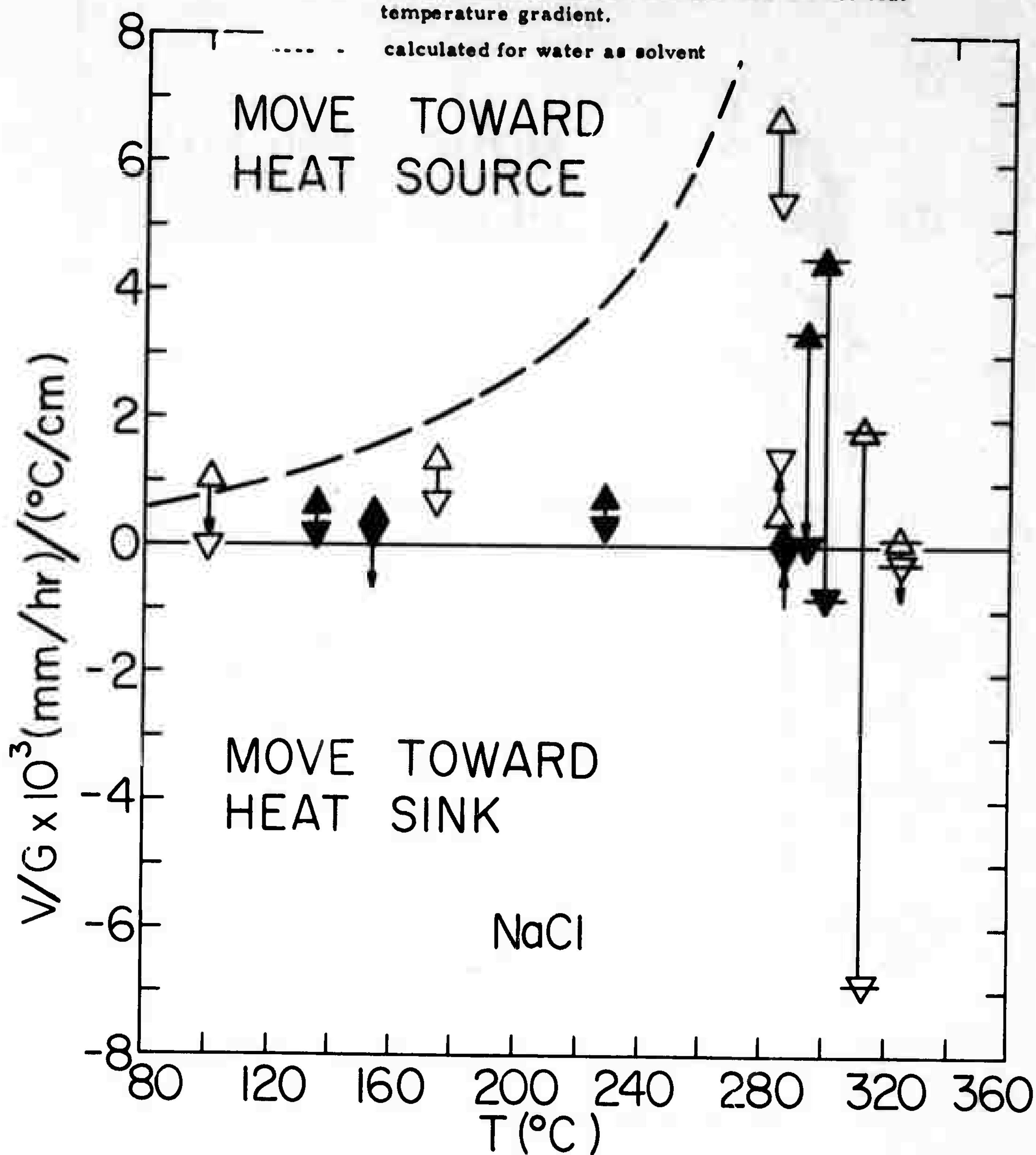

Figure 42 Rate of movement of solvent inclusions in NaCl/imposed temperature gradient. T is average temperature within inclusion.

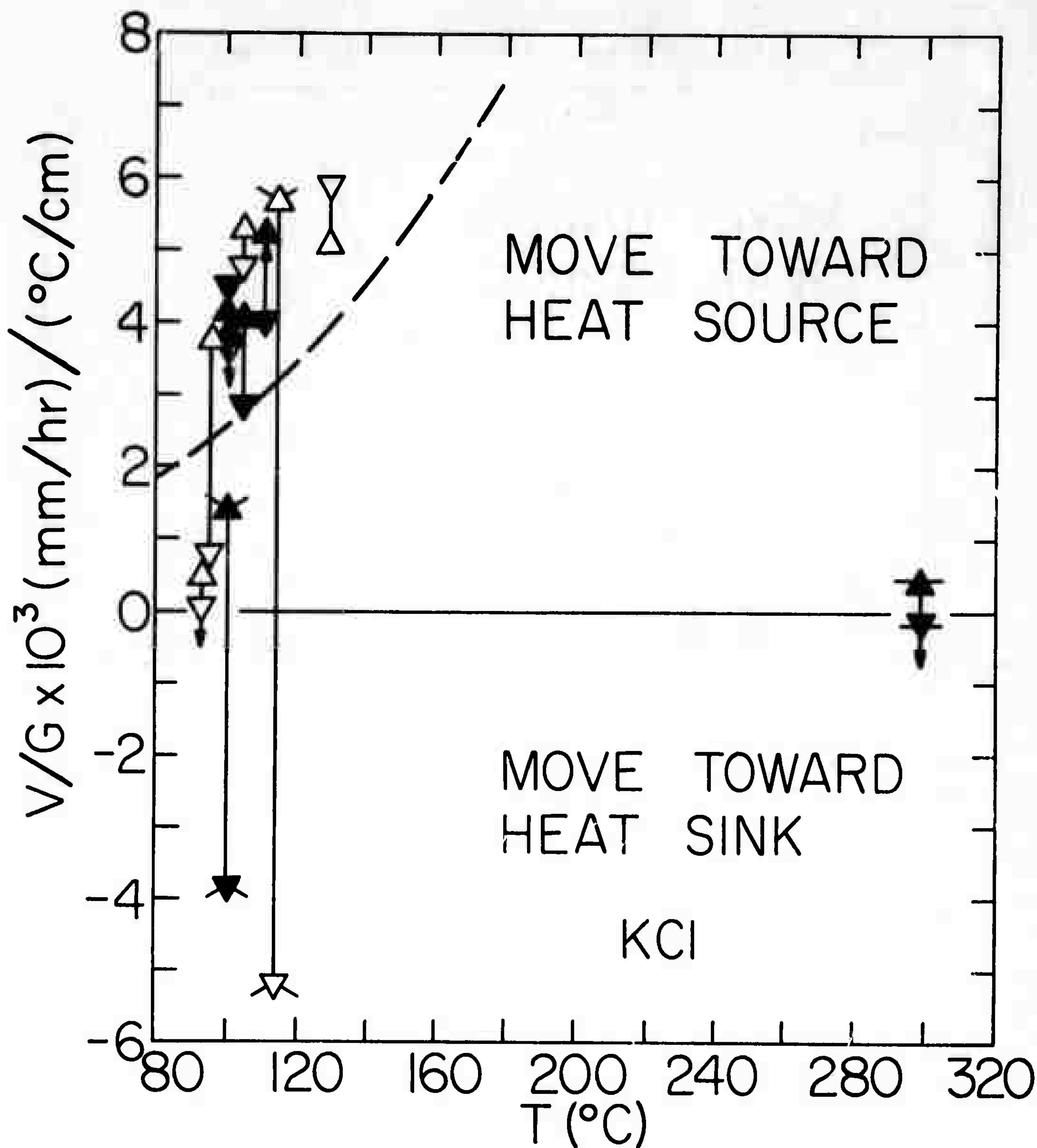

Figure 43 Rate of movement of solvent inclusions in KCl/imposed temperature gradient. Same notation as Fig. 42, plus following: Ⴤ - air bubble present in inclusion.

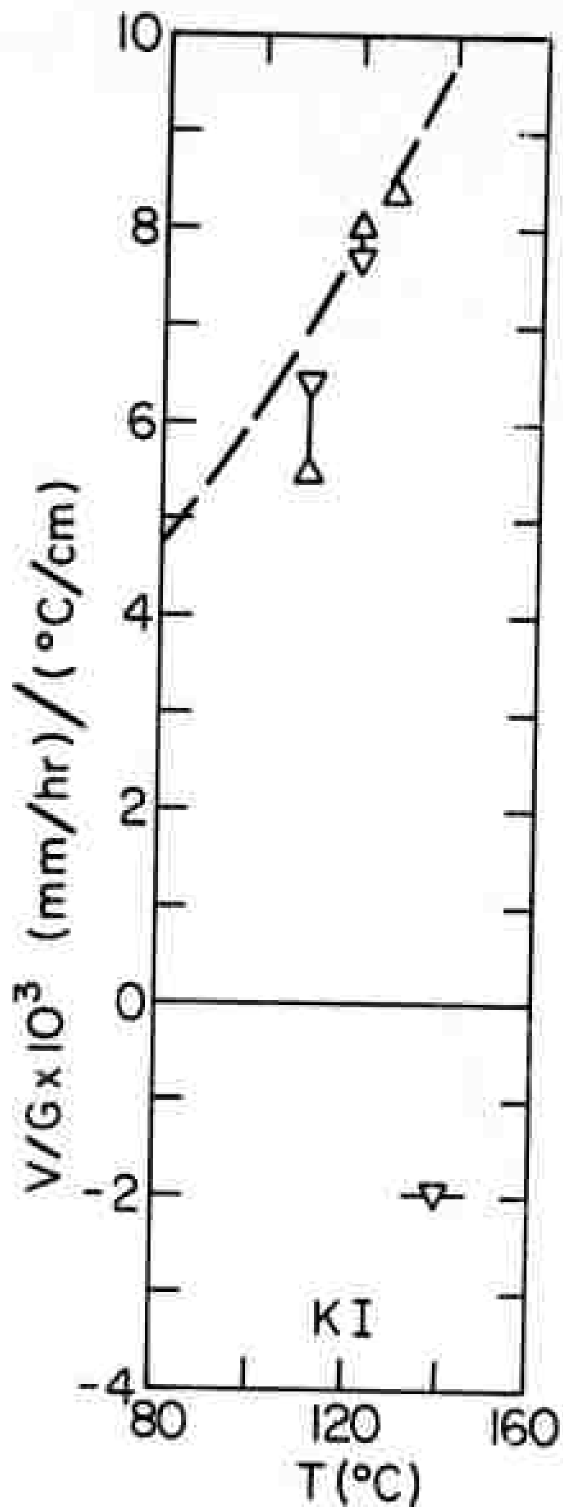

Figure 44 Rate of movement of aqueous inclusions in KI/imposed temperature gradient.

Same notation as Fig. 42.

TABLE VI

Measured Boiling Points of Solvent Inclusions in Alkali Halide Crystals in a Temperature Gradient

Crystal	Solvent	Boiling Point
NaCl	water	321°C
NaCl	water-alcohol	296°C
KCl	water	249°C
KCl	water-alcohol	209°C
KI	water	137°C

interfacial kinetics resistance to movement and that free convection was taking place in these ~ 0.5 mm diameter cylindrical inclusions, resulting in greater movement rates with a horizontal temperature gradient than with a vertical gradient.

C. Other Crystallization Studies

A paper has been published on off-eutectic solidification, which would prove useful were oriented composites of, say, GaAs-As required [12]. A survey of motion pictures dealing with crystal growth was also published [13].

III. OXYGEN: MEASUREMENT AND CONTROL IN LIQUID EPITAXIAL GROWTH OF III-V SEMICONDUCTORS

As reported previously [1], we are developing techniques to permit lower temperature growth of GaAs. The rates of oxygen removal from GaAs liquid phase epitaxial systems are dominant features which ultimately limit the minimum growth temperatures. Low growth temperatures are

desirable in that the temperature control requirements for controlling film thicknesses are less, impurity solubilities are lower, and chemical reactivities are reduced.

The oxygen problem has two principal aspects. The first is oxygen chemiabsorbed on the seed, most likely as a GaAs-oxide more stable than Ga_2O_3(s). In order to grow superior quality films it is necessary to remove this oxide prior to the growth. Manifestations of incomplete removal are irregular nucleation and the growth of films with poor surfaces.

Evidence for the presence of oxygen on the surface of GaAs substrates which were not reduced by H_2 in 30 minutes at 825°C was previously noted. The mole ratio of H_2O to H_2 in the exhaust gas line of a liquid phase epitaxial system was monitored by the emf of a ZrO_2-CaO cell operated at 700°K. The emf of this cell was stable to 1 mV and changed approximately 20 mV per decade change in the H_2O-H_2 mole ratio over its linear range. This was estimated to be the case for H_2O/H_2 ratios $\leq 10^{-6}$. For the reaction at 800°C the steady-state H_2O/H_2 ratio was $\sim 2 \times 10^{-6}$ with a H_2 flow rate of 100 cc/min. Without changing the flow conditions the emf of the ZrO_2 cell increased, indicating a lower H_2O/H_2 ratio when the reaction was cooled. This indicated that the reactor inlet H_2 was of higher quality and that it was degraded by the quartz reaction itself at 800°C. With the reaction at 800°C for several hours so that steady state conditions pertained, the seed was lowered into the furnace to a position just above the melt and so maintained for 30 minutes. At the end of this period the H_2O/H_2 ratio was at its original steady state value. Immersion of the seed in the Ga melt caused a momentary rise in H_2O/H_2 ratio. The Ga melt was slightly under-saturated. This rise indicated that the oxide on the substrate dissolved in the melt and the dissolved oxygen then reacted with the H_2 atmosphere to produce H_2O. Removal of the seed from the melt and subsequent immersion produced no detectable change in the exit H_2O/H_2 ratio. These experiences prompted the consideration of using an alternate method for removing oxygen from Ga melts.

One approach used in several laboratories elsewhere involves the use of carbon reactors contained in quartz. There are problems associated with adequately cleaning the carbon, avoiding reaction of carbon with the quartz and subsequent introduction of Si as an impurity. In principle, though, the carbon should be a good reducing agent for oxygen in Ga. H_2 is almost as good a reducing agent. The rates of removal are important. If one considers the dissolved oxygen in the Ga melt to be in equilibrium with the H_2 atmosphere (an optomistic assumption) and that the dissolved oxygen removal rate is proportional to the partial pressure of H_2O (which we optomistically take as 10 ppm or 10^{-5} atm) and a reasonable H_2 flow rate of 100 cc atm min^{-1}, the removal rate of oxygen from the melt at 1000°K is

$$\text{moles of 0 removed from melt per minute} = \frac{10^{-5}\text{ atm} \times 100\text{ cc/min}}{1000\text{ deg} \times 82\text{ cc atm mol}^{-1}\text{deg}^{-1}} \simeq 10^{-8}\text{mol/min}$$

$$\simeq 1\text{ monolayer/cm}^2\text{ of substrate.}$$

This slow removal rate caused us to consider using electrolytic pumping to remove dissolved oxygen. Calcia-stabilized zirconia operating with an ion current of only 10 mA can remove oxygen at a rate of 3×10^{-6} moles/min or 300 times faster than a clean H_2 atmosphere (work elsewhere has shown near unity transference numbers for oxygen ion). In addition, this pumping efficiency is to be anticipated for concentrations of oxygen below the saturation concentration at temperatures as low as 500°C.

The system designed to test this is shown in Figure 45. Its prime feature was the use of a calcia-stabilized zirconia pump which served as the melt crucible. The other electrode (outside) was fired Pt paste operating in a H_2 atmosphere saturated with H_2O at 0°C to establish a known oxygen activity. A well-designed Pd-Ag tube H_2 diffuser was graciously provided by Standard Telecommunications Laboratory. All valves were the improved West Glass stopcocks with leak rates

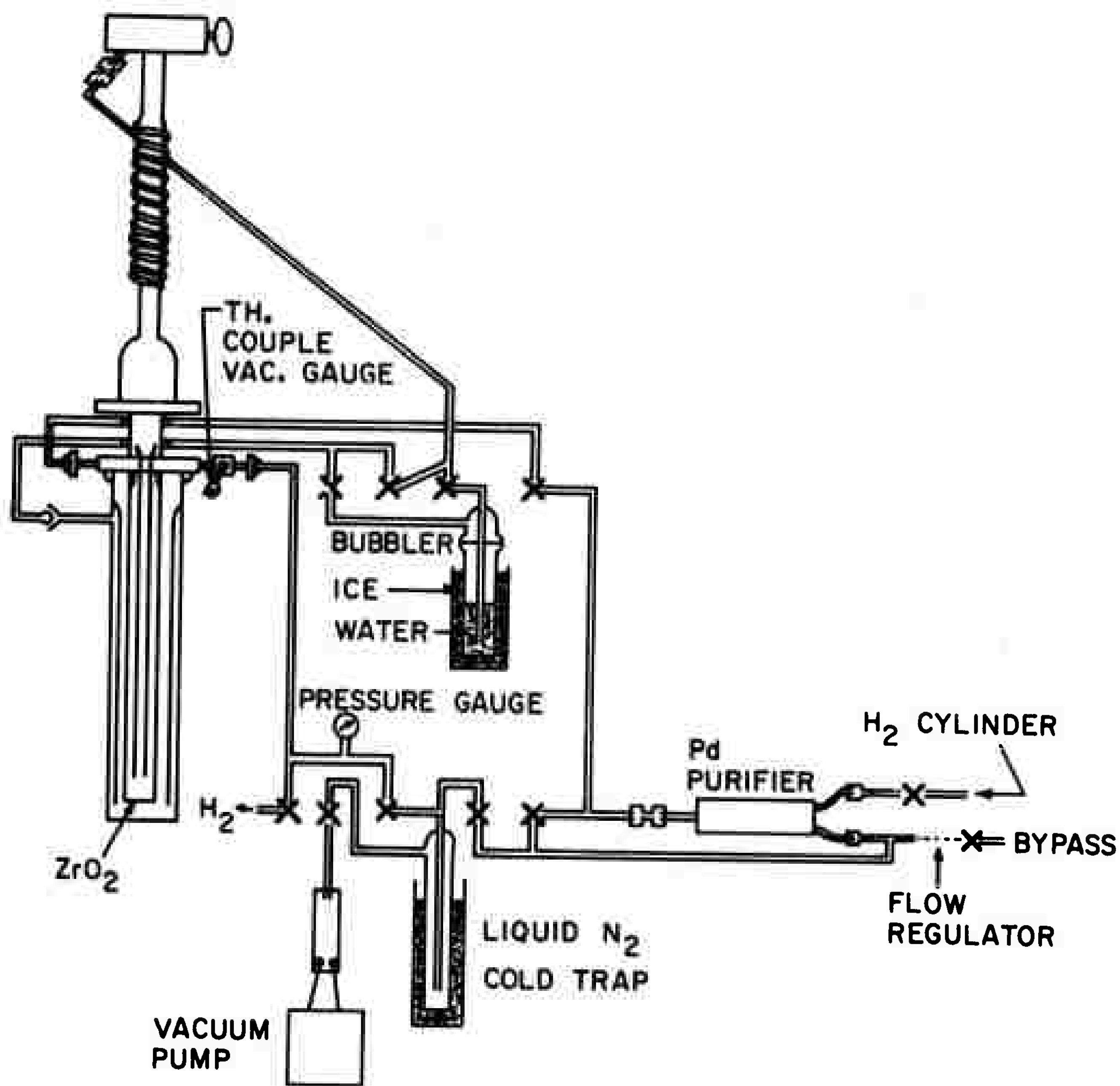

Figure 45 Diagram of system for measuring and controlling oxygen concentrations.

$\leq 4 \times 10^{-10}$ ssc atm sec^{-1}. Initially, problems were encountered with leaks, necessitating some modifications, which also permitted electrochemical measurement of oxygen fugacity in the cell. In this manner we have achieved and measured oxygen fugacities in Ga melts over five orders of magnitude below those which we could achieve by hydrogen reduction at 700°C.

These techniques will have numerous applications in addition to permitting liquid epitaxial growth of GaAs at lower temperatures. They will permit growth of GaAs with a controlled and measured oxygen fugacity. The electroluminescence efficiency in red-emitting GaP diodes is greatly reduced by the presence of oxygen. These techniques should permit growth of GaP with much lower oxygen concentrations than is currently possible. The role of oxygen in determining the properties of GaAs is largely unknown, primarily because reliable analytical techniques were not previously available. In order to be able to measure oxygen concentrations, we will determine the oxygen fugacity-concentration relationships for Ga and several other metallic solvents.

A horizontal solution growth epitaxial system has been designed for the growth of semiconductor films. Its design incorporates a novel feature which provides for the automatic control of oxygen fugacities in the films. Advantages are that large sized zirconia or thoria tubes will not be required. Use of these can be expected to be troublesome because of the poorly controlled purities of the commercial tubes and the difficulties in fabricating them.

A novel boat design has been developed for the growth of GaAs bulk crystals and those of other III-V semiconductors. It utilizes a semipermiable membrane which should restrict melt contamination by impurities such as silicon and oxygen.

IV. CHARACTERIZATION

A. Carbon in GaAs

We have performed infrared absorption measurements on some of our high resistivity Czochralski crystals over a higher frequency region. Figure 46 shows the liquid nitrogen temperature absorption coefficient vs. wavenumber for an undoped sample. Note the distinct absorption band at $\sim 582.4\ cm^{-1}$. This band is due to the localized vibrational modes of carbon in GaAs [14]. The rise of the absorption coefficient at the lower frequencies is due to the two-phonon lattice absorption band at 528 cm^{-1}. Differential transmission measurements performed on this sample and an undoped horizontal Bridgman sample over a frequency range from 5000 cm^{-1} to 350 cm^{-1} showed no additional bands. This indicates that carbon existed in GaAs as a single defect species and that there was no complexes or pairing between carbon and other impurities in the material. At present, the exact role of carbon in the electrical properties of our GaAs is not known. It is suspected, however, that carbon may be the impurity that lowers the mobility (see Section I.A).

Additional measurements are being carried out to study the properties of carbon in GaAs. Crystals doped heavily with n-type and p-type impurities will be grown and infrared measurements will be made to see if there is any enhancement or suppression of the carbon local mode. Attempts will be made to identify whether carbon is a donor or an acceptor in GaAs, and to correlate the absorption peak strengths with the concentrations of the carbon impurities.

B. Dislocation Studies and Electrical Properties of GaAs

The purpose of this section is to demonstrate the results of a unified approach to the characterization of semiconductor materials by applying various analytical techniques to the same set of samples. In our previous report [1] we have shown, using optical microscopy, various

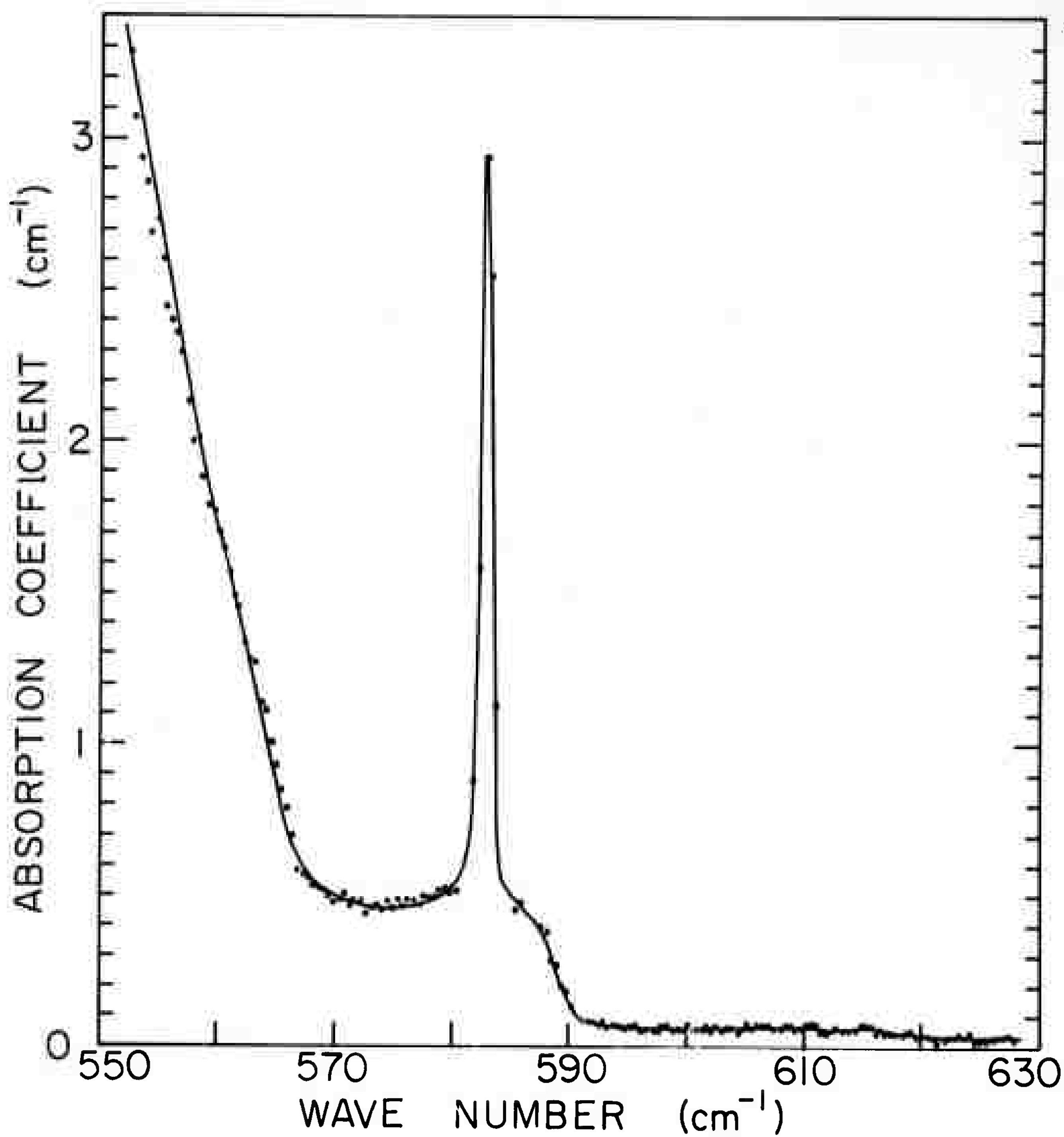

Figure 46 Infrared absorption at liquid nitrogen temperature of sample from Czochralski-grown crystal CZ-37.

etching techniques needed to correctly portray dislocations on the polar (111) surfaces of GaAs. In this report we will show, by means of transmission x-ray topographs, bulk growth defects in a crystal grown by our new liquid seal Czochralski method. Electron beam excited cathodoluminescence was used to study the surfaces of both the as-grown as well as the plastically deformed crystal. Finally, the Hall parameters of the as-grown and deformed crystals were measured as a function of temperature, type of dislocation and dislocation density. [15]

1. X-Ray Topography

To characterize defects due to crystal growth, sample slices for x-ray topography were cut normal to the growth direction from the top (seed) and bottom end of Czochralski crystal CZ-16, from which bend samples were also prepared. In order to obtain topographs of the bulk defects, thin wafers (0.076 to 0.152 mm) of (111) GaAs had to be prepared by mechanical and chemical polishing methods.

The following steps were followed in the preparation of the GaAs wafers:

(a) The crystal was mounted on a sample holder that could be used with the Laue camera and the cut-off wheel.

(b) The crystal was oriented to the desired crystallographic direction (e.g., < 111 >) to within 0.5 to 1.0^{o} using standard Laue back reflection methods.

(c) The desired number of 1.0-mm thick slices was cut from the crystal by mounting both crystal and holder on the platform of a diamond (or SiC) cut-off wheel.

(d) Using a low melting temperature wax (Apiezon black wax) the slices were mounted on a flat quartz disk or on a stainless steel cylindrical block. The slices were then hand lapped on plate glass in a slurry of 3200 mesh abrasive powder.

(e) To remove surface damage due to lapping, a method of simultaneous mechanical and chemical polishing was employed. The sample was polished on a rotating wheel covered with a soft cloth (Geoscience Polytex Pix) continuously wet with a polishing solution of "Mirrolite" powder (a patented powder developed at USC). The surface removal rate was 0.0025 to 0.025 mm/hour.

(f) Because of the polarity of GaAs in the $< 111 >$ direction, a solution of Mirrolite A was used on the A(111) surface, and plain Mirrolite for the $B(\bar{1}\,\bar{1}\,\bar{1})$ surface. To determine the polarity of the (111) surface to be polished, the Schell etchant method described in detail in the previous report [1] was followed. Mirrolite A was used instead of the conventional bromine-methanol solution because of the toxic nature of the bromine gas evolved.

(g) After polishing both surfaces to the desired thickness, the GaAs wafer (extremely brittle) was very carefully demounted from the holder by immersing the sample in acetone for three to six hours. After successively rinsing in acetone and deionized water, the wafer was dried in a slow jet of filtered air.

Lang $(\bar{2}20)$ symmetric transmission topographs of (111) GaAs wafers were taken with a Kystallos Lang camera and recorded on 50 micron Ilford nuclear plates. Figure 47 shows $(\bar{2}20)$ topographs of slices taken from the front (Figure 47a) and back end (Figure 47b) of the crystal. Although a low dislocation density ($\sim 10^3$ cm^{-2}) has been determined for this crystal, some features indicated by arrows may be associated with dislocations.

Figure 48 shows $(\bar{2}20)$ transmission topographs of (111) wafers taken from the back end of the crystal. Striations in Figure 48a may be associated with dislocations, while the network may be due to compositional

<112>

<110>

a

Reproduced from best available copy.

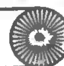

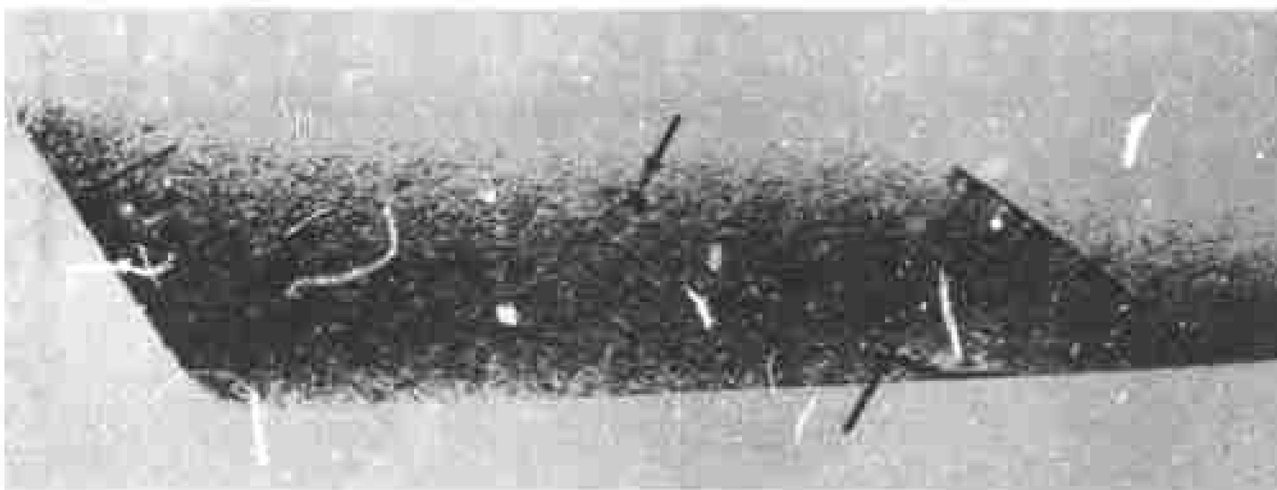

b

Figure 47 Lang $(\bar{2}20)$ symmetric transmission topographs of (111) wafers of as-grown, Te-doped ($10^{17}cm^{-3}$) GaAs. Arrows refer to features associated with dislocations in (a) wafer taken from front (or seed) end, and in (b) wafer taken from back end of crystal. Crystal directions refer to both samples. Magnification: 15x. Sample nos. (a) CZ-16-13, (b) CZ-16-4.

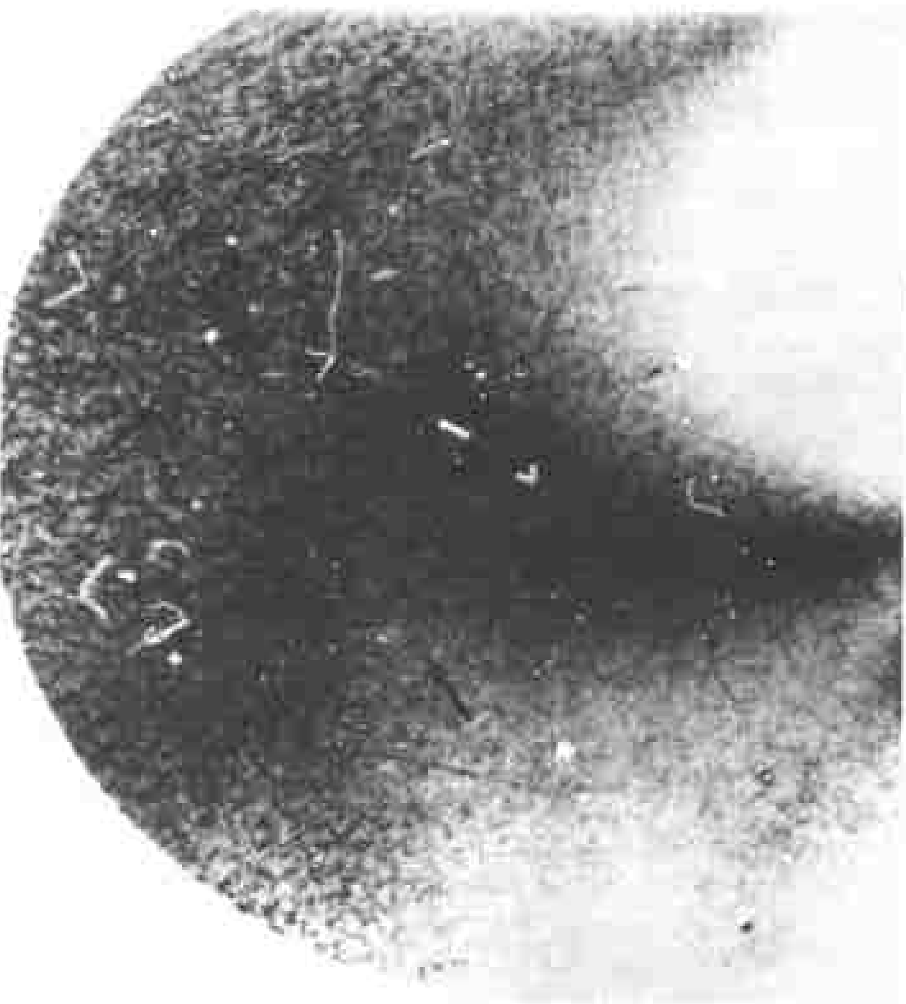

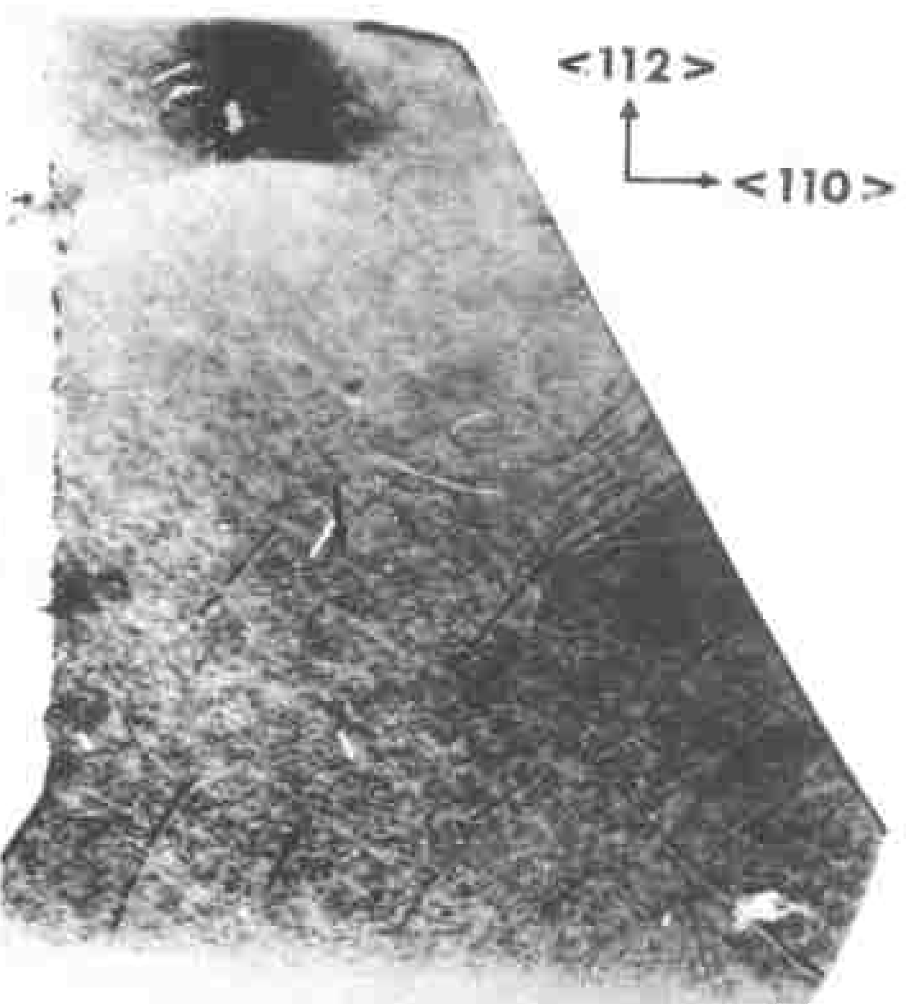

Reproduced from best available copy.

Figure 48 Lang ($\bar{2}20$) transmission topographs of (111) wafers taken from back end of as-grown Te-doped (10^{17} cm^{-3}) GaAs. Arrows indicate possible dislocations in (a) and (b). Crystal directions refer to both samples. Magnification: (a) 12x, (b) 15x. Samples nos. (a) CZ-16-3; (b) CZ-16-2.

fluctuations or polishing artifacts. To identify these features more precisely, we plan to take other topographs of the same samples using skew transmission and skew reflection (Berg-Barrett) techniques.

2. Plastic Deformation by Four-Point Bending

To determine the effects of crystal imperfections on the electrical properties of GaAs, dislocations were introduced in a controlled manner into the samples by four-point bending in an all quartz bend-furnace.

GaAs samples chosen for the bending experiments were taken from a Te-doped (10^{17} cm^{-3}) Czochralski crystal (CZ-16) and an undoped crystal grown by the horizontal Bridgman method (HB-105). After suitably orienting the crystals by a standard Laue X-Ray technique, the samples were cut successively with a diamond wheel and a diamond impregnated wire saw such that the bars could be bent along the [$\bar{1}\bar{1}2$] direction (Figure 49).

The samples were 1.6 to 2.0 cm long, 0.12 to 0.17 cm wide and 0.10 to 0.15 cm thick. To remove any surface damage due to cutting, the rectangular bars were lapped in a slurry of 3200 mesh powder, etched in a hydrofluoric-nitric acid solution (HF: NHO_3: H_2O = 1: 3: 2) until about 50 microns were removed, and finally rinsed in deionized water. The resulting samples exhibited bright and shiny surfaces.

Six bar samples were cut from two adjacent slices (nos. 9 and 10) from approximately the center of crystal CZ-16. Two bars taken from slice 9 were used for control purposes (namely, as-grown and heated, not bent), while from slice 10, four bars were cut and bent to various curvatures. To introduce a majority of α-dislocations (namely, dislocations whose extra half-plane ends on a row of Ga-atoms), the samples were bent according to the orientation shown in Figure 49, with [$\bar{1}\bar{1}2$] as the bend axis. To introduce β-dislocations (whose extra half planes end on As-atoms), the sample was flipped about the [$5\bar{1}2$] direction such that the bend axis was parallel to the [$11\bar{2}$] direction.

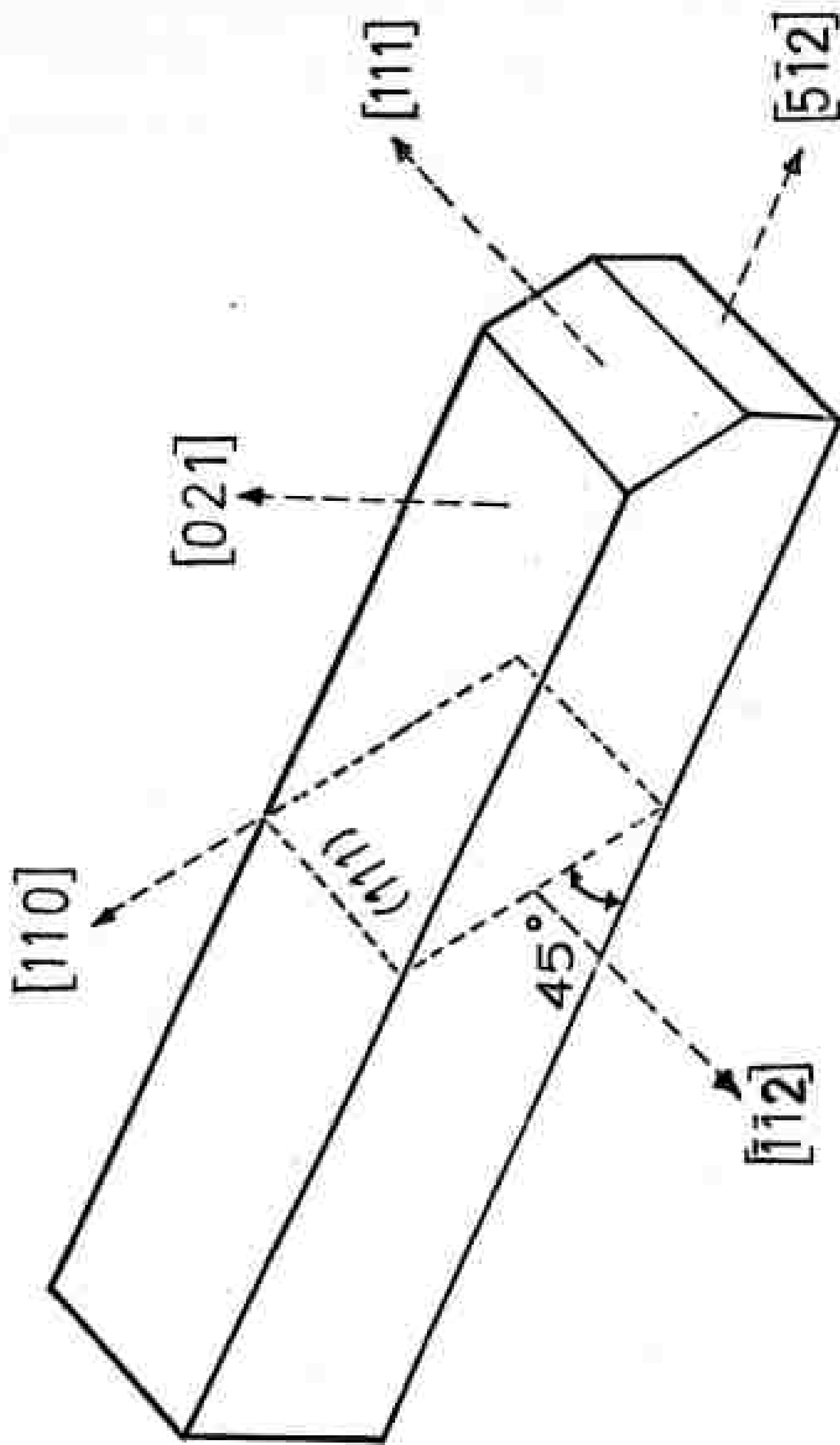

Figure 49 Orientation of GaAs bend sample showing $[\bar{1}\bar{1}2]$ bend axis and (111) slip plane.

Because the slices from the front end of the Bridgman crystal were slightly smaller than the Czochralski slices, only three bars (one for bending, the other two for control) could be cut from each slice. Thus, the four Bridgman samples were taken from four adjacent slices instead of from a single slice. To insure cleanliness of the samples, both the control and bend samples were etched lightly immediately prior to bending the the $HF-HNO_3$ solution and rinsed in deionized water.

The bending experiments were performed in an all fused silica apparatus (Figure 50) which was designed to eliminate sources of contamination likely to be present in a metallic or non-silica system. The bending apparatus consisted of a lower set of silica knife edges with a separation distance of $d_s = 1.24$ cm mounted on a movable stage (to permit easier alignment) and an upper set of knife edges ($d_s = 0.275$ cm) attached to the tip of a 1.5 cm diameter silica rod. The sample was set on the lower knife edges and kept in position by the upper knife edge. Bending was accomplished by turning the micrometer head a predetermined number of turns.

Prior to each bending operation, the silica platforms were removed from the bottle by means of the arch-shaped handles and washed with aqua regia, dilute HF, and rinsed in deionized water. To remove any residue from the cleaning, the entire bend apparatus was heated (minus the sample) to 700°C with two semi-cylindrical heating elements which surround the silica bottle. Upon cooling, the platforms were again removed from the bottle and a sample positioned on top of the lower knife edges. For control purposes, another unbent sample was set beside the lower knife edges on the movable stage. After flushing the silica bottle for 15 minutes with purified argon, the furnace was heated to 700°C. Temperature was monitored by a previously calibrated chromel-alumel thermocouple which extended via a sealed silica tube to the inside of the bottle down to the sample level.

The bending temperature range of 650 to 725°C was reached 15

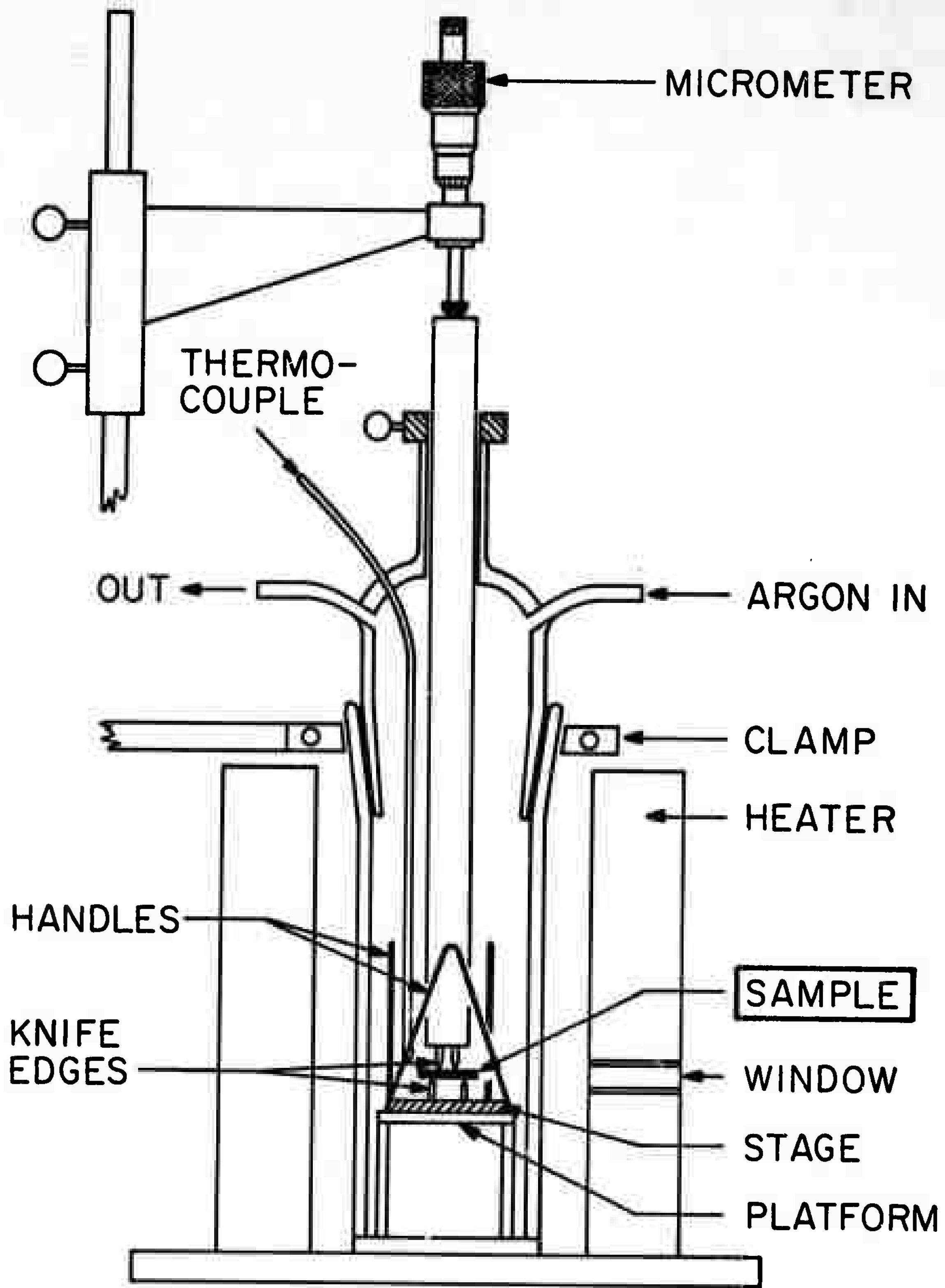

Figure 50 All-quartz four-point bend apparatus and furnace.

minutes from the moment power was turned on. The actual bending of the sample took 30 seconds. Immediately after bending, which was observed and monitored through a window, power was turned off and the sample cooled to room temperature by pulling the two heating elements away from the silica bottle. Upon removal from the furnace, the bent and control samples were always found to retain their original shiny surfaces.

Using this bending procedure, both α and β dislocations were introduced into the Czochralski and Bridgman grown GaAs samples. By bending these samples to various radii of curvature, R, which were measured graphically from enlarged photographs of the samples, different levels of dislocation densities were attained. The dislocation density, ρ, was calculated using Nye's relation [16], $\rho = 1/(Rb \cos \theta)$, where b is the magnitude of the slip vector, $\vec{b} = (a/2) < 110 >$, θ is the angle between the (111) slip planes and the neutral bend plane. Table VII lists the measured bend radii and calculated dislocation densities of both α- and β-dislocations. Dislocations densities were also measured from cathodoluminescence micrographs (discussed in the next section) and these values are plotted in Figure 51.

3. Cathodoluminescence of Deformed Regions in GaAs

To characterize the surface and bulk regions of the bent and control samples without damaging the surfaces by chemical etching (in order to preserve the samples for future electrical measurements), an electron microprobe was used to study the electron beam excited cathodoluminescence from the GaAs samples. Figure 52 shows the cathodoluminescence infra-red (CL-IR) micrographs (a, b, and c) and the corresponding cathodoluminescence (CL) intensity line scans (d, e, and f) of the as-grown (A), heated but not bent (H), and bent (B) Te-doped GaAs. The micrographs were obtained from the $(\bar{1}\bar{1}2)$ surface normal to the bend axis and at the center along the edge of each sample as indicated in the accompanying sketches. Dark stripes in Figure 52a represent growth bands on (111) planes inclined at 45° relative to the (021) plane.

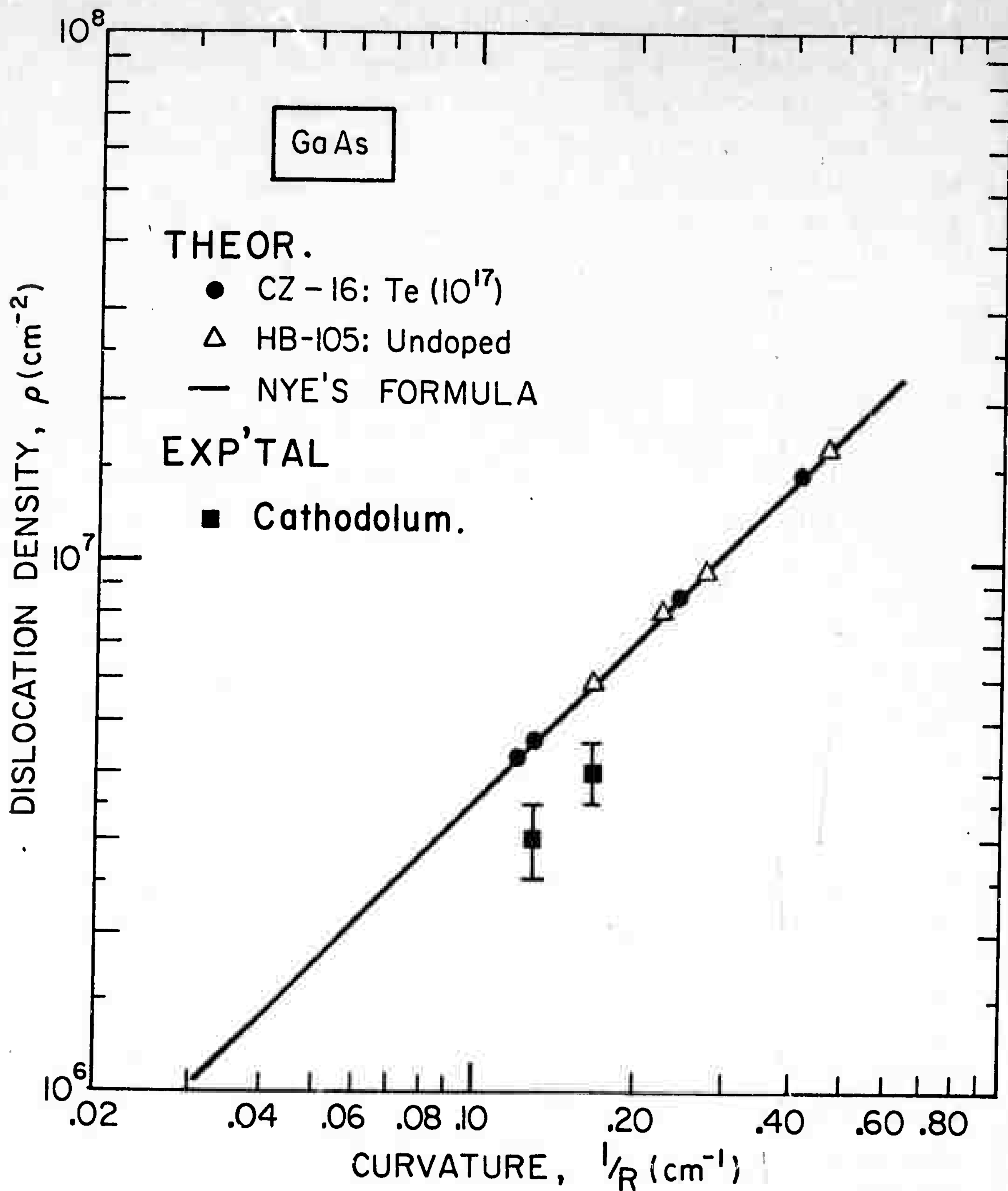

Figure 51 Calculated dislocation densities in bent Czochralski and Horizontal Bridgman crystals. Experimentally determined densities were obtained from cathodoluminescence infra-red micrographs of the bent samples.

TABLE VII

Radii of Curvature, Dislocation Types and Densities in Bent n-Type GaAs

A. Czochralski. Te (10^{17} cm^{-3})

No.	Sample No. (CZ-16)	Disloc'n Type	Curve No.	Radius of Curvature R(cm)	Curvature $\frac{1}{R}$ (cm^{-1})	Dislocation Density $\rho(cm^{-2})$	
						Calculated (a)	Exp'tl (b)
1	10-F-B1	α	B1	8.30	0.121	4.28×10^6	(c)
2	10-E-B2	β	-	7.62	0.131	4.64×10^6	$(4\pm1)\times10^6$
3	10-C-B3	β	B2	4.13	0.242	8.57×10^6	(c)
4	10-D-B4	β	B3	2.42	0.414	1.47×10^7	(c)

B. Horizontal Bridgman: Undoped

No.	(HB-105)	Disloc'n Type	Curve No.	R(cm)	$\frac{1}{R}$ (cm^{-1})	ρ (cm^{-2})	
						Calculated	Exp'tal
1	F13-C-B1	β	B1	4.98	0.167	5.91×10^6	$(5\pm1)\times10^6$
2	F11-C-B2	α	-	4.44	0.225	7.97×10^6	(c)
3	F12-C-B3	α	B2	3.78	0.265	9.38×10^6	(c)
4	F10-C-B4	β	-	2.13	0.469	1.66×10^7	(c)

(a) Using Nye's formula

(b) From cathodoluminescence infra-red micrographs of (112) surface.

(c) Cathodoluminescence work in progress.

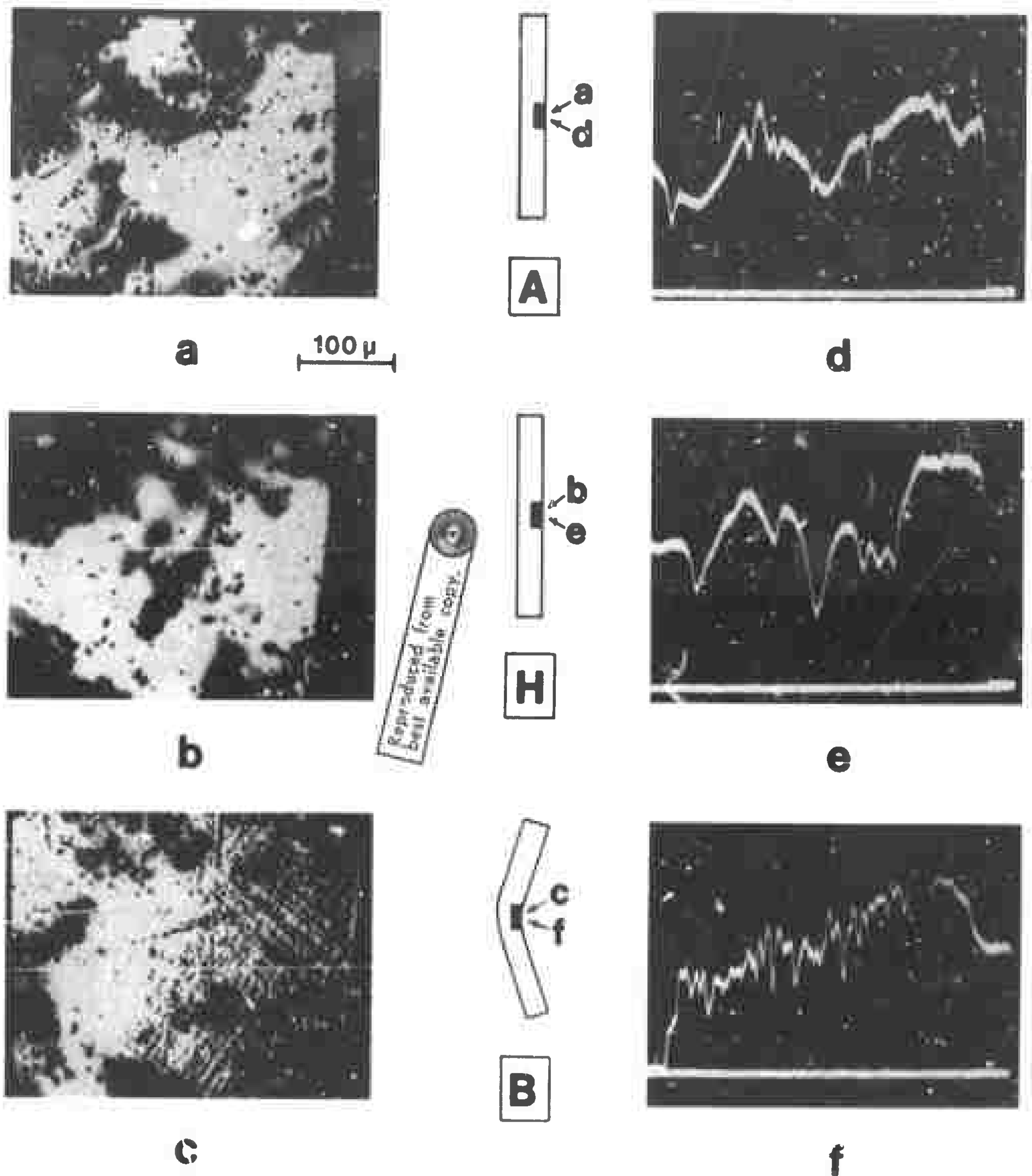

Reproduced from best available copy.

Figure 32 Cathodoluminescence Infra-red (CL-IR) micrographs of Te-doped GaAs (a, b, and c) and cathodoluminescence (CL) intensity line scan (d, e, and f) across sample. Areas examined are indicated schematically in the as-grown (A), heated (H), and bent (B) Czochralski (CZ-16) samples. The ordinate and abscissa in (d), (e), and (f) refer, respectively, to CL intensity (in arbitrary units) and distance across sample in microns.

The CL-IR micrographs (Figures 52a and 52b) show the effect of heating on the growth bands and particles visible in Figure 52a. Thus, after heating, the particles have coarsened and the distance between the bands appears to have increased, probably indicating that the dark material in the bands coalesced with the small particles to form larger particles. The mottled appearance in Figure 52 was observed only in the bent sample. It is believed that the dark patches were due to the termination of dislocation lines at the surface from which no radiative recombination took place. Thus, some estimate could be made of the dislocation densities in the bent samples, although because of the low resolution of the micrographs, the values determined from the pictures differ by 15 to 20 per cent from the calculated densities (Table VII).

The CL intensity line scans (Figures 52d, 52e, and 52f) give a qualitative picture of the homogeneity of the samples along the region scanned by the electron beam. In Figure 52d, the ordinate represents the relative CL intensity in arbitrary units, while the abscissa indicates distance along the sample surface in units indicated by the distance bar. Based on the CL line scan, it appears that the as-grown Czochralski sample gave a more uniform profile than the as-grown horizontal Bridgman (undoped) sample shown in Figure 53.

Figure 53 shows the CL-IR micrographs (a, b, and c) and CL intensity line scans (d, e, and f) for the undoped GaAs. The notations are the same as those used in Figure 52. In contrast to the doped sample in Figure 52, the undoped Bridgman samples exhibited a higher particle density (Figure 53b). Slip on the (111) planes was evident on the deformed $(\bar{1}\bar{1}2)$ surface and what are believed to be end points of dislocations on the $(\bar{1}\bar{1}2)$ plane appear as dark spots in Figure 53c.

Figure 54 shows that in a bent sample, the mottled or checkered pattern on the (112) plane was restricted to the area near the center, and that the pattern disappeared the farther one moved away from the center (Figures 54a, 54d, and 54e). Figure 54 also shows some microcracking

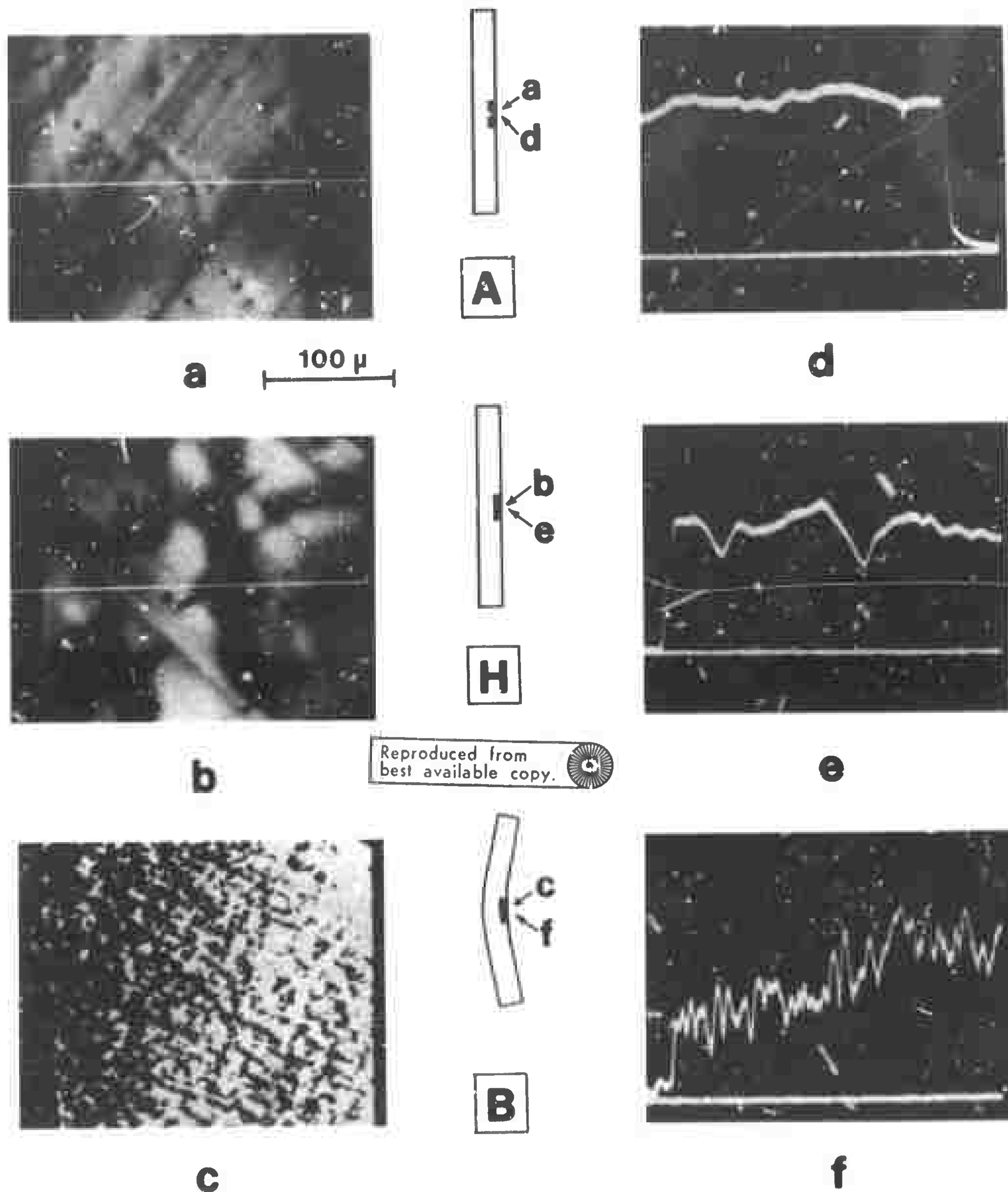

Reproduced from best available copy.

Figure 53 CL-IR micrographs of undoped GaAs (a, b, and c) and CL intensity line scans (d, e, and f) across sample. Areas in the as-grown (A) and heated (H) horizontal Bridgman (HB-105) samples are compared with the bent (B) sample.

GaAs

HB-105

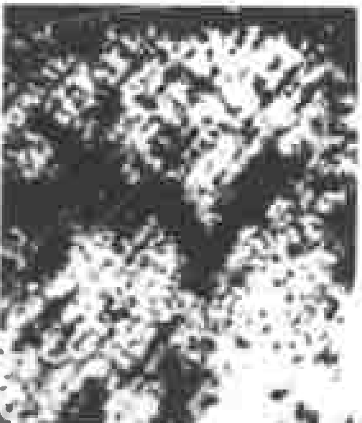

a

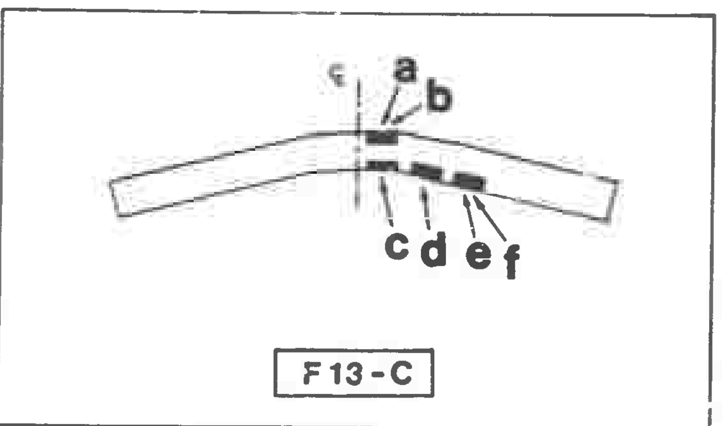

b

Reproduced from
best available copy.

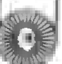

c

d

e

f

Figure 54 CL-IR micrographs (a, c, d, e) and secondary electron emission micrographs (b, f) of the tensile (a) and compressive (b) areas in a bent, undoped GaAs sample. Regions progressively removed from bend center are shown in (e) and (f).

along the upper edge, thus suggesting that the deformation was more severe on the tensile (Figure 54a) than on the compressive side (Figure 54c). The backscattered secondary electron image corresponding to the tensile (Figure 54b) and compressive surfaces (Figure 54) of the bent region revealed a featureless surface in contrast to the checkered pattern shown by the CL-IR micrographs.

Figure 55 shows CL-IR micrographs taken on both the $(\bar{1}\bar{1}2)$ surface, compressive side, (Figures 55c and 55d) and on the (021) surface, tensile side (Figures 55e and 55f). Figures 55a and 55b show featureless secondary electron images taken from two areas approximately 0.7 and 1.3 mm from the center on the $(\bar{1}\bar{1}2)$ surface, compressive side. The CL-IR, however, exhibit slip traces of (111) planes on both the $(\bar{1}\bar{1}2)$ and (021) surfaces.

Thus, with the aid of electron beam excited CL, it is possible to reveal details not otherwise visible from optical or back-scattered secondary electron micrographs. Without damaging the samples, we have delineated slip characteristics and determined dislocations densities (to a good approximation) in plastically deformed GaAs.

4. Electrical Properties

Hall measurements were made of the samples which were heated and bent in the all-quartz bend furnace. Before the electrical properties could be measured, the problem of appropriately installing ohmic contacts on bar shaped samples had to be solved. Three methods were evaluated as discussed below.

The first method evaluated consisted simply of soldering indium at six points of the bar corresponding to the six arms in a Hall bridge sample. The contacts were non-ohmic, displaying non-linear and asymmetrical voltage-current characteristics, and yielded a sample resistance of 4000 ohms or greater. The second method involved was the evaporation of a Au-Ge eutectic alloy onto the current contacts of

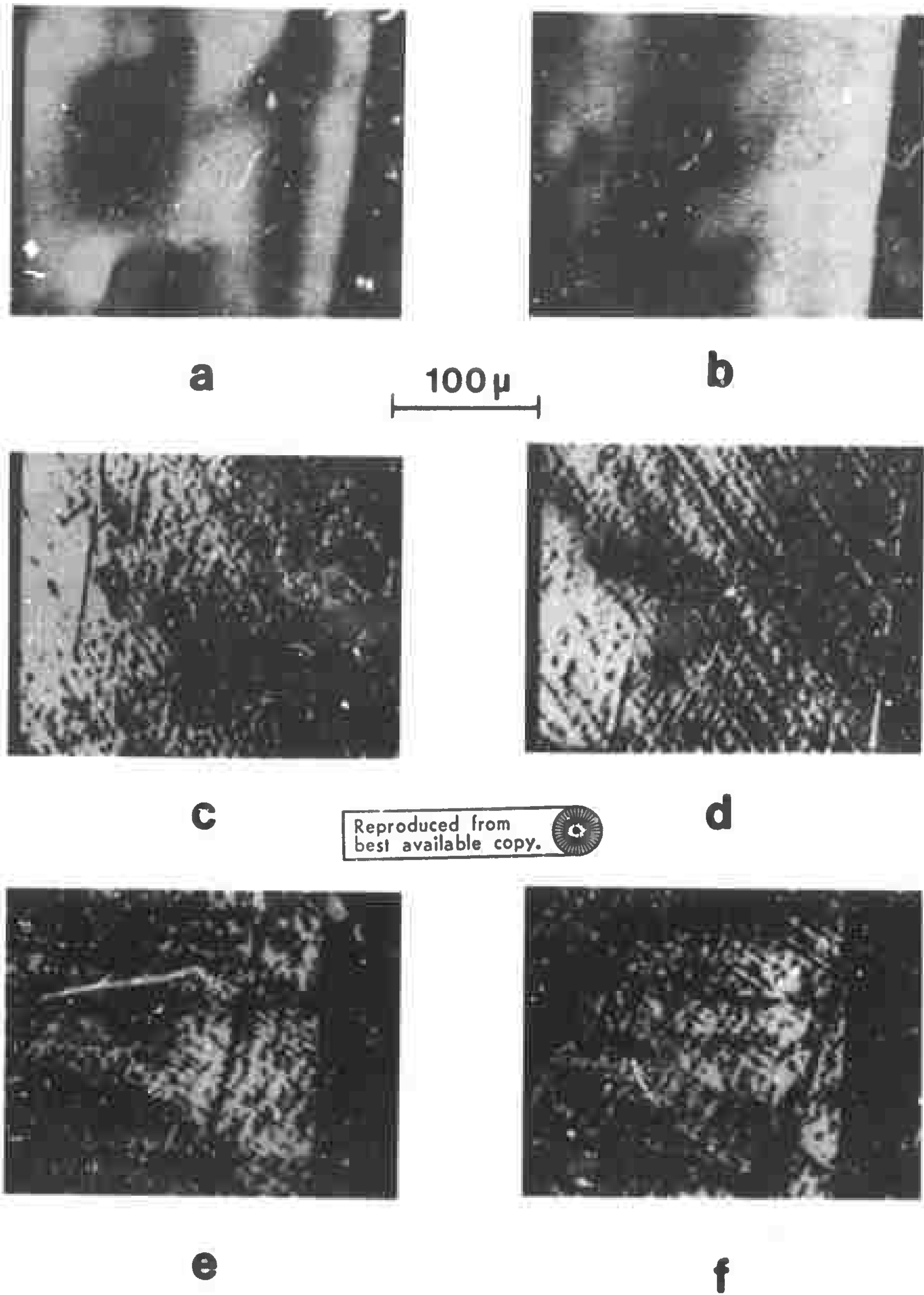

Reproduced from best available copy.

Figure 55 Secondary electron emission-micrographs (a, b) and CL-IR micrographs (c, d, e, f) of bent area in undoped GaAs sample (HB-105-F13C). Taken from $(\bar{1}\bar{1}2)$ face, compressive side are micrographs (a) and (c) (0.7 mm from bend center) and (b) and (d) (1.3 mm from bend center). Micrographs (e) and (f) were taken from (021) face, tensile side.

the sample after the method of Clawson and Wieder [13]. To keep the Au-Ge film from curling up during the alloying process, a layer of indium oxide was evaporated on the Au-Ge film. Alloying of the Au-Ge with the GaAs surface was accomplished by exposing the sample to a 400°C heat lamp. The indium oxide was subsequently removed by gently abrading the contacts. The resulting contacts were ohmic and yielded a resistance of 0.4 ohm.

The third method consisted of soldering a small amount of indium at the desired locations on the bar sample and applying momentarily the edge (not the tip) of a hydrogen flame to the spots of indium. This method assured proper alloying of the indium with the GaAs surface and yielded linear and symmetrical voltage-current curves with a sample resistance of 0.1 to 0.2 ohms.

The effect of heating during the flame soldering process was evaluated by comparing the Hall measurements taken from the same sample to which the two types of contacts were successively bonded. The first set of Hall measurements were taken after Au-Ge was evaporated onto the top surface of the bar ends (current contacts), while the second Hall data were measured after indium was flame soldered to the edge surfaces of the bar ends. Comparison of the Hall parameters taken at room and liquid nitrogen temperatures indicated a difference between the two methods of 2 to 3% in the resistivity data, and a difference of 5 to 8% in the Hall coefficient, mobility and carrier concentration. A similar range differences was found between Hall measurements taken from the same sample after a first and then a second exposure to flame soldering.

This third method of attaching indium contacts by hydrogen flame soldering was subsequently adopted as standard because it yielded low resistance ohmic contacts, presented a bright and clean surface, and because the variations in the measurements were within experimental error. A further reason for using this method was that with the aid of

a suitably designed sample holder, the leads could be attached to the sample with a minimum of sample handling, no subsequent cleaning, and thus eliminated possible sources of specimen contamination.

Hall parameters were calculated from resistivity and Hall voltage data obtained at temperatures ranging from 77°K to 300°K from a DC Hall apparatus with a 5 kG magnet (Courtesy of Dr. H. Wieder, U.S. Naval Electronics Center, San Diego). Sample currents varied from 10 to 20 mA. Reproducibility of the measurements was 1 to 2% for the resistivity data and 2 to 5% for the Hall coefficient, mobility and carrier concentration.

The Hall parameters as a function of reciprocal temperature for the as-grown (A), heated (H) and bent (B) Horizontal Bridgman (HB-105) and Czochralski (CZ-16) samples are shown in Figures 56, 57, 58, and 59. The letter-number combinations identifying the samples are referenced in Table VIII. The Greek symbols refer to the predominant type of dislocation introduced into the sample by bending. The samples are grouped such that there is one α- and one β-type bend sample from the undoped HB-105 and doped CZ-16. The B3 sample in the figures refer to a sample that was oxidized after bending and during the cooling period.

Although the Hall parameters of the individual samples displayed very little temperature dependence because of the high carrier concentrations present, the relative differences between the curves for the control and bent samples were sufficiently large to permit determination of the effects of bending and short term heating (10 to 20 minutes) in the temperature range of 600° to 700°C.

The effect of short term heating (measured relative to the as-grown sample) on the undoped GaAs crystal (HB-105) was to increase the Hall coefficient by 20% (Figure 56), decrease the carrier concentration by 17% (Figure 57), decrease the conductivity of 7% (Figure 58) and increase the mobility by 12% (Figure 59). For the Te-doped sample

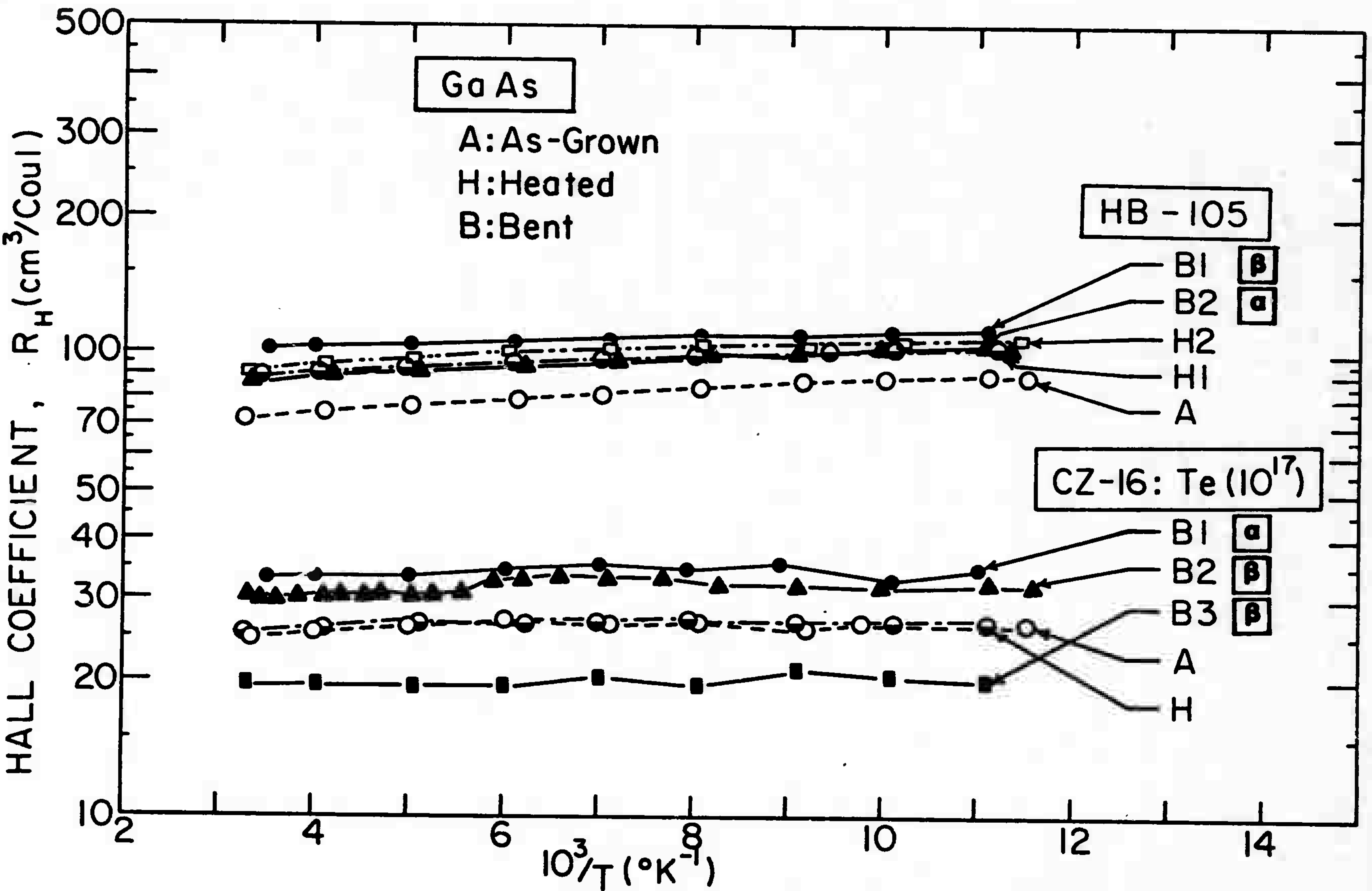

Figure 56 Hall coefficient vs. reciprocal temperature for Te-doped Czochralski (CZ-16) and undoped horizontal Bridgman (HB-105) samples of As-grown (A), heated (H, H1, H2) and bent (B1, B2, B3) GaAs. Majority dislocations introduced during bending are referred to by α and β.

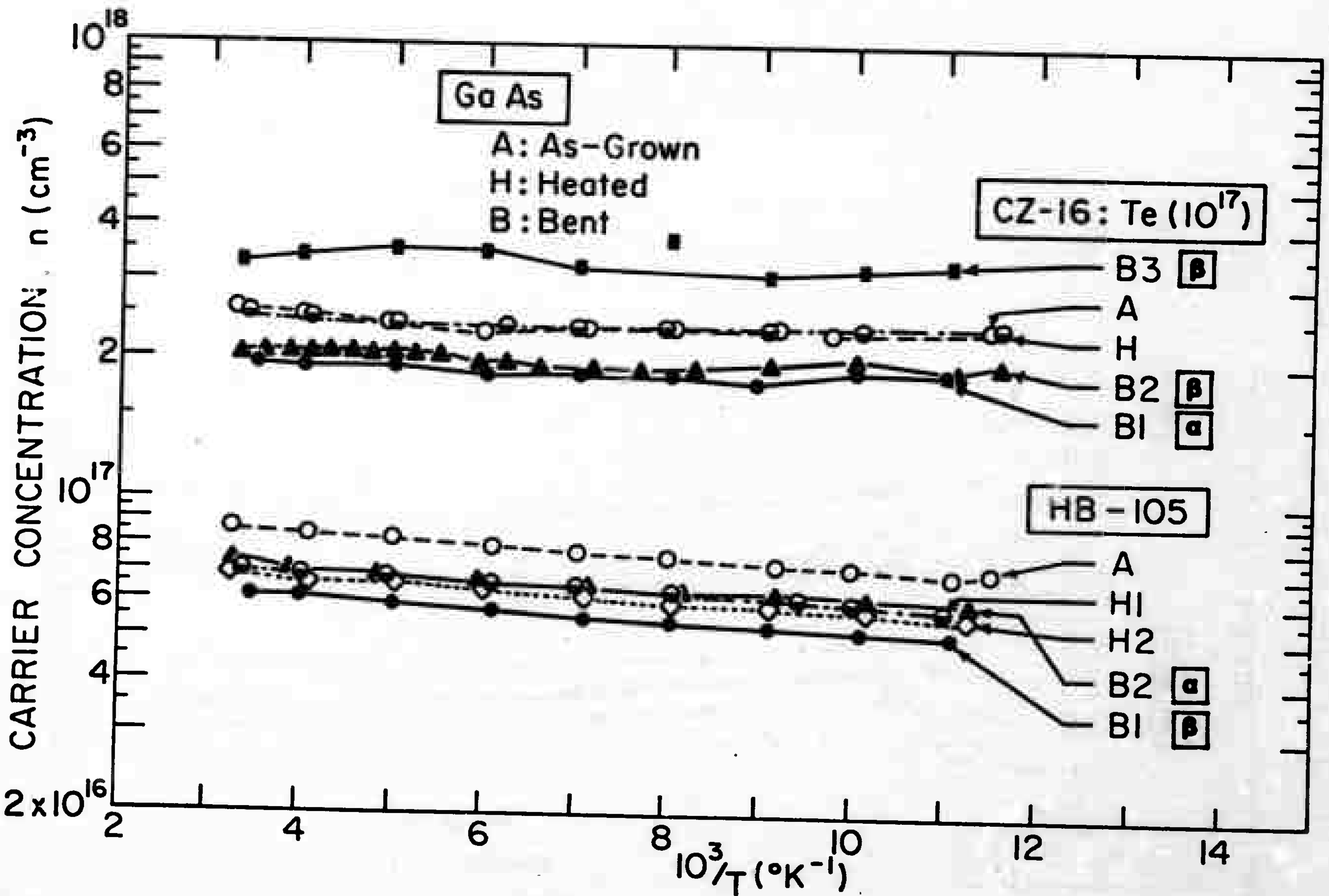

Figure 57 Carrier concentration vs. reciprocal temperature for As-grown (A), heated (H), and bent (B) horizontal Bridgman (HB-105) and Czochralski (CZ-16) GaAs.

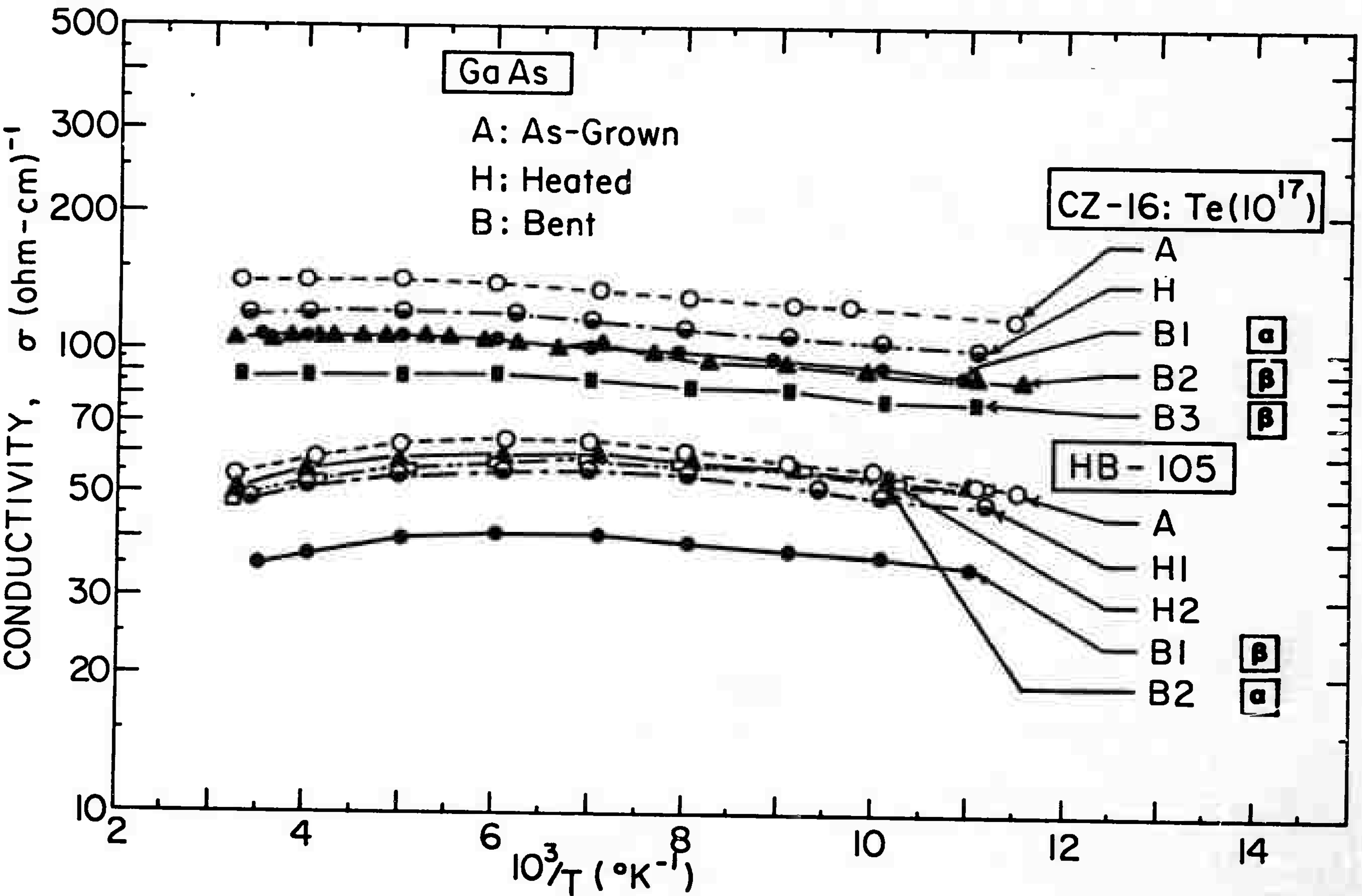

Figure 58 Conductivity vs. reciprocal temperature for As-grown (A), heated (H), and bent (B) horizontal Bridgman (HB-105) and Czochralski (CZ-16) GaAs.

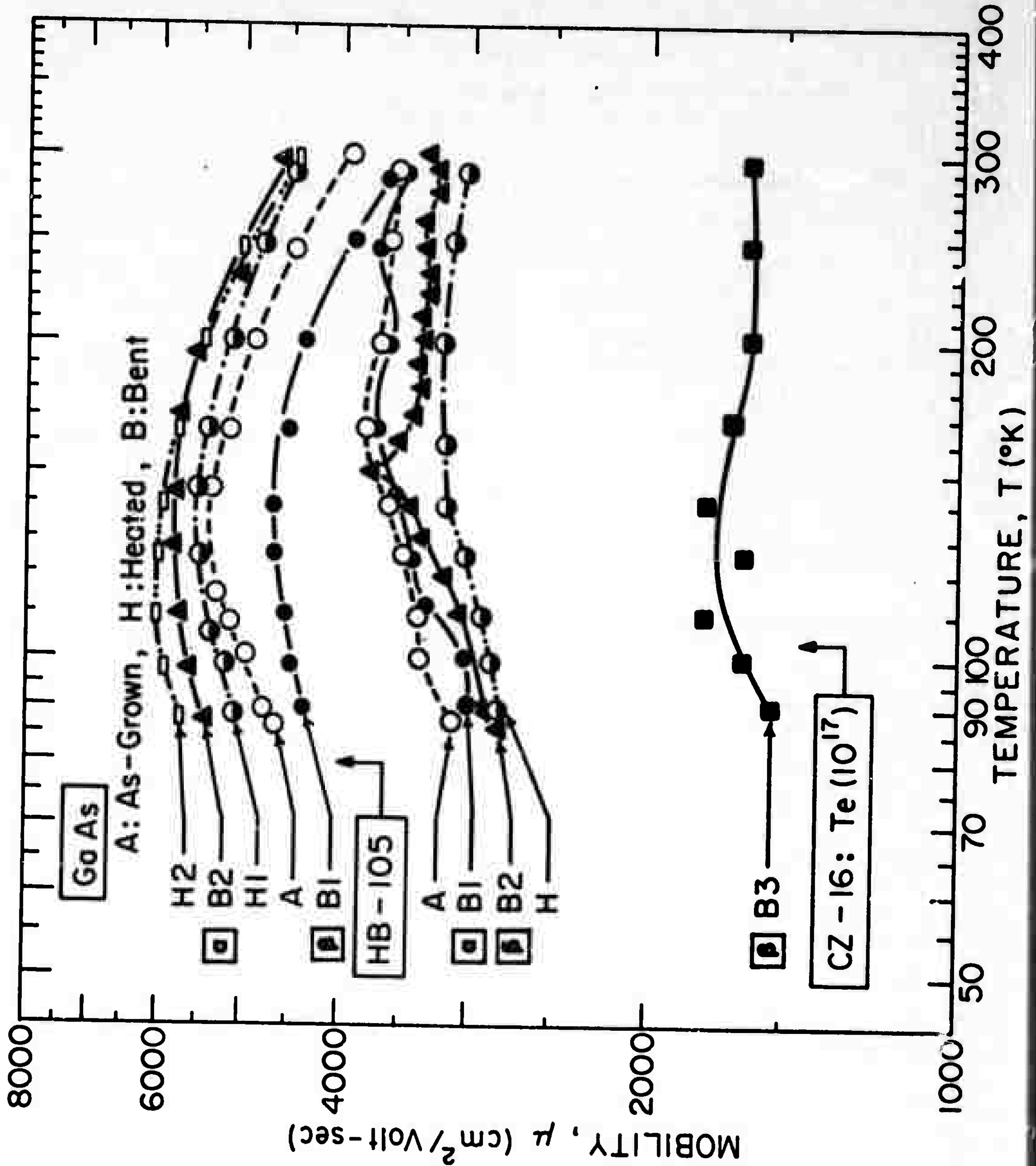

Figure 59 Mobility vs. Temperature for As-grown (A), heated (H), and bent (B) horizontal Bridgman (HB-105) and Czochralski (CZ-16) GaAs.

TABLE VIII

Relative Changes in Hall Parameters After Heating and Bending of n-Type GaAs

A. Effect of Heating on the Unbent GaAs Relative to the As-Grown Sample

No.	Sample No.	Curve No. (a)	Percent Changes at 77°K			
			Hall Coeff. (R_H(cm^3/coul)	Carrier Conc'n n(cm^{-3})	Conductivity σ(ohm-cm)$^{-1}$	Mobility μ(cm^2/V-sec.)
1	CZ-16 9-B-H	H	-0.2	+0.8	-14.7	-14.7
2	HB-105 F13-B-H1	H1	+19.8	-16.7	- 7.2	+11.5
3	HB-105 F12-B-H3	H2	+ 8.5	- 7.5	+ 6.2	+15.3

B. Effect of Bending on the Heated GaAs Relative to the Heated But Unbent Sample.

No.	Sample No.	Curve No. (a)	Disloc'n Type	Calculated Disloc'n Density ρ(cm^{-2})	Percent Changes at 77°K			
					R_H (cm^3/coul)	n (cm^{-3})	σ (ohm-cm)$^{-1}$	μ (cm^2/V-sec)
1	CZ-16 10-F-B1	B1	α	4.28×10^6	+ 31.0	-21.3	-12.4	+14.7
2	HB-105 F12C-B3	B2	α	9.38×10^6	- 5.1	+ 5.4	+ 1.6	- 4.4
3	HB-105 F13C-B1	B1	β	5.91×10^6	+16.1	-14.8	-27.4	-15.5
4	CZ-16 10C-B3	B2	β	8.57×10^6	+22.4	-18.8	-14.[illegible]	- 4.85
5	CZ-16 10D-B4	B3	β	1.47×10^7	-22.45	+36.4	-23.53	-42.28

(a) refers to Hall Parameter vs. Reciprocal Temperature Curves.

(CZ-16), heating had no effect on the Hall coefficient or carrier concentration and produced a 15% decrease in the conductivity and mobility. Thus, the decrease in the carrier concentration after heating was limited to the undoped sample, while little or no change in carrier concentration was noted in the doped sample. (Table VIII). Because the role of impurities such as copper and carbon in GaAs is quite complex [18], no definite mechanism has as yet been assigned to explain the observed phenomena. However, it is quite certain that heating, even though of short duration has affected the electrical properties of GaAs, as has been observed by others [19,20].

The microstructure observed in both the doped (Figures 52a and 52b) and undoped heated samples (Figures 53a and 53b) appears to have no direct relationship to the changes after heating in the carrier concentration or mobility. Thus, the increase in size of the particles in CZ-16 probably has no bearing on the decrease in mobility, nor does the absence of change in the particle size in HB-105 appear to be related to the increase in mobility.

The effect of bending on the Hall parameters of both the doped and undoped samples are shown in the same set of figures (56-59). Because of the two types of dislocations introduced and because of the varying dislocation densities involved, the changes in the Hall parameters of the bent samples are summarized for convenient reference in Table VIII. It is to be noted that the changes recorded are those changes in the parameters after the effects of heating had already been taken into account.

The principal effects of dislocations (in other semiconductor materials) when these lie parallel to the bend direction and normal to the current flow have been: a decrease in carrier concentration, conductivity and mobility [21-23]. Table VIII indicates that these effects appear verified in the case of β-dislocations (especially sample B3) but not consistently in the case of α-dislocations.

The large changes observed in the oxidized sample, B3, are noteworthy because it appears that the oxidation was not limited to the surface but also affected the bulk in such a manner as to produce a 36% increase in the carrier concentration, a 42% decrease in mobility, and a 23% decrease in conductivity. This observation does not appear consistent with the classification of oxygen as a trap [18]. Furthermore, the changes in the dislocation density appear to have no effect on the parameters. This is not surprising because the number of available donor or acceptor sites introduced by a dislocation density of 1.47×10^{7} cm^{-2} (the maximum listed in Table VIII) amounts to 2.65×10^{13} cm^{-3}, assuming that the fraction of sites occupied is 0.1. Thus, with carrier concentrations ranging from 10^{16} to 10^{17} cm^{-3}, changes in the acceptor site density of 1.8×10^{9} to 2.65×10^{13} cm^{-3} will not produce significant effects on the parameters unless other factors such as impurties also play a role.

Because the effects observed due to bending (after taking into account heating effects) are significantly large, they will have to be explained in terms of the complex interaction between the dislocations and impurities. Previous work with plastically deformed higher purity semiconductors have shown the directional property of charge carriers with respect to the orientation of dislocations [21-23]. Thus, the maximum decrease in the conductivity and mobility resulted when the current flow was normal to the dislocation lines, while little or no change was observed when the current flow ran parallel to the dislocations. This implies that impurities in a semiconductor do not have the directional properties of dislocations.

An experiment, therefore, is planned to sort out the effects due to dislocations from those due to impurities by a passing a current in the bent sample parallel and perpendicular to the bend axis. The effect of impurities (whether or not precipitated on the dislocations) on the mobility and conductivity will be evident when current is run parallel to the bend axis. Similarly, the corresponding effect of dislocations

(combined with the impurities) will be noted when current is run normal to the bend axis. Thus, it will be possible to differentiate between the effects due to impurities only, and those due to a combination of dislocations and impurities, and finally those due to dislocations only.

C. Electron Microprobe Investigations

Some microprobe studies have already been reported in Sections I.E.1 and IV.A.

1. Cathodoluminescence of $GaAs_{1-x}P_x$

The experimental results on the $GaAs_{1-x}P_x$ system described here were obtained using X-ray microanalysis to determine the composition of the samples and the clean electron beam column [24] for temperature dependence of cathodoluminescence studies. All cathodoluminescence measurements were made using a beam voltage of 50 kV to reduce the effect of surface recombination. The sample temperature was variable from 27°K to 300°K. The samples were mounted on a copper sample holder using indium. The samples were pressed into the indium either while it was hot or at room temperature. At no time was any sample contamination due to electron irradiation seen.

Cathodoluminescence measurements were made as a function of temperature and beam current on the $GaAs_{1-x}P_x$ mixed crystals. As x increased from 0 to 1, the nature of the mixed crystal changed from a direct to an indirect band gap semiconductor. This occurred at a value of $x = 0.4$ to $x = 0.5$. The samples were first analyzed to determine the composition using electron probe X-ray analysis and J. W. Colby's [25] MAGIC computer program for quantitative electron microprobe analysis. The results of these measurements are shown in Figures 60 and 61.

Figure 60 shows the peak energies of the cathodoluminescence spectra as a function of crystal composition at 30°K (upper curve) and at 300°K (lower curve). The cross-over (direct to indirect band gap)

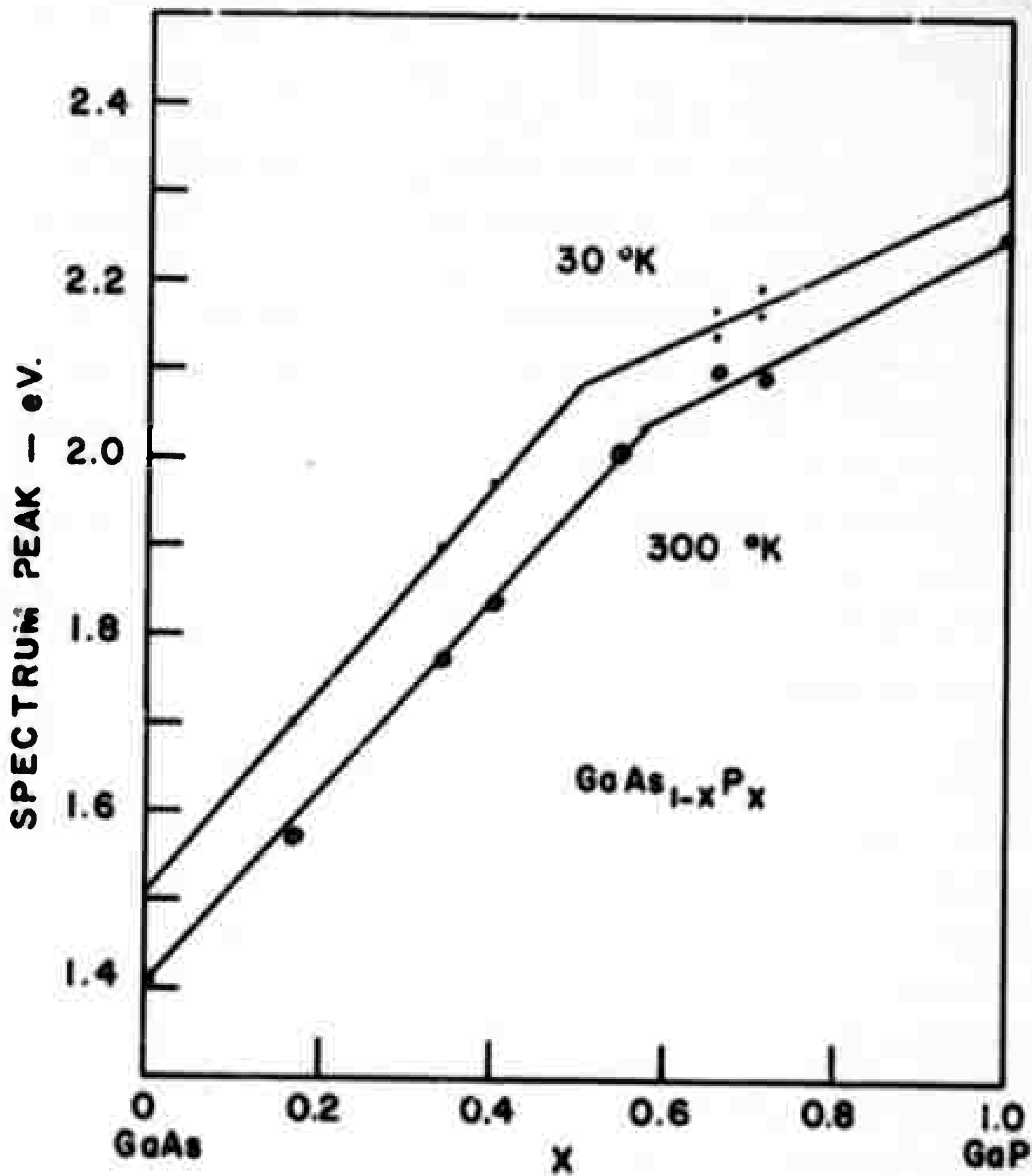

Figure 60 Composition dependence of cathodoluminescence spectrum peak of $GaAs_{1-x}P_x$ crystals. Upper curve at 30°K, lower curve at 300°K.

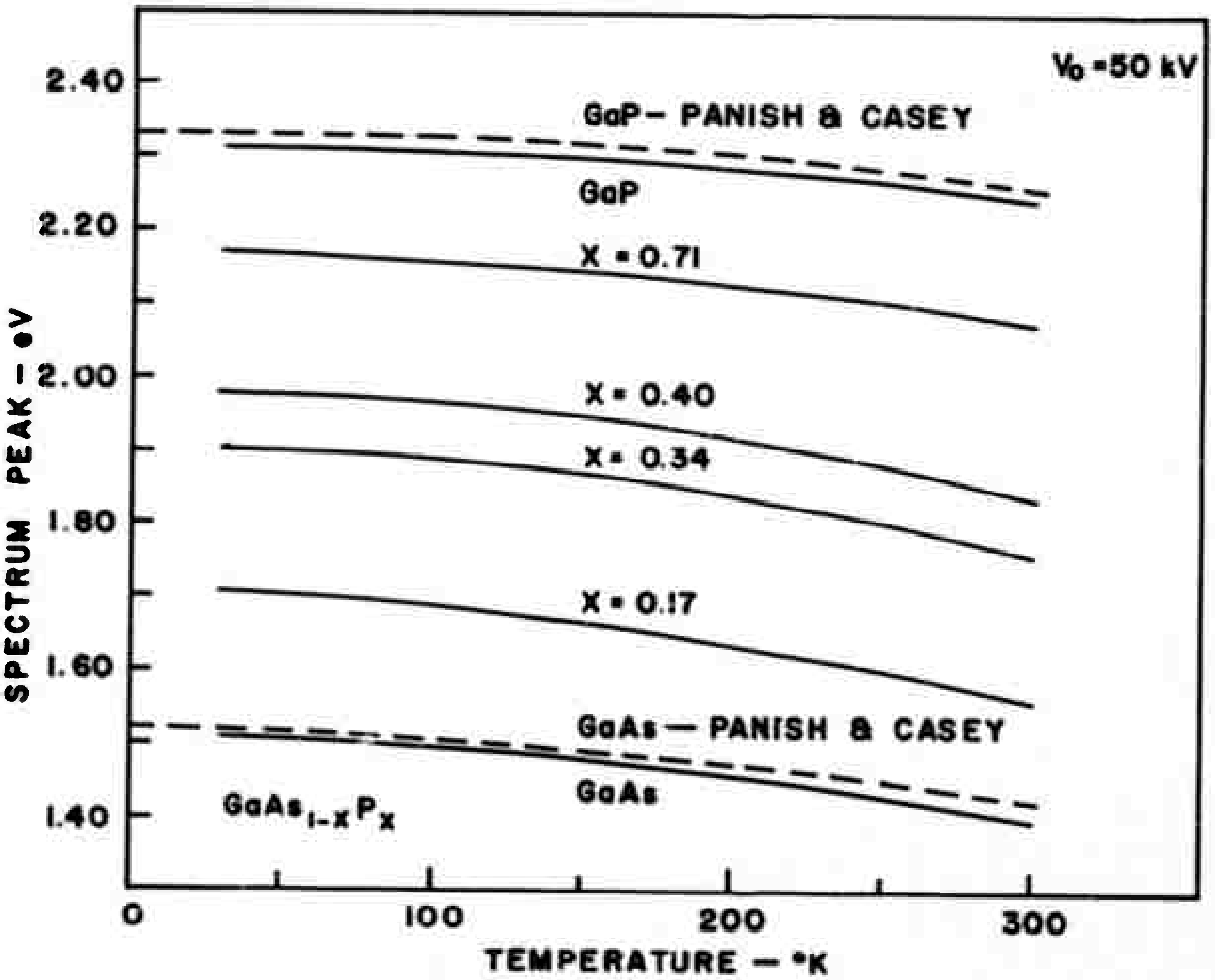

Figure 6: Temperature dependence of cathodoluminescence spectrum peak of $GaAs_{1-x}P_x$ crystals.

point is at x = 0.45 to x = 0.50 which is close to that measured by others whose values ranged from 0. to 0.45 [26-28]. Differences could be due to different methods of measurement as well as differences in the samples measured.

Figure 61 shows the temperature variation of the energy peak of cathodoluminescence spectra of the various $GaAs_{1-x}P_x$ crystals. The upper and lower dashed curves show the absorption edge of GaP and GaAs versus temperature according to Casey and Panish [29]. The curves are all fairly parallel and show the same temperature dependence whether the material is direct or indirect in nature. Departure from this parallel behavior at higher temperatures and values of x = 0.0 to x = 0.4 can be explained by electron beam heating which is higher at these points because the thermal conductivity is lower for these samples at these temperatures [30,31]. The thermocouple, located about 0.5 cm from the beam spot would not detect this heating effect. For pure GaP no such heating has been observed at any sample current value available with this instrument because the thermal conductivity of GaP is quite high compared to GaAs and $GaAs_{1-x}P_x$ for $x < 0.8$.

In one sample whose x value was 0.71, a 40 meV downward shift of cathodoluminescence peak energy was measured as the sample current changed from 0.3 to 1.1 µA. According to the band gap variation with temperature, this corresponds to a temperature rise of 50K°. Using a value of 0.2W/cm°C for the thermal conductivity and the formula for temperature rise due to electron beam irradiation given by Almasi et al [32], which assumes an infinitely thick sample, one gets a temperature rise of 40K°. Differences could be accounted for by differences in sample thickness and the nature of the indium contact with the sample.

2. Stimulated Emission of GaAs

Attempts have been made to produce superradiance from electron-

beam excited heavily-doped n-type GaAs. Surprisingly, the results reported by Casey and Kaiser [33] could not be duplicated either at room temperature or at 113°K. A linear decrease of spectrum energy peaks with increasing beam current and a decrease of radiation intensity with beam current after a certain value of beam current was reached were observed at both of these temperatures. While Casey and Kaiser did not observe these effects, our observations could be attributed to improper thermal contact between sample and sample holder, which would have caused a large temperature rise of the sample during electron irradiation.

With improved methods for specimen mounting, we were still unable to observe the results reported by Casey and Kaiser. Also, the application of a uniaxial strain failed to enhance the intensity significantly.

In order to understand the production of stimulated emission, we are now making experiments using a cavity formed by the chemically polished surfaces of a thin specimen ($\sim 50\mu$ or less in thickness). Clear cavity modes of about 30A° apart were observed in these samples at room temperature. Since the threshold beam current for stimulated emission could be an order of magnitude less at low temperature than at room temperature, we are now making experiments at $\sim$110°K temperature to observe stimulated emission.

3. Transmission Electron Microscopy

A modification to the ultrasonic cutter has been designed so that specimens can be cut for subsequent thinning by jet etching. The parts for this modification are now being fabricated in the shop. A jet polishing apparatus is also being set up.

D. GaAs Photoluminescence Measurements

Low-temperature photoluminescence measurements have been made on GaAs samples cut from six crystals grown at USC. Five of the

samples were grown by the liquid-sealed Czochralski technique (Section I.A), the sixth was grown by the horizontal Bridgman technique. One of the Czochralski-grown crystals and the Bridgman-grown crystal were not intentionally doped, the remaining crystals were doped with Te and combinations of Mg, S and Se. Photoexcitation was by helium-neon laser (6328 Å, 1.96 eV), filtered to remove long-wavelength laser lines. Photoemission in the wavelength region 0.8 to 1.05μ (1.55 to 1.18 eV) was analyzed with a Perkin Elmer E1 monochromator and detected with a cooled RCA 7102 photomultiplier. The photomultiplier output was amplified by conventional phase-sensitive techniques and recorded on chart paper.

Luminescence measurements in GaAs are complicated by the fact that impurity banding occurs at very low impurity concentrations ($\sim 10^{16}/cm^3$) due to the low carrier effective masses. Such banding greatly broadens the energy levels associated with impurity-assisted recombination. Thus, when banding occurs it is often possible to determine the general class of impurity present (shallow donors, deep acceptors, etc.) and the transition mechanism involved, but it is not possible to identify impurity atomic species.

Of the samples examined, only the Bridgman-grown specimen was pure enough to show some luminescence from free excitons or from excitons bound to neutral shallow donors or acceptors. Even in this sample, the dominant luminescence appeared to involve free-to-bound or shallow donor-acceptor pair recombination. The undoped Czochralski-grown sample appeared to be less pure and gave evidence of possible donor-acceptor pair or free-to-bound acceptor recombination. This result is in general agreement with the results of other characterization studies of this material which suggest compensation and Si contamination. The spectra from the Te-doped GaAs were dominated by possible free-to-bound transitions involving the Te donor. Some evidence for bound exciton recombination at neutral Te donors exists in the more lightly

doped sample. In the more heavily doped sample, contamination by deep acceptor impurities such as Fe, Zn, Cd, Cu, etc., is suggested. The Mg: Se- and Mg: S-doped samples produced broad-band luminescence which could be interpreted as donor-acceptor pair recombination. Other interpretations involve Si or some deep acceptor. More exact interpretation of the data simply is not possible due to the effects of impurity banding and the confused and often contradictory state of the GaAs photoluminescence literature. It should be pointed out that free and bound exciton recombination are not commonly observed in bulk GaAs and that nearly all such spectra reported come from high-purity epitaxially-grown material.

E. High Impedance Hall System

During the past year we completed the design and construction of a system for making Hall effect measurements on high impedance samples. The circuitry features electric suppression of cable capacitance and leakage effects in both the current supply and voltmeter leads. The Hall sample current is programmable and the current source has an effective leakage resistance greater than 10^{12} ohms. The voltmeter circuit is balanced and has independent conpensation for the leakage resistance and capacitance of each lead to a level greater than 10Ω ohms. The operational amplifiers used are varacter bridge amplifiers. The converse of the voltmeter is also guarded to yield a common mode resistance of the order of 10^{12} ohms. When the high impedance features are not required, this voltmeter can be bypassed and replaced by a balanced digital voltmeter with a decrease in noise level. The system is capable of measuring samples with a resistance of the order of 10^{10} ohms without applying more than 10 volts across the current terminals of the Hall sample.

We are currently calibrating the temperature sensor in our Hall cryostat and have made several system modifications to reduce the difference between sample temperature and control sensor temperature.

The system is now being used routinely for measurements at room temperature and will shortly be used for the analysis of GaAs crystals which have shown strong effects of carbon in local mode studies (Section IV). We also plan to see how the combination of Hall and capacitance studies can be used to characterize very high impedance material. For example, one of the samples we measured recently had a sample resistance of the order of $10^9\ \Omega$, a nominal carrier concentration of $10^9/cm^3$ and mobility of $1\ cm^2$/volt-sec. The sample was in the van der Pauw configuration and was 25 mils thick. If the free carrier concentration were equal to the net donor doping, the depletion widths given expected surface potentials would have almost completely depleted the sample from both sides. This would have a profound effect on effective doping and mobility. Accordingly, we plan to study the capacitance and Hall effect of such samples in an FET configuration which should help us to eliminate some of these geometrical effects in the characterization of high resistivity material.

F. Tunnel and Thermal Effects in Photoemission in Schottky Barriers

The work described in last year's report [1] has undergone some extension and revision. This work was intended to present in a clear fashion the thermal and tunneling perturbations introduced into Schottky barrier height measurements determined by photoinjection of carriers from the metal into the semiconductor. This is important when interface effects are to be studied because the photodetermined barrier is still the most directly measurable quantity and a comparison with capacitance methods or thermionic emission measurements for lightly doped semiconductors is then useful for describing the interface. For heavily doped semiconductors, the perturbations introduced by tunneling are for the normal current-voltage characteristic but are still relatively small for phtoinjection. In addition to the function of helping to determine a "standard" measurement of barrier height we also wished to determine the bias dependcnce of photoinjection for Schottky barriers. This

determination permits photoinjection from Schottky barriers to be used to initiate avalanche multiplication in a precisely defined fashion.

We have written a short paper on the thermal effects on a Fowler photohold plot [34] and are preparing a manuscript which is summarized below. We found, upon careful examination, that the quantum mechanical transmission for electron near the barrier energy is dependent almost entirely upon the electric field at the semiconductor surface, rather than upon the band bending in the surface depletion layer. This made it feasible to calculate results for a variety of temperatures and electric fields (i.e., a two parameter theory) rather than for three parameters; viz., temperatures band bending and semiconductor doping. Representative predicted plots of the square root of the photoreference versus hv $-\phi_B$ (where ϕ_B is the barrier height) are shown in Fig. 62. Note that for quantum energies (hv) 0.1 eV in excess of the barrier, appreciable derivatives between time and apparent threshold over. The 0^oK results show the tunneling effects which predominate at low temperatures.

Figure 63 shows some interesting features determined by an electric field in the semiconductor, image force near the metal surface and Thomas-Fermi field perturbation into the metal of the equivalent one determined potential well seen by an electron which crosses a barrier. Electrons with appreciable off-axis momentum see the dashed barrier where V_{TK} is the energy required in the metal to conserve transverse k. This type of phenomenon should be important in negative affinity electron emitters. It is very interesting, however, that in the case of <111> Si on An the predicted transmission coefficients are actually higher because of the transverse h (cf. Fig. 64). This occurs because the spike in the barrier potential occurs within a Thomas-Fermi screening length which is $\approx 0.5\mathring{A}$ and is thus almost completely transparent. The shallower effective potential step reduces the wave vector change between the two media and this increases the transmission. Figures 65a, b, c give results for the difference between true barrier and apprent barrier from the Fowler

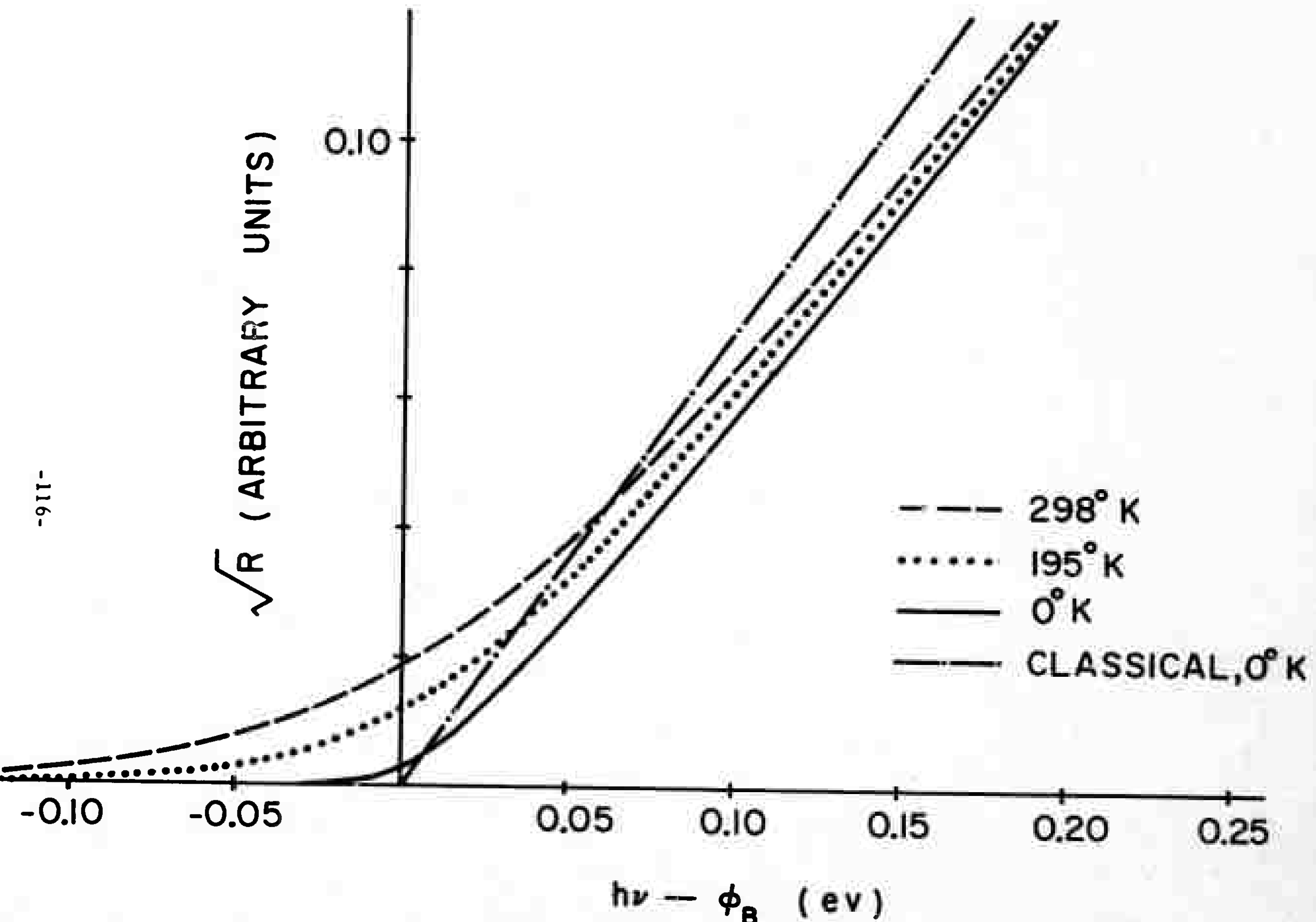

Figure 62 Square root of the photoreference versus the excess of the quantum energy over the barrier height for phtoinjection from the metal into the semiconductor of a Schottky barrier. Quantum mechanical transmission and thermal effects from the Fermi-Dirac tail of the photoexcited distribution are included in all but the classical 0°K result. One-dimensional effective electron.

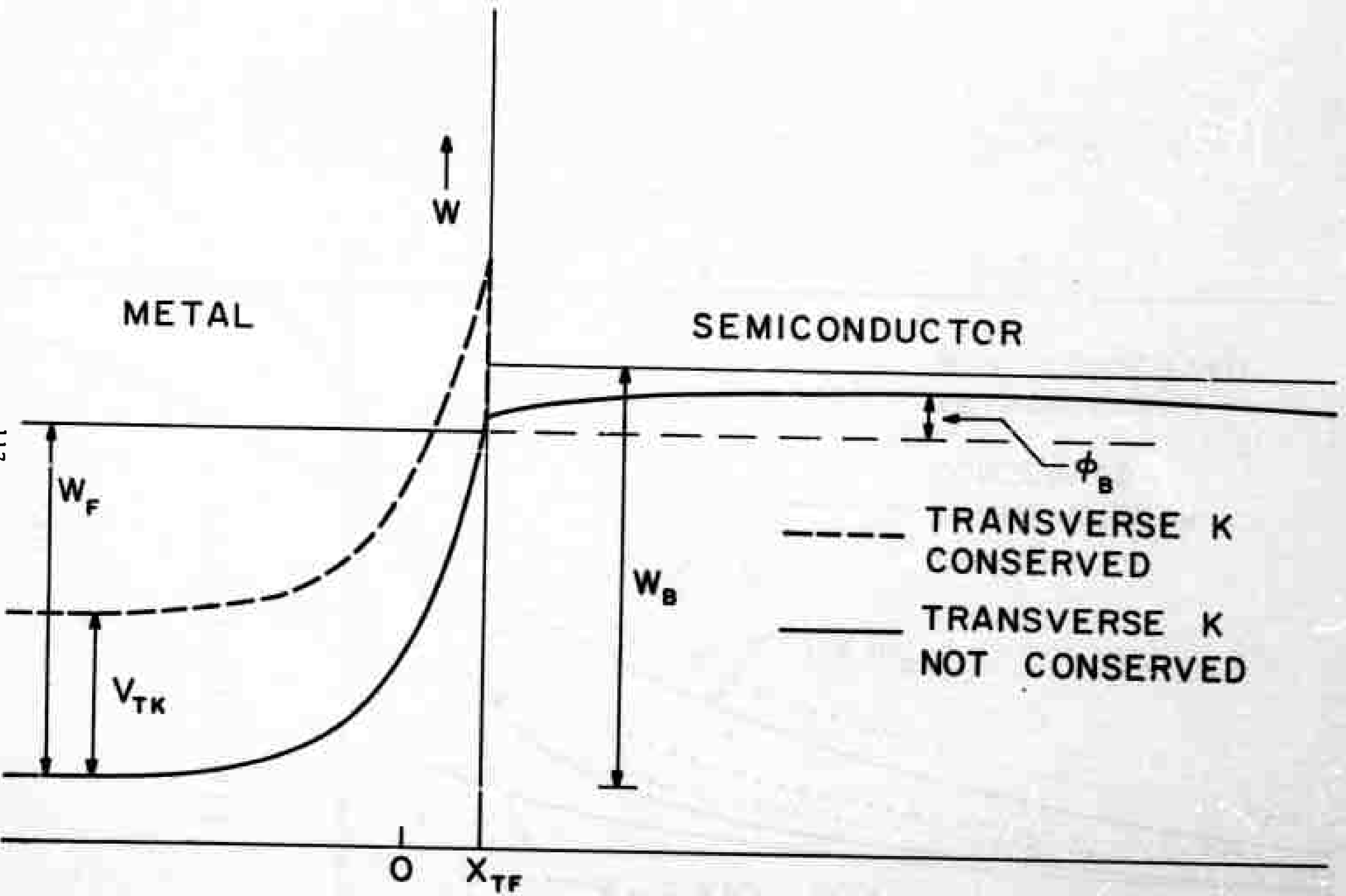

Figure 63 Typical one-dimensional effective electron potential energy barrier for a Schottky barrier when an electron conserves and does not conserve transverse momentum when crossing the interface.

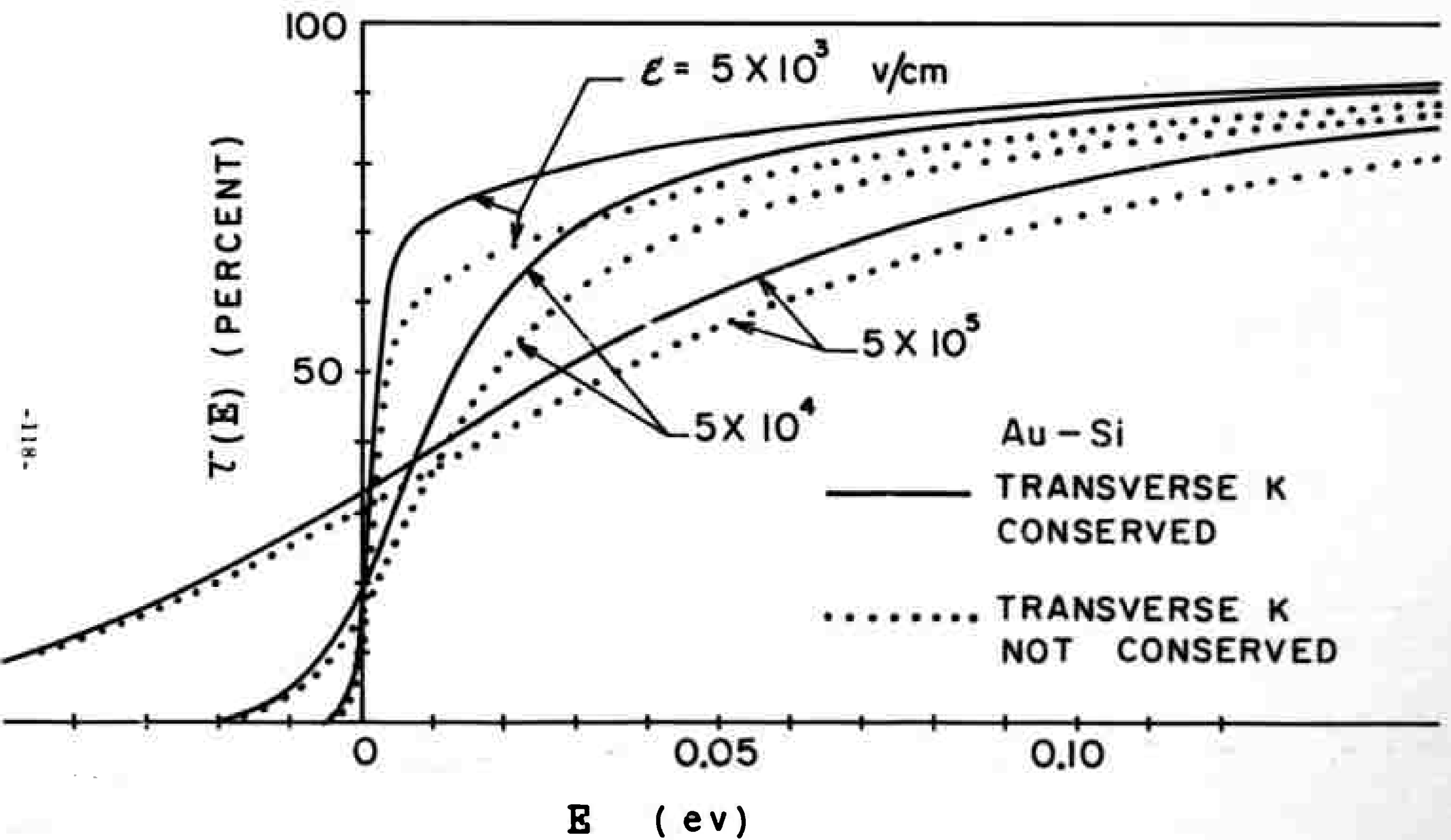

Figure 64 Effect of conservation of transverse k on transmission coefficient as a function of energy for Schottky barrier for Au on < 111 > n-type Si as a function of semiconductor electric field at the interface.

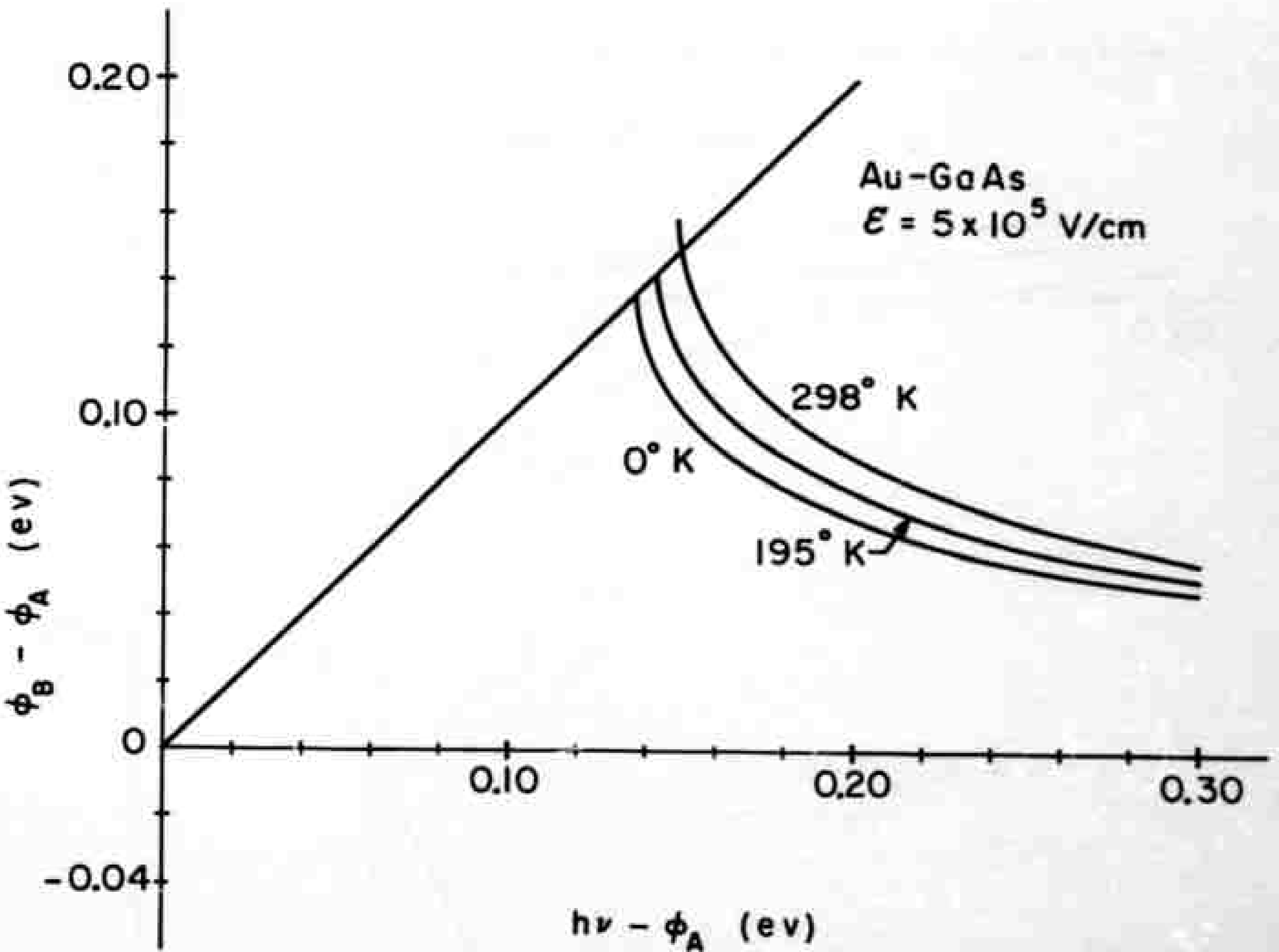

Figure 65a Difference between true and apparent barrier heights for Au-GaAs Schottky barriers as a function of the difference between the energy of the incident photon and the apparent barrier height for an electric field of 5×10^5 V/cm.

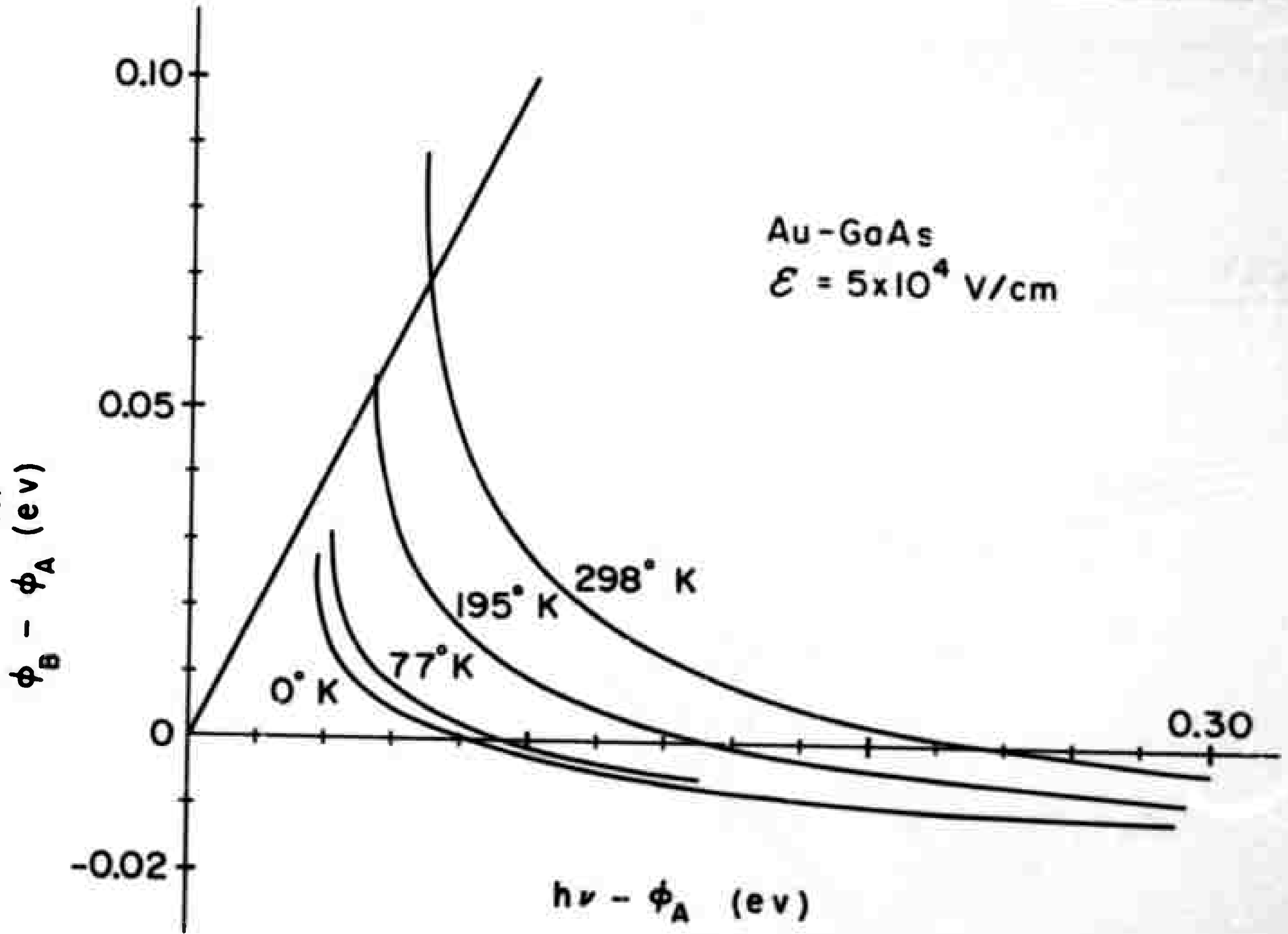

Figure 65b Au-GaAs Schottky barriers at an electric field of 5×10^4 V/cm.

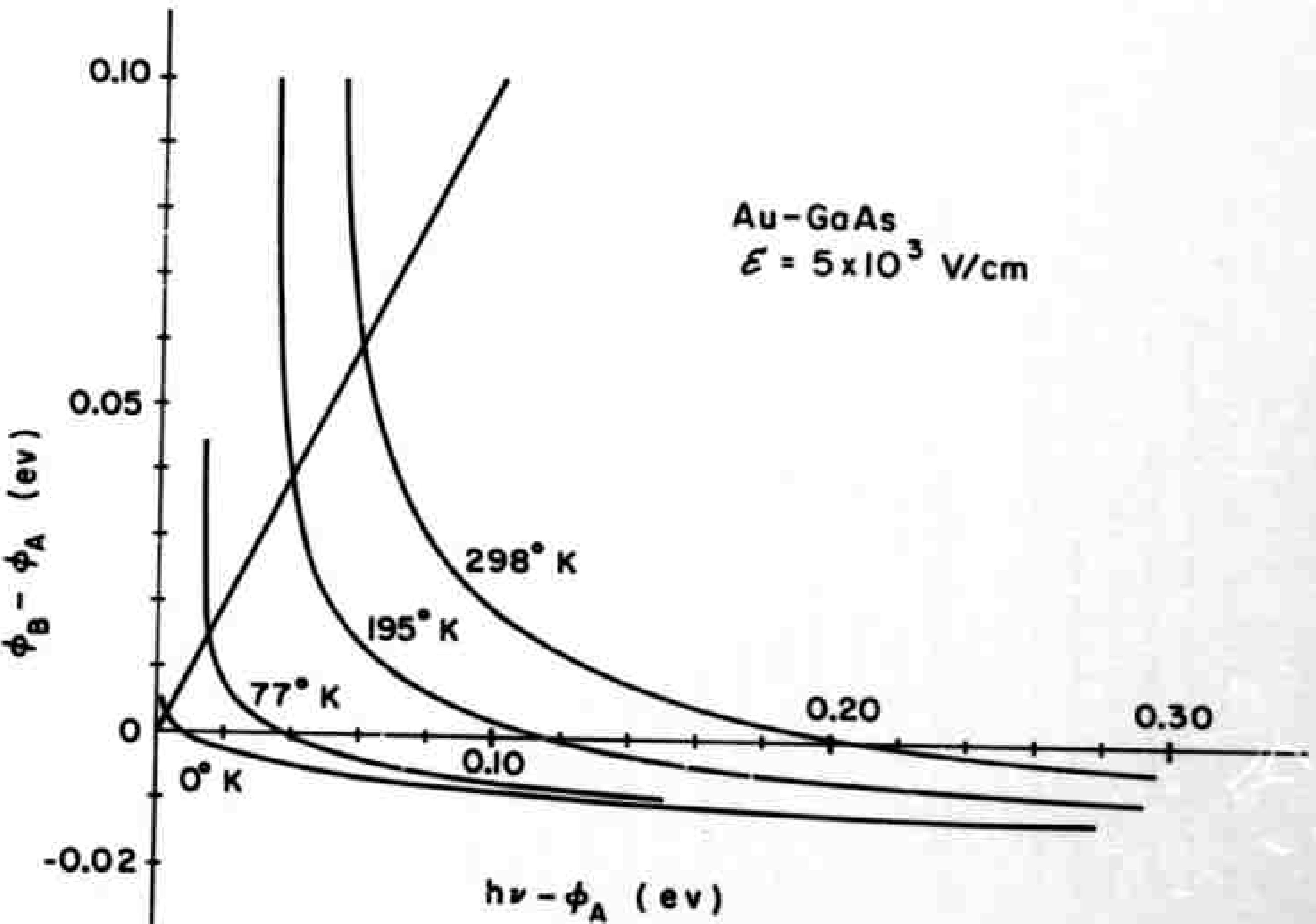

Figure 65c Au-GaAs Schottky barriers at an electric field of 5×10^3 V/cm.

plot intercept, φ_a, as a function of $h\nu - \phi_a$ for selected temperatures and electric fields for Au-GaAs barriers. The results are a weak enough function of metal work function to be considered universal for all metals. Note the large convections for 5×10^5 V/cm (which occurs for approximately one volt bandbending with a doping of 10^{18} cm^{-3}). The net results for the case of GaAs are thus of considerable interest.

G. Schottky Barrier Capacitive Characterization of Impurities

The behavior and concentration of charged impurity states is a critical factor in the operation of charge control semiconductor devices. To this end we have sought to inforce the tools for measuring and analyzing the effects of such levels in Schottky barriers. The Schottky barrier has been chosen as a fairly standard configuration because it can be formed with a minimum perturbation of the semiconductor material. Work in this area has proceeded along these lines during the past year, namely in developing a simple easily applied theory of the capacitance effects of such impurities (this aspect of the work has been funded by the Army Research Office, Durham). The resulting guidelines are summarized below. We have also continued work on measuring equipment for acquiring capacitance-voltage and capacitance-frequency relationships for Schottky barriers. Pilot work on fabrication of Schottky barriers on GaAs has also been done and point-by-point C-V data taken on representative diodes. A more complete investigation has been held in abeyance pending completion of the measuring equipment.

1. Theoretical

Beguwala and Crowell have developed a more comprehensive solution for deep level effects. A differential equation has been derived which enables one to evaluate the complex capacitance (i.e., conductance and susceptance) of a Schottky barrier in the presence of several deep lying impurities. Our approach also facilitates the modeling of the impedance with lumped frequency independent circuit elements. We have

established that our previously reported three element model (Fig. 66a) is not particularly satisfactory for a distribution of deep levels and even for a single deep level does not bear a simple relationship to the impurity time constant and concentration. Our present approach yields an equivalent circuit with 3r+1 frequency independent elements for a system with r impurity levels (Fig. 66b). The $R_i C_{di}$ product equals the time constant of the nth level over the frequency range of interest. The C_i capacitances constitute the dielectric contributions of the semiconductor depletion region. The capacitances have simple relationships to the concentrations and energy levels of the different impurity species. This model can be uniquely synthesized from experimental C vs ω measurements at a single temperature if one can measure capacitance far enough into forward bias. Failing this one needs to consider C vs temperature and C vs V measurements along with C vs ω measurements for a unique synthesis. This type of characterization gives one considerable physical insight into the role of each impurity level and furthermore emphasizes the interdependence of capacitance and conductance.

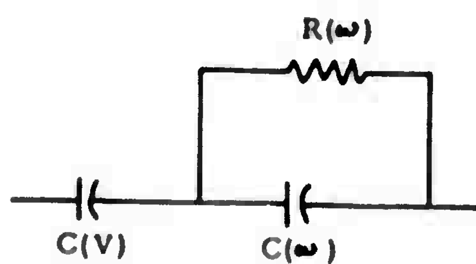

Fig. 66a

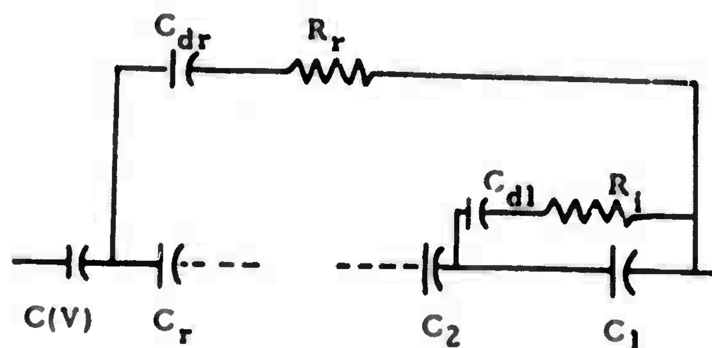

Fig. 66b

2. Measurement Facilities

We have considerably improved the performance of our electronically balanced capacitance measuring system during the past year and have made a variety of pilot measurements, none, however, characteristic of a system that is yet well enough documented for extensive use.

We have virtually completed construction of a universal constant-voltage as signal source unit which operates in conjunction with a programmable bias supply and two oscillators, one programmable for frequency or amplitude modulation and the other a low frequency source with a gain proportional to the dc bias across the diode under test. This signal source will permit C-ω, C-V and impurity profile scanning. At the moment the voltage sweep times and waveforms are not optimum for the frequency sweep and voltage sweep in the low frequency range ($2H_z$ - 200 H_z) and appropriate modifications are in progress.

The electronic balancing circuits consists of an inverting operational amplifier configuration with a selection of bridged T feedback network . The bridged-T is necessary to allow the passage of dc through the test diode and higher current ranges of necessity force higher low frequency limitation for capacitance measurements. For most diodes, however, there is a wide frequency range over which the output voltage has a constant capacitive sensitivity. We have designed this system to be critically damped for ranges in which the low frequency cutoff is above 200 H_z, the frequency range in which transient capacitance measurements are anticipated to be of use. In the low frequency range (down to 2 H_z) we have designed the system to be undercritically damped to extend the low frequency capabilities. We have decided that this represents a reasonable low frequency limit for C-ω measurements and that for phenomena with capacitive effects in the lower frequency ranges that measurements of capacitance transients will be as meaningful and easier to make. We are designing this electronic balancing system to be direct reading to have an internal calibration for capacitance and conductance and to have focusing for offset adjustment to eliminate stray conductance or capacitance effects.

The output of the electronic balancing circuit is fed to a PAR124 phase sensitive detector which permits electronically controlled frequency sweeping and either capacitance or conductance readout. We have not yet completed the auxiliary systems described above to specify the orthogonality of capacitance and conductance effects as a function of frequency but this feature is almost ready for documentation. Preliminary indications suggest that a phase orthogonality within $1/2^{\circ}$ can be maintained during a frequency sweep over a useful frequency range (i.e., a decade or more).

The final online analogue computer that is used to process the data to give output voltages corresponding to C, C^{-2}, C^{-3} by C, $\omega \log \omega$ and impurity density is essentially operational but requires some additional circuitry to facilitate scale charges and requires a circuit card library to make the output functions easily available.

3. Measurements

A limited number of point-by-point measurements on Pt-n-type GaAs Schottky barriers have been made to debug sample fabrication techniques for C-V measurement. Figure 67 shows $1/C^2$ versus V results for a nominal Te doping of 1.6×10^{16} cm^{-3} (300°C Hall measurement). The results on chemical-mechanical polished and solvent-rinsed surfaces showed large anomalies, presumably due to damage of the surface layer in polishing. Chemically etched samples, on the other hand, had much straighter $1/C^2$ versus V relationships at large reverse bias (indicating homogeneous doping of 4×10^{16} cm^{-3}), but had an anomaly starting at ~ 0.5 volts forward bias. This anomaly was not observed with a sample from another crystal of comparable doping.

With completion of the scanning capacitance system, routine acquisition of similar capacitance and conductance data and Hall effect measurements is planned for all newly prepared GaAs.

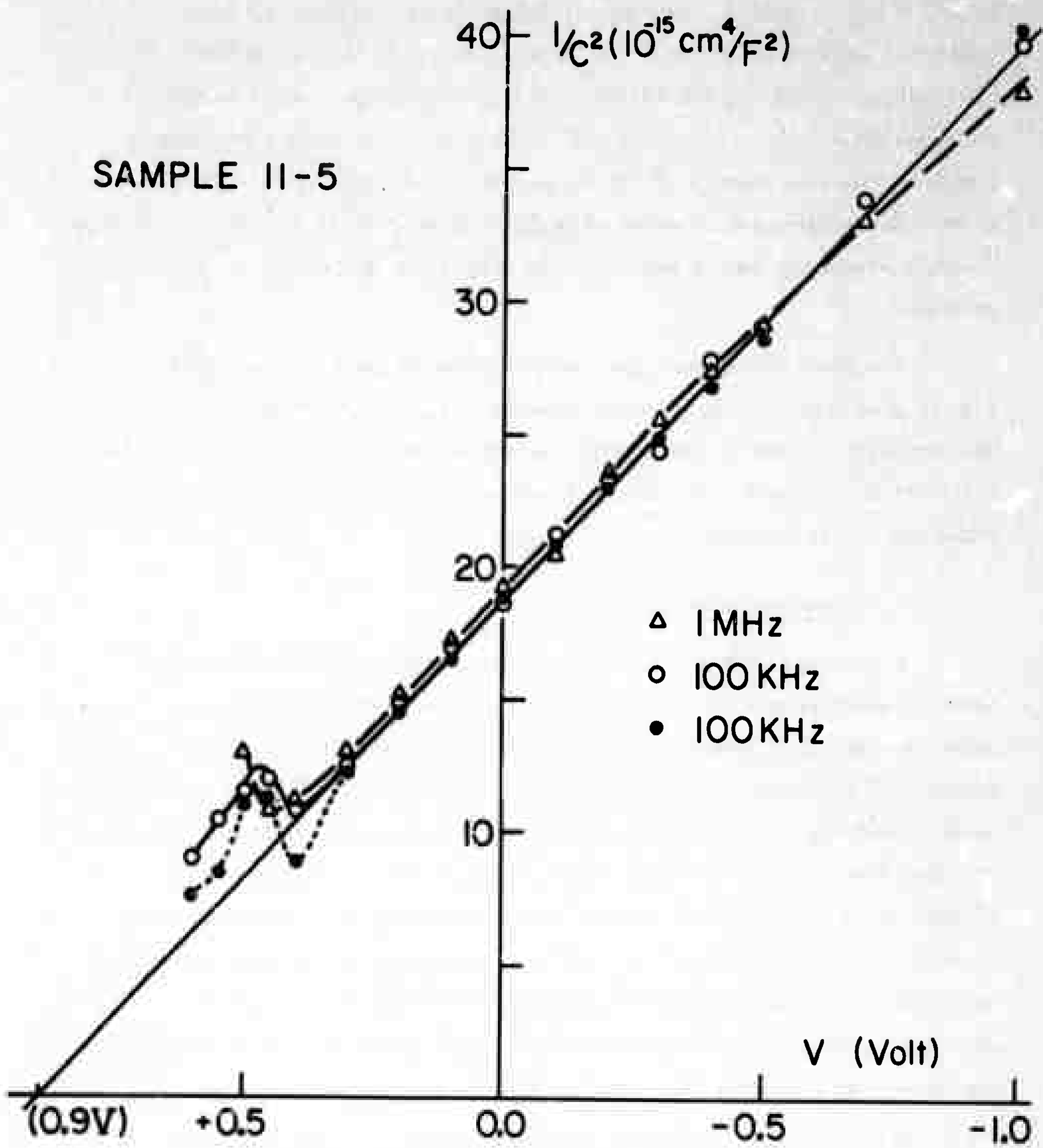

Figure 67 Capacitance-Voltage Measurements on Pt-n-type GaAs Schottky Barrier.

REFERENCES

1. Final Technical Report, "New Methods for Growth and Characterization of GaAs and Mixed III-V Semiconductor Crystals," ARPA Order No. 1628, Grant No. DAHC15-70-G14 (July 1971).

* 2. P. C. Leung and W. P. Allred, "Improved Czochralski Grower for Gallium Arsenide," Houston Electrochemical Society Meeting (1972).

* 3. E. S. Johnson and W. P. Allred, "Liquid Encapsulated Zone Refining of Gallium Arsenide," Princeton meeting of American Association for Crystal Growth, 1972.

* 4. C. E. Chang and W. R. Wilcox, Mat. Res. Bull. 6, 1297 (1971).

5. W. R. Wilcox, Ch. 6 in "Fractional Solidification," edited by M. Zief and W. R. Wilcox (Dekker, 1967).

* 6. V. F. Yip, C. E. Chang and W. R. Wilcox, "Vertical Gradient Freeze Crystal Growth of GaAs: Theory and Practice," Princeton AACG meeting, 1972.

* 7. V. F. Yip, C. E. Chang and W. R Wilcox (paper in preparation).

* 8. V.H.S. Kuo and W. R. Wilcox, "Some Factors Influencing the Pushing of Foreign Particles During Solidification," Princeton AACG meeting, 1972.

* 9. K. Chen and W. R. Wilcox, I/EC Fund. (in press).

* 10. K. H. Chen and W. R. Wilcox, "Boiling and Convection During Movement of Solvent Inclusions," Princeton AACG meeting, 1972.

11. W. R. Wilcox, Ind. Eng. Chem. 61, 76 (March 1969).

* 12. R. T. Pepper and W. R. Wilcox, J. Composite Materials 5, 465 (1971).

* 13. W. R. Wilcox and P. J. Shlichta, J. Crystal Growth 15, 61(1972)

14. R. C. Newman, F. Thompson, M. Hyliards and R. F. Peart, Solid State Comm. 10, 505 (1972).

* 15. A. L. Esquivel and S. Sen, Bull. Amer. Phys. Soc. Ser. II 17, 61(1972).

---

*Papers resulting from this grant.

16. J. F. Nye, Acta Met., 1, 153 (1953).

17. A. Clawson and H. Wieder, U.S. Patent No. 3,532,562 (6 Oct 1970).

18. L. R. Weisberg, F. D. Rosi, and P. G. Herkart, in "Properties of Elemental and Compound Semiconductors," H. C. Gatos, ed., (Interscience Publishers, N.Y., 1960), p. 49.

19. A. F. Kravchenko, A. M. Palkin, and V. P. Rulera, Soviet Physics-Semiconductors, 1, 922 (1968).

20. S. P. Grishina, M. G. Mil'vidskii, V. B. Osvenskii, and V. I. Fistul', Soviet Physics-Semiconductors, 4, 240 (1970).

21. R. A. Logan, G. L. Pearson, and D. A. Kleinman, J. Appl. Phys. 30, 885 (1959).

22. U. Baitinger, J. Arndt, and D. Schnepf, J. Materials Science 4, 396 (1969).

23. R. L. Bell and A.F.W. Willoughby, J. Materials Science 5, 198 (1970).

24. H. C. Marciniak and D. B. Wittry, Rev. of Sci. Instr. 42, 1810 (1971).

25. J. W. Colby, "MAGIC - A Computer Program for Quantitative Electron Microprobe Analysis," Bell Telephone Laboratories, Inc., Allentown, Pa.

26. W. K. Subashiev and S. A. Abagyan, "Band Structure of $GaAs_{1-x}P_x$ Crystals," in Proceedings of the International Conference of the Physics of Semiconductors, (Dunod, Paris, 1964).

27. W. G. Spitzer and C. A. Mead, Phys. Rev. 133, A872 (1964).

28. D. A. Cusano, G. E. Fenner and R. O. Carlson, General Electric Research Laboratory Report No. 64-RL-3767G (September 1964).

29. M. B. Panish and H. C. Casey, J. Appl. Phys. 40, 164 (1966).

30. M. G. Holland, Phys. Rev. 134, A471 (1964).

31. H. Weiss, Ann. Physik 4, 121 (1959).

32. G. S. Almasi, J. Blair, R. E. Ogilvie, and R. J. Schwartz, J. Appl. Phys. 36, 1848 (1965).

33. H. C. Casey, Jr., and R. H. Kaiser, Appl. Phys. Letters 8, 113 (1966).

REFERENCES (continued)

* 34. C. R. Crowell, T. F. Kao, C. L. Anderson and V. L. Rideout, Surface Science (in press).